

# Fatigue of Aluminum Welds In Canadian Highway Bridges

by

Reid Coughlin

A thesis  
presented to the University of Waterloo  
in fulfillment of the  
thesis requirement for the degree of  
Master of Applied Science  
in  
Civil Engineering

Waterloo, Ontario, Canada, 2010

©Reid Coughlin 2010

I hereby declare that I am the sole author of this thesis. This is a true copy of the thesis, including any required final revisions, as accepted by my examiners.

I understand that my thesis may be made electronically available to the public.

## Abstract

Aluminum is the most common metal in the world and its high strength to weight ratio, along with excellent corrosion resistance, can provide efficient solutions for the design and rehabilitation of highway bridge structures. A reduction in a structure's self-weight, when using aluminum, is advantageous for the rehabilitation of existing structures requiring an increased live load capacity and for rapid bridge replacements whereby larger, lightweight components can be installed with limited disruption to traffic. Aluminum structures and components offer the potential for lower life-cycle costs due to the favourable corrosion resistance, allowing for less maintenance over the life of the structure.

One significant disadvantage of aluminum is that it is more susceptible to fatigue damage in relation to steel. Being a newer design material for bridge structures, compared to steel, and due to its limited use in the past, limited fatigue testing has been conducted to date. Bridge design codes and specifications employ different approaches for establishing fatigue design (S-N) curves for aluminum structures. The British and European design standards use a two-slope design curve, with a shallower slope in the high cycle range, implying that fatigue damage accumulates at a different rate at lower stress ranges. The Aluminum Association in the United States uses a more conservative approach, assuming a single-slope design S-N curve, by simply extending the curve past the constant amplitude fatigue limit at the initial slope. Limited testing under variable amplitude loading in the high cycle range has been completed to date, where a second slope could be warranted. A new chapter of the Canadian Highway Bridge Design Code (CSA-S6) on aluminum structures is currently under development. The research presented herein provides recommendations regarding the correction factors required for fatigue design of aluminum. In addition, fatigue testing and fracture mechanics analysis studies are performed to further investigate the use of a two-slope S-N curve for the fatigue design of aluminum highway structures.

It is shown that using fatigue correction factors derived for steel can result in unconservative designs for aluminum structures. On this basis, new correction factors are proposed. The effects of overload events, such as overloaded trucks and simultaneous truck crossings, are also considered and an amplification factor is proposed to account for increases in the fatigue correction factor due to the occurrence of such overload events.

A fatigue test program was undertaken including both constant and variable amplitude testing for a non-load carrying fillet welded transverse stiffener fabricated from 6061-T651 aluminum. For all fatigue specimens, dye penetrants were applied when a fatigue crack was present to facilitate measurements to quantify the crack shape. Static tension and cyclic coupon tests were conducted to determine material properties for both as-received and annealed aluminum. Hardness tests were also conducted for as-received and annealed aluminum, as well as aluminum in the heat-affected zone (HAZ), to estimate the material properties of the aluminum at the vicinity of the weld. Residual stress testing was also conducted on fatigue specimens to determine residual stresses present at the weld toe. The parameters established based on this laboratory work were used as input for a fracture mechanics analysis.

Validation of the employed linear elastic fracture mechanics model was completed through a sensitivity analysis of the input parameters and comparison with the constant amplitude fatigue test data. With a working fracture mechanics model, fatigue life predictions were generated for the tested variable amplitude load histories, which were representative of in-service loading histories induced by realistic truck traffic. It is shown that the fatigue life predictions provide a good fit with the test data and suggest that the use of a second slope in the design S-N curve may be warranted. Fatigue life predictions were also generated to examine the effects of overload events. Based on these predictions, it is concluded that overload events cause a reduction in fatigue life in the high cycle range. Finally, a scale effect study was conducted to predict the fatigue life of full-scale fatigue details, accounting for increased plate thickness, residual stresses, and initial defect depths. The results of this study showed that the fatigue life of the large-scale fatigue details is reduced as compared to the small-scale specimens tested.

## **Acknowledgements**

I would like to thank my supervisor, Professor Scott Walbridge, for his assistance with the preparation of this thesis, for without his help this would not be possible. His knowledge and expertise in the area of fatigue and fracture was paramount in completion of this research.

I would like to thank the Civil Engineering Structures Lab technicians, Doug Hirst, Richard Morrison, and Rob Sluban for their knowledge and assistance with the lab testing portion of my research. A special thanks to Maria El Zeghayar for her guidance in completion of the cyclic testing, and to Max Hsu for his general assistance in the lab. I would also like to thank Kasra Ghahremani for his help in many areas throughout my research.

Finally, I would like to thank my family, friends, and office mates for their continuous support and motivation. They all made my Masters research an enjoyable experience.

## Table of Contents

Author's Declaration.....	ii
Abstract.....	iii
Acknowledgements.....	v
Table of Contents.....	vi
List of Figures.....	x
List of Tables.....	xiv
1. Introduction.....	1
1.1 General.....	1
1.2 Objectives.....	2
1.3 Scope.....	2
1.4 Thesis Organization.....	2
2. Literature Review.....	4
2.1 Aluminum Alloys.....	4
2.2 Aluminum in Bridges.....	6
2.2.1 Design Considerations.....	6
2.2.2 Past Aluminum Bridge Structures.....	8
2.3 Fatigue of Aluminum Welds.....	17
2.3.1 Comparing CA and VA Fatigue Test Data.....	18
2.3.2 Testing at the ATLSS Laboratory at Lehigh University.....	20
2.3.3 Testing for the ERAAS Fatigue Document.....	21
2.3.4 EUREKA Research Project.....	23
2.4 Current Design S-N Design Curves.....	24
2.4.1 Canadian Standards Association.....	25
2.4.2 The Aluminum Association.....	26
2.4.3 European Committee for Standardization.....	28
2.4.4 British Standard Institute.....	29
2.4.5 International Institute of Welding.....	30
2.4.6 Code Comparison for the Design S-N Curve.....	32
2.5 Fatigue Load Correction Factors.....	35
2.6 Overload Traffic Events.....	37
2.7 Fracture Mechanics.....	41

2.7.1 Concurrent to testing at the ATLSS Laboratory.....	41
2.7.2 Concurrent to the EUREKA Research Project.....	44
2.7.3 Initial Crack Size and Crack Shape.....	45
2.7.4 Residual Stresses in Welded Aluminum Components.....	48
2.7.5 Cyclic Material Constants.....	49
2.8 Summary.....	51
3. Fatigue Load Correction Factors.....	53
3.1 Calibration Procedure.....	53
3.2 CSA-S6 Load Correction Factors.....	56
3.2.1 Calibration Data.....	57
3.2.2 Calibration Results.....	58
3.3 AASHTO Load Correction Factors.....	61
3.3.1 Calibration Requirements.....	61
3.3.2 Calibration Results.....	65
3.4 Effect of Overload Events.....	68
3.4.1 Case One: Overloaded Trucks.....	68
3.4.2 Case Two: Multiple Occurrences of Trucks.....	73
4. Fatigue and Materials Testing.....	84
4.1 Fatigue Testing.....	84
4.1.1 Test Program.....	84
4.1.2 Test Specimens.....	86
4.1.3 Test Equipment and Procedure.....	88
4.2 Static Tensile Coupon Testing.....	91
4.2.1 Test Program and Specimen Geometry.....	91
4.2.2 Test Equipment and Procedure.....	92
4.3 Cyclic Coupon Testing.....	93
4.3.1 Testing Program and Specimen Geometry.....	94
4.3.2 Test Equipment and Procedure.....	94
4.4 Microhardness Testing.....	96
4.4.1 Test Program and Specimen Geometry.....	96
4.4.2 Test Equipment and Procedure.....	98
4.5 Residual Stress Testing.....	99

4.5.1 Test Description .....	99
5. Fatigue and Materials Testing Results .....	101
5.1 Fatigue Testing.....	101
5.1.1 Test Results and Interpretation .....	101
5.1.2 Crack Shape Measurements .....	104
5.2 Static Tensile Material Testing .....	106
5.2.1 Test Results and Interpretation .....	107
5.3 Cyclic Testing .....	111
5.3.1 Test Results and Interpretation .....	112
5.4 Microhardness Testing.....	114
5.4.1 Test Results and Interpretation .....	114
5.5 Residual Stress Testing.....	118
5.5.1 Test Results and Interpretation .....	118
6. Fracture Mechanics Analysis .....	121
6.1 Introduction.....	121
6.2 Linear Elastic Fracture Mechanics Model .....	121
6.3 Fracture Mechanics Input Parameters.....	124
6.3.1 Material Properties.....	124
6.3.2 Initial Crack Depth.....	125
6.3.3 Crack Shape .....	125
6.3.4 Residual Stress .....	126
6.3.5 Crack Growth Parameters .....	126
6.4 Constant Amplitude and Sensitivity Analysis .....	127
6.5 Variable Amplitude Analysis.....	134
6.5.1 Comparison with VA Test Data.....	135
6.5.2 Overload Analysis.....	137
6.5.3 Additional Analysis of Different Influence Lines.....	139
6.5.4 Scale Effect Study .....	143
6.6 Strain Based Analysis .....	145
6.6.1 Strain Based Fracture Mechanics Model .....	145
6.6.2 Analysis Results Using SBFM.....	148
7. Conclusions and Recommendations .....	151



7.1 Conclusions .....	151
7.1.1 Fatigue Correction Factors .....	151
7.1.2 Experimental Testing and Fracture Mechanics Analysis .....	151
7.2 Recommendations for Future Work .....	154
7.2.1 Fatigue Correction Factors .....	154
7.2.2 Experimental Testing and Fracture Mechanics Analysis .....	154
References .....	156

## List of Figures

Figure 2.1: Loss of strength in the HAZ [Gitter 2006] .....	5
Figure 2.2: Smithfield Street Bridge in Pittsburgh, PA [Hecker 2003] .....	12
Figure 2.3: Arvida Bridge in Quebec, Canada over the Saguenay River [CSCE 2005] .....	13
Figure 2.4: Fairchild Bridge Design [Siwowski 2006] .....	14
Figure 2.5: Svensson Deck (left) and Alumadeck (right) .....	16
Figure 2.6: All-aluminum bridge in Norway (left) and floating bridge in Netherlands (right) [Siwowski 2006] .....	17
Figure 2.7: Characteristic CA stress range representation .....	19
Figure 2.8: Small-scale cruciform joints (left) and full-scale beam specimens (right) .....	20
Figure 2.9: ATLSS test data for axial cruciform and beam stiffeners [Menzemer and Fisher 1993] ..	21
Figure 2.10: ERAAS test data for a non-load carrying web stiffener [Jaccard <i>et al.</i> 1995] .....	22
Figure 2.11: Fatigue details tested for the EUREKA research program .....	23
Figure 2.12: EUREKA test data for a cruciform joint with $t = 12$ mm [Soetens <i>et al.</i> 1995] .....	23
Figure 2.13: EUREKA test data for cruciform joint and beam stiffeners [Soetens <i>et al.</i> 1995] .....	24
Figure 2.14: EUREKA CA/VA test data for a cruciform joint with $t = 12$ mm [Soetens <i>et al.</i> 1995] ..	24
Figure 2.15: CSA-S157 design S-N curves [CSA 2005] .....	25
Figure 2.16: ADM 2005 design S-N curve [AA 2005] .....	26
Figure 2.17: ADM 2005 design S-N curve representation [AA 2005] .....	27
Figure 2.18: Eurocode 9 design S-N curves for fillet welds [CEN 2006] .....	28
Figure 2.19: BS 8118 design S-N curves [BSI 1992] .....	30
Figure 2.20: IIW design S-N curves under CA loading [Hobbacher <i>et al.</i> 2005] .....	31
Figure 2.21: IIW design S-N curves under VA loading [Hobbacher <i>et al.</i> 2005] .....	32
Figure 2.22: Design S-N curve comparison for a non-load carrying transverse stiffener .....	34
Figure 2.23: Differences between single- and two-slope S-N design curves [Menzemer 2000] .....	34
Figure 2.24: CSA CL-625 design code truck [CSA 2006] .....	36
Figure 2.25: AASHTO fatigue design truck (left) and fatigue design truck proposed by Moses et al. [1987] (right) .....	37
Figure 2.26: Comparison of the CL-625 with maximum observed loading conditions [CSA 2006] ..	39
Figure 2.27: ATLSS LFM analysis for overload events [Menzemer and Fisher 1993] .....	42
Figure 2.28: ATLSS LFM analysis for beam stiffeners with varying initial crack sizes [Menzemer 1992] .....	43

Figure 2.29: ATLSS LEFM analysis for beam stiffeners with varying crack shape ratios [Menzemer 1992].....	43
Figure 2.30: EUREKA LEFM analysis [Soetens <i>et al.</i> 1995].....	44
Figure 2.31: Defect histogram for initial flaws of welded aluminum components [Menzemer 1992]	45
Figure 2.32: Influence of initial crack length on fatigue life [Kosteas and Bompard 1995] .....	48
Figure 2.33: Aluminum cyclic testing data [Burk and Lawrence 1978] .....	50
Figure 3.1: Influence lines used in calibration for one (left), two (centre), and five (right) spans.....	54
Figure 3.2: Sample of load effect history (left) and histogram (right) for $ps-m$ , $L = 30$ m case.....	55
Figure 3.3: Conceptual explanation of calibration procedure .....	56
Figure 3.4: GVW histogram for the Ontario traffic survey .....	57
Figure 3.5: CSA-S6 correction factor results for CSA-S6 Detail Category A ( $m = 6.85$ ) .....	59
Figure 3.6: CSA-S6 calibration results using AASHTO design S-N curves.....	60
Figure 3.7: CSA-S6 calibration results using CSA-S157 design S-N curves.....	61
Figure 3.8: AASHTO fatigue design code truck (HS20-44) [AASHTO 2007] .....	62
Figure 3.9: GVW histogram for an American survey of 27513 trucks [Snyder <i>et al.</i> 1985] .....	64
Figure 3.10: GVW histograms for American truck data included (left) and excluded (right) in this study .....	64
Figure 3.11: AASHTO correction factor results for single slope S-N curve with $m = 3$ .....	66
Figure 3.12: Calibration results for AASHTO aluminum design S-N curves .....	67
Figure 3.13: FBDM L-165 design truck.....	69
Figure 3.14: FBDM design truck comparison to the MOL and OBF.....	69
Figure 3.15: Overloaded trucks using modified HS20-44 (left) and modified CL-625 (right) .....	70
Figure 3.16: CSA-S6 correction factor results for overload events.....	71
Figure 3.17: CSA-S6 correction factor results for CL-625 amplified by 1.0, 1.5, and 2.0 .....	72
Figure 3.18: AASHTO correction factor results for overload events.....	73
Figure 3.19: CSA-S6 correction factor results for overloads every 450 <sup>th</sup> truck passage .....	75
Figure 3.20: AASHTO correction factor results for overloads every 450 <sup>th</sup> truck passage .....	76
Figure 3.21: CSA-S6 correction factor results for overloads every 15 <sup>th</sup> truck passage.....	77
Figure 3.22: AASHTO correction factor results for overloads every 450 <sup>th</sup> truck passage.....	78
Figure 3.23: Truck simulation based on GVW cumulative distribution .....	79
Figure 3.24: CSA-S6 correction factor results using Nowak and modified Nowak models .....	80
Figure 3.25: CSA-S6 correction factor results using Nowak model .....	81

Figure 3.26: AASHTO correction factor results using Nowak and modified Nowak models.....	81
Figure 3.27: AASHTO correction factor results using Nowak model.....	82
Figure 4.1: VA load histories for LH1 (top) and LH2 (bottom).....	85
Figure 4.2: Fatigue test specimen geometry.....	87
Figure 4.3: Specimen fabrication; aluminum panels (left) and saw-cut specimens (right).....	87
Figure 4.4: MTS 810 material testing frame.....	89
Figure 4.5: Crack shape ratio estimation using dye penetrant (specimen H4 shown).....	90
Figure 4.6: Dye penetrant quality classification.....	91
Figure 4.7: Tensile test specimen geometry [ASTM 2004].....	92
Figure 4.8: Oven used for full annealing of aluminum specimens.....	93
Figure 4.9: Cyclic test specimen geometry.....	94
Figure 4.10: Cyclic test frame using MTS 442 controller.....	95
Figure 4.11: Apparatus used to hang specimens during annealing process.....	95
Figure 4.12: Cyclic test specimen with M-Coat.....	96
Figure 4.13: Hardness test specimen.....	97
Figure 4.14: Fabrication of hardness test specimens from existing fatigue and tensile specimens.....	97
Figure 4.15: Vickers hardness test locations for BM & AM (left), and WM & HAZ (right).....	98
Figure 4.16: Vickers hardness machine (left) and high-powered microscope (right).....	99
Figure 5.1: Fatigue test data compared with AASHTO design S-N curve for Detail Category C.....	102
Figure 5.2: CA fatigue data compared with Menzemer [1992] data.....	103
Figure 5.3: CA fatigue data compared with ERAAS data [Jaccard <i>et al.</i> 1995].....	104
Figure 5.4: Crack shape ratio histogram.....	105
Figure 5.5: Crack shape measurements versus Menzemer [1992] relationship.....	106
Figure 5.6: Engineering stress vs. strain for as-received 6061-T651 aluminum.....	108
Figure 5.7: Engineering stress vs. strain for annealed 6061-O aluminum.....	108
Figure 5.8: Engineering stress vs. strain for 6061-T651 and 6061-O aluminum.....	109
Figure 5.9: Failure of 6061-T651 (bottom) and 6061-O (top).....	110
Figure 5.10: Failure surfaces of 6061-T651 (left) and 6061-O (right).....	111
Figure 5.11: Total engineering & plastic strain for 6061-T651 aluminum.....	112
Figure 5.12: Cyclic test data for 6061-T651 aluminum.....	113
Figure 5.13: Cyclic test data for 6061-O aluminum.....	114
Figure 5.14: Vickers hardness pyramid diagonal length measurements.....	115

Figure 5.15: Vickers hardness measurements for BM & AM.....	116
Figure 5.16: Vickers hardness measurements for WM & HAZ.....	117
Figure 5.17: Residual stress measurement locations [Proto 2010].....	118
Figure 5.18: Residual stress measurements at weld toe [Proto 2010].....	119
Figure 6.1: Effective and opening stress intensity factor representation [Stephens <i>et al.</i> 2001].....	122
Figure 6.2: SCF determination: FE model of weld detail (left) and SCF distribution (right).....	123
Figure 6.3: Crack growth rate curves based on Eurocode 9.....	126
Figure 6.4: Material properties comparison for $R = 0.1$ .....	128
Figure 6.5: Initial crack depth comparison for $R = 0.1$ .....	129
Figure 6.6: Crack shape ratio comparison for $R = 0.1$ .....	130
Figure 6.7: Crack shape ratio comparison for all $R$ -ratios.....	131
Figure 6.8: Residual stress comparison for $R = 0.1$ .....	132
Figure 6.9: Residual stress comparison for $R = -1.0$ .....	133
Figure 6.10: Crack growth data comparison for $R = 0.1$ .....	134
Figure 6.11: VA test data and LEFM prediction for load history LH1.....	135
Figure 6.12: VA test data and LEFM prediction for load history LH2.....	136
Figure 6.13: VA test data and LEFM prediction for the LH1 and LH2 load histories.....	137
Figure 6.14: LEFM predictions considering overload events for the LH1 load history.....	138
Figure 6.15: LEFM predictions considering overload events for the LH2 load history.....	139
Figure 6.16: Influence lines used to generate in-service load effect histories: single-span simply supported girders (left) and two-span continuous girders (right).....	140
Figure 6.17: Girder span comparison for the $p2tr-mx$ influence line.....	141
Figure 6.18: Girder span comparison for the $p2tr-m$ influence line.....	142
Figure 6.19: Lower bound LEFM predictions for all influence lines.....	143
Figure 6.20: Plate thickness comparison for large-scale components.....	144
Figure 6.21: Initial crack depth comparison for large scale components.....	145
Figure 6.22: Explanation of stress-strain analysis used in the fracture mechanics model.....	147
Figure 6.23: LEFM and SBFM comparison for CA loading.....	149
Figure 6.24: LEFM and SBFM comparison for VA loading.....	150

## List of Tables

Table 2.1: Aluminum bridges in North America and Europe.....	10
Table 2.2: Aluminum cyclic properties [Burk and Lawrence 1978].....	50
Table 3.1: Average annual daily truck traffic [CSA 2006].....	57
Table 3.2: Design detail categories for AASHTO, CSA-S6, and CSA-S157.....	58
Table 3.3: CSA-S6 fatigue correction factor results corresponding to AASHTO detail categories ....	60
Table 3.4: United States truck category axle weights and spacings [Moses <i>et al.</i> 1987].....	63
Table 3.5: United States truck categories and types [Moses <i>et al.</i> 1987, Harwood <i>et al.</i> 2003].....	63
Table 3.6: AASHTO fatigue correction factor results .....	67
Table 3.7: Simultaneous truck crossing amplification factor.....	83
Table 4.1: Fatigue test matrix .....	86
Table 4.2: Cross-sectional dimensions of fatigue test specimens .....	88
Table 4.3: Crack shape ratio comparison.....	91
Table 4.4: Vickers hardness test matrix .....	98
Table 5.1: Tensile specimen dimensions before testing and after failure .....	107
Table 5.2: Description of load-displacement data.....	107
Table 5.3: Aluminum alloy mechanical properties .....	109
Table 5.4: Aluminum alloy mechanical properties .....	110
Table 5.5: Vickers hardness results summary.....	117
Table 5.6: Residual stress test results.....	119
Table 6.1: 6061-T651 aluminum material properties .....	125
Table 6.2: Sensitivity analysis expected values .....	127

# Chapter 1

## Introduction

### 1.1 General

In the design of highway bridge structures in Canada, limit states design principles are followed to ensure all structural components comply with the ultimate, serviceability, and the fatigue limit states outlined in the *Canadian Highway Bridge Design Code (CSA-S6)*. Currently absent from the CSA-S6 is guidance on the design of aluminum bridge structures. A CSA-S6 Technical Committee was established to address this through the development of a new chapter for CSA-S6 on the design of aluminum highway bridge structures.

There are a number of issues related to the fatigue limit state that need to be resolved, particularly in relation to the fatigue of aluminum welds in highway bridge structures. In many highway bridge design codes, fatigue design involves passing a code truck model over influence lines for various critical locations on the bridge and determining the resulting nominal stress ranges. These stress ranges are then multiplied by a fatigue correction factor to account for differences in the fatigue damage due to the code truck and the expected real traffic. The calculated nominal stress range must not exceed the fatigue resistance of the associated fatigue detail, as defined by fatigue design (S-N) curves and detail categories provided in design codes. In the current Canadian and American codes, correction factors have been established for use with fatigue design S-N curves having a single slope of  $m = 3.0$ . Although suitable for steel, the assumptions on which these correction factors are based are generally not applicable to aluminum structures which use S-N curves with  $m \neq 3$ . There is a need to derive similar correction factors for the design of welds in aluminum highway structures.

Many design codes and specifications in Europe use two-slope design S-N curves to determine the fatigue resistance. The *AASHTO LRFD Bridge Design Specification (AASHTO)* in the United States uses single-slope design S-N curves. Historically, the use of fracture mechanics analysis has been the primary basis for the use of a second slope in design S-N curves. At this point, very limited test data exists under variable amplitude loading in the high cycle domain where a second slope is used. There is an additional need to investigate the problem further through fatigue and material testing and linear elastic fracture mechanics analysis.

## **1.2 Objectives**

The primary objectives of the work summarized in this thesis were as follows:

1. To establish fatigue correction factors for welded aluminum structures for use in the CSA-S6 and AASHTO Bridge Codes.
2. To perform experimental testing and fracture mechanics analysis to investigate the appropriateness of a two-slope S-N curve for the fatigue design of aluminum for bridge structures, including:
  - fatigue testing to develop a database of test results in the high-cycle range under variable amplitude loading conditions,
  - materials testing to determine input parameters for the fracture mechanics analysis, and
  - linear elastic fracture mechanics analysis, to generate fatigue life predictions in the high cycle range to quantify the effects of overload events, varied loading histories, and scale effects on the S-N curve.

## **1.3 Scope**

The scope of the work presented in this thesis is limited to three major areas: review and formulation of fatigue correction factors for both the CSA-S6 and AASHTO Bridge Codes, experimental and materials fatigue testing, and a fracture mechanics analysis of aluminum welds under cyclic loading conditions.

The review and calibration of the fatigue correction factors is limited to factors for use in the CSA-S6 and AASHTO Bridge Codes in conjunction with the fatigue design (S-N) curves from the CSA-S157 Aluminum Design Code and the AASHTO Bridge Code.

The fatigue and materials testing is limited to small-scale testing of a single transverse stiffener weld geometry and a single grade of aluminum – 6061-T651.

## **1.4 Thesis Organization**

This thesis is organized as follows: first, a literature review is presented in Chapter 2, in which the most recent research is discussed regarding the use of aluminum in bridges, fatigue testing of aluminum, and design methodologies dealing with the fatigue of aluminum structures. In Chapter 3 a calibration method is described for establishing fatigue correction factors for aluminum structures.



The implementation of this procedure is then discussed and fatigue correction factors are presented for both the CSA-S6 and AASHTO Bridge Codes. In Chapter 4 the fatigue and materials testing program performed for the current thesis is described. The results of this testing program are presented and discussed in Chapter 5. In Chapter 6 a linear elastic fracture mechanics model is described and validated by comparison with the available fatigue test results. It is then used to perform a number of studies to extend the results of the testing program. Finally, Chapter 7 presents the main conclusions and recommendations of this research.

## Chapter 2

### Literature Review

A review of the existing research on the fatigue of aluminum is presented in this chapter. Firstly, the current use of aluminum alloys in bridges and the specific properties of aluminum alloys as they pertain to bridges are discussed. This is followed by a summary of research that has been conducted to date with regards to fatigue of aluminum weldments both from testing data and fracture mechanics analysis. Finally, the most prominent specifications and codes for the fatigue design of aluminum structures both in North America and Europe are discussed and compared.

#### 2.1 Aluminum Alloys

Aluminum is the most common metal and the third most abundant element in the earth's crust behind oxygen and silicon. For more than a century, aluminum has proven to be a suitable design choice for load-bearing structures. The clear advantage of aluminum is its low density, which is approximately one third of steel at  $2700 \text{ kg/m}^3$ . Aluminum alloys are very corrosion resistant. When most copper free aluminum alloys are exposed to atmospheric conditions, they react with oxygen and water vapour to form a thin oxide layer, which provides protection against corrosion [Gitter 2006].

Aluminum is a metal with material properties for certain alloys very similar to mild steel, thus the structural design process is very similar to steel. Considerations for the use of aluminum alloys, in relation to the design of steel, should include its differing mechanical properties; more specifically its linear thermal expansion and elastic modulus. The linear thermal expansion of aluminum is  $23 \times 10^{-6} / ^\circ\text{C}$ , which is twice that of steel. Thus, expansion of the material must be allowed for or the resulting stresses must be accommodated in the design. The elastic modulus of aluminum is one third that of steel at 70 GPa, which has a significant impact on the structural design. For example, Gitter [2006] notes that to maintain the stiffness of a steel section using aluminum, since the weight of aluminum is one third that of steel, simply increasing the section thickness by three times is not effective because this eliminates any weight benefits. A proven rule of thumb for structural design is that by increasing all section dimensions by a factor of 1.4 (excluding the section width), flexural stiffness can be maintained while the weight can be reduced by one half versus steel [Gitter 2006]. Typically the weight of steel sections can only be optimized to a limited extent because standardized sections are used. Gitter [2006] also states that using custom extruded aluminum sections for design, weight reductions greater than 50 percent can be achieved.

A very important consideration when designing with aluminum is the loss of strength due to heat, especially due to the welding process. Similar to other materials, the strength of aluminum decreases with increasing temperature. For aluminum Gitter [2006] states that for temperatures up to 80°C, the loss in strength is negligible for all alloys and tempers. Beyond 80°C, creep effects may have to be considered. The more critical issue with regards to loss of strength due to heat occurs in the vicinity of welds. Due to the local melting of the weld metal needed for the welding process, the temperatures are very high in the region around the weld, thus causing a decrease in the strength of the base metal around the welded area. This area in the vicinity of the weld is commonly referred to as the heat affected zone (HAZ). The strength of aluminum alloys, tend to increase during fabrication processes such as rolling and extruding due to the cold working that results. This cold working can be removed, however, by exposure to sufficiently high temperatures for sufficient periods of time. This process of removal of cold working effects is known as annealing. Intentionally annealed aluminum products are said to have an O-temper, and have material properties similar to those of the HAZ. Aluminum alloys that undergo a solution heat treatment followed by quenching and ageing are said to be heat-treatable aluminum alloys. During the welding process, it is important to note that non-heat treatable alloys lose all the strength gained by work hardening, restoring the alloy to O-temper, while heat-treatable alloys in temper T6 have a strength loss of only approximately 40% and do not return to a fully annealed state [Gitter 2006]. Figure 2.1 illustrates the loss of strength in the HAZ due to the weld.

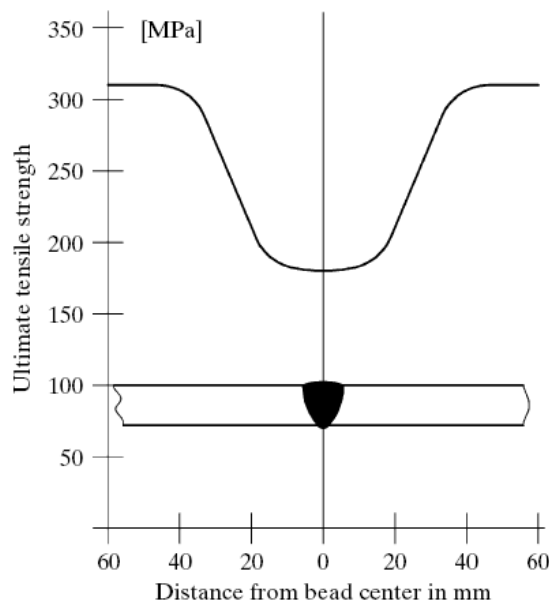


**Figure 2.1: Loss of strength in the HAZ [Gitter 2006]**

Another important design consideration when using aluminum alloys is fatigue. Fatigue occurs when materials are subjected to cyclic loading. Over time cracks develop and propagate under repeated loading to failure. The fatigue strength of aluminum is approximately one third that of steel, thus providing the potential for fatigue to be a more prevailing failure mode in aluminum structures [Das and Kaufman 2007].

## **2.2 Aluminum in Bridges**

### **2.2.1 Design Considerations**

The use of aluminum for the design and rehabilitation of highway bridges can provide efficient solutions in certain cases. Aluminum bridge structures and components offer the potential for lower life-cycle costs due to the excellent corrosion resistance of this material, thus eliminating the need for protective coatings and reducing maintenance requirements. Life-cycle cost analyses have clearly shown the economic benefits of using aluminum for the replacement of existing bridge decks [Siwowski 2006]. The relative ease of transportation and erection of aluminum bridge components also allows for the use of accelerated bridge construction techniques as all or part of the structure can be shipped and installed on-site [Das and Kaufman 2007]. Light, prefabricated bridge systems may also be of interest in remote locations where the use of concrete may not be feasible and steel erection may be costly.

The many advantages of the use of aluminum in bridge structures are described by Das and Kaufman [2007]. The foremost advantage of using aluminum is its low density; which is approximately one third that of steel. For the rehabilitation of existing bridges, by replacing aging concrete decks with new extruded aluminum ones, the live load capacity can be significantly increased due to the resulting reduction in the dead load. An increase in the live load capacity of the structure using aluminum can provide cost savings for the rehabilitation of substructure and superstructure components [Siwowski 2006]. The reduction of the structures dead load due to the light weight of aluminum reduces the loads transmitted to the foundations [Mazzolani 2006]. By reducing the loads imposed on the foundations for the rehabilitation of an existing structure, the use of aluminum can eliminate the need to remediate the existing substructure. In addition to the low density of aluminum, the strength can be as high as that of mild steel. Reducing the weight of the structure while maintaining strength requirements, aluminum can be more efficient than steel and concrete due to its high strength-to-weight ratio. Benefits of aluminum's light weight are not only apparent in service but also during

construction. Mazzolani [2006] writes that the light weight of aluminum simplifies the erection phases, as completely prefabricated components can be transported to site. It thus reduces the demand for physical labour, and reduces energy use. This energy reduction comes from the reduction in the fossil fuels used to transport the lighter structural components from production to site.

Another advantage of aluminum and possibly the most important reason to consider the use of aluminum in structural applications is its excellent corrosion resistance. Corrosion, associated mainly with the intrusion of de-icing salt, has been identified as the major cause of the deterioration in both concrete and steel bridges [Siwowski 2006]. Therefore, it is the most important factor responsible for the large majority of structurally deficient bridges currently in service. With a high resistance to water and road salt attack, negligible corrosion eliminates the need for protective coatings, thus reducing maintenance costs over the life of the structure. Therefore, the use of aluminum can improve the durability of bridge structures. Many bridge structures are located in marine environments where corrosion levels may be very high, thus the use of aluminum may represent a favourable alternative.

Das and Kaufman [2007] note that aluminum has high toughness and highly ductile fracture in very cold temperatures, which is advantageous in comparison to steel. Steel tends to exhibit a ductile-to-brittle transition at low temperatures, whereas aluminum does not. High toughness at very low temperatures eliminates concerns of brittle fracture, specifically for structures in arctic climates.

Another significant advantage of aluminum in structural applications is its ease of fabrication. The ability to easily develop complex aluminum extrusions allows for an optimized structural design, thus making efficient use of the material and reducing component weight. Aluminum extrusions can be pre-fabricated in large sections and because of their light weight they can be shipped to site and installed quickly and efficiently. Especially for bridge structures, simple erection procedures with fewer components allow for reduced construction times, and more importantly, limited traffic delays. Extrusions can provide stiffer structural shapes while avoiding the excessive welding and bolting typical in built-up sections [Mazzolani 2006]. Simplified structural section allows for the potential to simplify connection details. Use of aluminum extrusions in buildings is very prevalent and provides an advantage for features such as shear connectors, glazing units, snap-together parts, threaded components for bolts, etc.

Although the use of aluminum offers many advantages, Das and Kaufman [2007] also outline the disadvantages of aluminum in bridge structures. The primary disadvantage of aluminum is its higher initial cost compared to steel and concrete. The cost premium covers a large range depending on the

structure but in general the initial cost of aluminum can be 25 to 75 percent higher than steel or concrete. The higher initial cost of aluminum is due in part to the energy required during the manufacturing process, which also poses a higher environmental cost. The high environmental cost is negated by the reduced environmental impact when shipping the lighter weight aluminum. Although the initial cost of aluminum is higher, when you consider the life cycle cost of the structure the use of aluminum may be more cost efficient. Aluminum's excellent corrosion resistance greatly reduces the maintenance costs of the structure; therefore, the life-cycle cost of the structure may be less than steel. Although it is clear through life-cycle cost analysis that the cost of aluminum structures can be less than a steel comparison, the use of aluminum in bridge structures is not frequent. Especially in North America, the design and management of infrastructure projects is generally still governed by the initial costs opposed to the life-cycle cost; therefore the design of aluminum bridge structures is not viewed as a favourable option due to the high initial cost. In addition, typically the budgets for new bridge construction and bridge maintenance are separated [Das and Kaufman 2007] and thus does not account for the life-cycle of the structure, which makes the initial cost of aluminum unfavourable.

Additional disadvantages include some physical properties of aluminum. Aluminum has a modulus of elasticity of 70 GPa which is considerably less than steel at 200 GPa. Low material stiffness poses a design concern when considering buckling due to compressive loading. The fatigue strength of aluminum is also roughly one third that of steel, which can be especially unfavourable in welded structures. Also, aluminum's coefficient of thermal expansion is double that of steel and concrete. These differences in the physical properties of aluminum create design challenges. With limited knowledge of how the properties of aluminum affect design and subsequently a lack of design rules to follow, many engineers are hesitant to incorporate the use of aluminum in bridge design. A lack of information regarding the service life of existing aluminum bridge structures and limited data to validate the low life-cycle costs of aluminum compared to the life-cycle costs of traditional materials contribute to the lack of consideration aluminum receives from bridge engineers [Thompson *et al.* 1996].

### **2.2.2 Past Aluminum Bridge Structures**

Aluminum has successfully been used as a construction material for new bridges and the rehabilitation of existing bridges. Projects involving the rehabilitation of existing bridges where aluminum alloys were used have generally involved replacing decks with lighter weight aluminum ones. In 1933, the first such example of a deck replacement with aluminum and also the first

documented use of aluminum in a bridge structure was the rehabilitation of the Smithfield Street bridge in Pittsburgh, PA. In the following 50 years after the first application of aluminum in bridges, almost 100 bridges around the world, both vehicular and pedestrian, have been constructed [Siwowski 2006]. Many pedestrian bridges have been constructed with aluminum, especially in Europe, but herein the focus is on bridges designed for vehicular traffic.

The first examples of the construction of all-aluminum bridge structures were projects undertaken by Alcan and Alcoa, historically, two major suppliers of aluminum. Both structures provided access to smelting plants. It is believed that Alcan and Alcoa built these structures to demonstrate that aluminum is a potential construction material for bridges. In North America, many of the aluminum structures in existence were constructed in the 1950s and 1960s. During this period, in the United States, there was a national effort to improve and make the highway system safer by incorporating controlled access on superhighways; which required the construction of many bridges for new grade separations. Due to the increased volume of bridge construction projects at that time, the availability of steel became more limited, causing increased steel prices and long lead times to obtain steel in some cases [Das and Kaufman 2007]. The cost of aluminum was still higher than steel but this was offset by the lower fabrication, transportation, erection, and maintenance costs [Siwowski 2006]. Between 1958 and 1965, five major structures were built using aluminum alloys in the United States. Newer aluminum alloys used at the time provided excellent corrosion resistance and were easy to weld. As the steel supply returned following this period, the use of aluminum tapered off, mainly because of the lack of codes and specifications for use when considering aluminum as a design option [Arrien et al 2001].

The use of aluminum in bridges in Europe has also been limited historically. Early use of aluminum in Europe commenced at the same time aluminum bridges were being constructed in North America. In the late 1940s, the first use of aluminum in bridges in Europe included two bascule bridges in the United Kingdom. In 1956, aluminum in bridges for vehicular traffic first appeared in Germany. Rehabilitation projects for two suspension bridges in France made use of aluminum alloys in the early 1970s. After the first uses of aluminum alloys mentioned above, more structures were built, but mainly only in Europe. A majority of the structures that were subsequently constructed in Europe were pedestrian bridges, which serves as the main differing development in Europe as opposed to North America. Many pedestrian bridges using aluminum alloys also exist in Japan, but the use of aluminum in vehicular bridges is still non-existent [Okura 2003]. Increases in the cost of aluminum

alloys in the late 1960s caused the use of aluminum in bridges to diminish considerably. It was not until the early 1990s when the cost of aluminum alloys fell that aluminum was re-considered as a material for bridge construction [Siwowski 2006].

After a period where aluminum was essentially not used in bridge construction, aluminum is being explored again as a possible design option for bridge structures, specifically in Scandinavian countries and the United States. Deck replacement systems for bridge rehabilitations are in use in Sweden and the United States and an all-aluminum structure has recently been constructed in Norway. Further developments have produced prototypes for new bridge structures, such as a floating roadway constructed using aluminum in the Netherlands [Siwowski 2006]. Table 2.1 provides a summary of the major milestones for aluminum bridge construction over the past 75 years [Arrien *et al.* 2001, Das and Kaufman 2003, Siwowski 2006].

**Table 2.1: Aluminum bridges in North America and Europe**

Location	Bridge Type	Use	No. of Lanes	Span (m)	Year	Alloy
Smithfield Street Bridge Pittsburgh, PA, USA	Steel truss bridge w/ orthotropic aluminum deck	Vehicular+Trolley	2+2 Tracks	111, 111	1933, 1967	2014-T6 (1933) 6061-T6 (1967)
Grasse River Bridge Massena, NY, USA	Riveted plate girders	Railway	1 Track	30.5	1946	2014-T6
Hendock Dock England	Riveted double leaf bascule	Vehicular/Railway	1+1 Track	37	1948	2014-T6 6151-T6
Arvida Bridge Arvida, QC, Canada	Riveted arch bridge	Vehicular	2	5@6.1, 88, 5@6.1	1950	2014-T6
Aberdeen Bridge Scotland	Riveted double leaf bascule	Vehicular/Railway	1+1 Track	30.5	1953	2014-T6 6151-T6
Lunen Bridge Germany	Riveted Warren Truss	Vehicular	1	44	1956	6351-T6
Route 86 over I-80 Des Moines, IA, USA	Concrete slab on welded aluminum plate girders	Vehicular	2	12, 21, 21, 12	1958	5083-H113
Banbury Bridge England	Riveted bascule	Vehicular	1	3	1959	6351-T6
I-495 above the Jerico exchange Jerico, NY, USA	Concrete slab on riveted aluminum plate girders	Vehicular	4 (2 Bridges)	23	1960	6061-T6
Route 36 (Appomattox River) Petersburg, VA, USA	Concrete slab on aluminum bolted triangular box girder	Vehicular	2	30	1961	6061-T6
Gloucester Bridge England	Riveted bascule	Vehicular	1	12	1962	6351-T6
Route 110 above Sunrise Hwy Amityville, NY, USA	Concrete slab on aluminum riveted triangular box girder	Vehicular	6 (2 Bridges)	9, 23, 23, 9	1963	6061-T6
Route 32 (Patapsco River) Sykesville, MD, USA	Concrete slab on aluminum riveted triangular box girder	Vehicular	2	28, 29, 32	1963	6061-T6
Saone River Bridge Montmerle, France	All-aluminum truss	Vehicular	N/A	79.9, 79.9	1973	A-SGMT 6
Rodan River Bridge Groslee, France	Concrete slab on aluminum truss	Vehicular	N/A	174	1977	6082-R31
Chamalieres Bridge Chamalieres, France	Aluminum girder	Vehicular	4	N/A	1978	N/A



Some of the significant aluminum bridge structures shown in Table 2.1, are further discussed to provide more detail on the specific key aluminum bridge projects in the past.

#### 2.2.2.1 Smithfield Street Bridge, Pittsburgh, PA, USA

The first documented use of aluminum in North America was the rehabilitation of the Smithfield Bridge in Pittsburgh, Pennsylvania, USA. The structure was built in 1882 and is a steel truss bridge with two 111 m spans spanning the Monongehela River, originally having a wooden deck supported by steel stringers. In 1933, the deck had deteriorated, thus both the wooden deck and steel stringers were replaced with an aluminum deck and asphalt wearing surface. By replacing the deck with a light weight aluminum alloy structure, the dead load was reduced, allowing for an increase in the bridge's carrying capacity by 3.5 times its original design [Siwowski 2006]. The riveted orthotropic aluminum deck was constructed using 2014-T6 aluminum alloy plate; which was a widely-used high-strength aluminum alloy at that time, but does not possess the corrosion resistance of aluminum alloys available today. With the increased live-load carrying capacity, the bridge could accommodate two-lanes of automobile traffic and two tracks for electric trolleys in both directions. The riveted orthotropic aluminum deck was in service for 34 years with no problems until it was replaced in 1967 to again increase the live load capacity of the bridge.

The 1967 rehabilitation consisted of the replacement of the riveted orthotropic aluminum deck with a welded orthotropic aluminum deck. The aluminum alloys used in the deck were 5156-H321 plate, offering higher corrosion resistance, which was welded to 6062-T6 extrusions and bolted to the existing superstructure. With the new aluminum deck, the bridge could accommodate an increased volume of vehicles and trolleys as well as higher live loads such as trucks and larger trolleys. The welded orthotropic aluminum deck was in service until 1993 with no problems until it was replaced with a steel deck. At that time, a life-cycle cost analysis was not completed and steel was the lowest initial cost option [Das and Kaufman 2007].



**Figure 2.2: Smithfield Street Bridge in Pittsburgh, PA [Hecker 2003]**

#### 2.2.2.2 Grasse River Bridge, Massena, NY, USA

The first all-aluminum bridge constructed in the United States was completed by the Aluminum Company of America (Alcoa) in 1946. The bridge accommodated railroad traffic on a line to the Massena smelter at the Alcoa plant in Massena, NY. The structure is a seven span railroad bridge servicing a single track with all but one span constructed using steel. The single all-aluminum span is 30.5 m in length, weighing less than half of a similar steel span and consists of two plate girders with riveted connections [Siwowski 2006]. Constructed around the same time as the Arvida bridge, similarly the same 2014-T6 aluminum alloy was used in the plate girders providing good strength resistance but poor protection from corrosion [Das and Kaufman 2007].

#### 2.2.2.3 Arvida Bridge, Arvida, QC, Canada

The first highway bridge constructed entirely of aluminum is located in Arvida, Quebec, Canada. Erected by the Aluminum Company of Canada (Alcan) in 1950, the bridge has multiple approach spans of 6.1 m with the main span of the riveted arch bridge being 88.4 m long and 14.5 m high. The bridge has a width of 9.75 m, with the total length spanning the Saguenay River in Quebec being 153 m. At the date of construction, the aluminum alloys available today that have strong resistance to stress and corrosion were not available. Thus the chosen alloy, 2014-T6, provided good strength but poor corrosion resistance [Arrien *et al.* 2001]. The superstructure of the bridge is an arch supporting an aluminum grid consisting of longitudinal stringers and cross-beams, which in turn supports a reinforced concrete deck. Aluminum was used in all supports for the superstructure. Weighing approximately 150 tons, the bridge is still in service today and remains the longest aluminum bridge

in the world [Siwowski 2006]. The bridge services distribution to the refining and smelting plants of Alcan and seemingly provides a working demonstration of the capabilities of aluminum in bridges [Das and Kaufman 2007].



**Figure 2.3: Arvida Bridge in Quebec, Canada over the Saguenay River [CSCE 2005]**

#### 2.2.2.4 Other Early North American Aluminum Bridges

In the 1950s and 1960s, during the height of the construction of the interstate highway system, the price of steel was rising and availability of steel was less. This brought about the use of aluminum in highway bridge structures in the United States at this time. In the period from 1958 to 1967 five major bridge structures were constructed using aluminum opposed to traditionally used steel [Das and Kaufman 2007].

The first two bridges constructed using aluminum used a conventional design of built-up plate girders. The first was constructed in Des Moines, Iowa and consisted of a four-span structure supporting two lanes of traffic on 86<sup>th</sup> Street over I-80 (Table 2.1). The superstructure was constructed of welded 5083-H113 aluminum plate girders supporting a concrete deck slab. The bridge remained in service until 1993 when, due to a re-design of the intersection, a bridge was no longer required at that location. When the bridge was removed, tensile and fatigue tests of the bridge components were conducted. It was concluded that after 40 years of service all of the aluminum components tested had similar properties as when the structure was built. The second bridge, constructed in 1960, was a twin structure including two single-span bridges each supporting two lanes of traffic on the I-495 in Jericho, New York (Table 2.1). The superstructure was constructed of

riveted 6061-T6 aluminum plate girders supporting a concrete deck slab. The structure was re-designed and replaced in 1992.

The last four aluminum bridges constructed during this period used the *Fairchild design* which consisted of a riveted and stiffened triangular box girder. To validate the structure, testing of a 50 foot (15.2 m) full-scale bridge using the *Fairchild design* was conducted at Lehigh University. Testing a full-scale bridge confirmed that by utilizing an optimized aluminum superstructure, the dead load can be significantly reduced, allowing for a lighter substructure and a cost reduction in transportation and erection of the bridge [Das and Kaufman 2007].

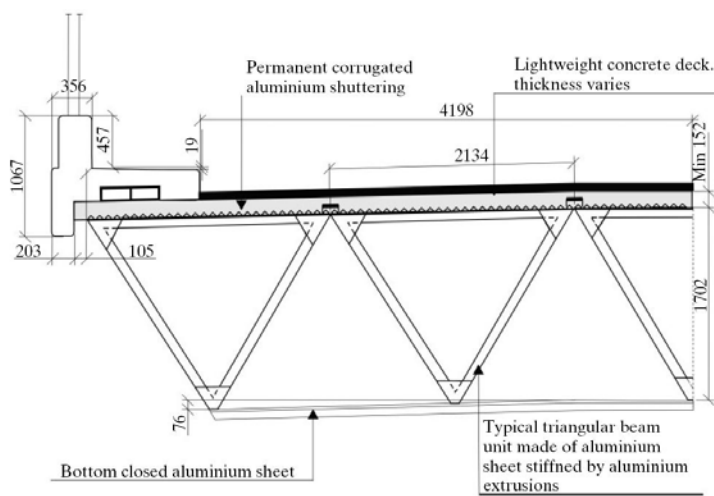


**Figure 2.4: Fairchild Bridge Design [Siwowski 2006]**

In 1961, the first bridge using the *Fairchild design* was constructed in Petersburg, Virginia (Table 2.1). The single span bridge accommodated two lanes of traffic on Route 36 over the Appomattox River. The superstructure was constructed using 2.5 mm 6061-T6 aluminum sheet. The second bridge using this girder system was constructed in Sykesville, Maryland and was a three span structure carrying two lanes of traffic on Route 32 over the Patapsco River (Table 2.1). The bridge was in service until 2004 when replaced by a new steel structure. The cause for replacement was noted as galvanic corrosion between the aluminum components and the steel bearings, as well as pitting corrosion in the girders, as no drainage was implemented in the hollow sections. The final two structures that used the *Fairchild design* were built in Amityville, New York, each four-span structure supporting three lanes of traffic on Route 110 over the Sunrise Highway (Table 2.1). Similar to the structure in Sykesville, MD the bridge has deteriorated over its service life, but it has been proposed to rehabilitate the structure.

### 2.2.2.5 Early European Aluminum Bridges

Use of aluminum in bridges structures in Europe started around the same time as in North America. In the late 1940s, the first aluminum bridges in Europe were constructed in the United Kingdom. The Sunderland bridge and Aberdeen bridge were built in 1949 and 1953, respectively. Both truss girder bascule bridges were built to accommodate one lane for vehicular traffic and one line of rail (Table 2.1). All truss chords and diagonals were made of 6151-T6 aluminum and connected using galvanized steel rivets. The aluminum deck for both structures was made of 2014-T6 aluminum consisting of two longitudinal stringers with cross-beams covered by aluminum plate and an asphalt wearing surface. By using aluminum in these cases the dead weight of the structures were reduced by approximately 40% as compared to a similar steel structure [Das and Kaufman 2007].

In 1956, the first aluminum bridge in Germany was constructed in Lunen. The riveted Warren truss bridge built entirely of aluminum was a single span structure supporting one lane of vehicular traffic (Table 2.1). Truss elements consisted of special extruded shapes using 6351-T6 aluminum. The deck was fabricated using riveted aluminum extrusions, which was riveted to aluminum stringers. In the early 1970s, two road bridge replacements in France utilized aluminum for the structure. The first structure was a two-span suspension structure over the Saone River in Montmerle made of steel and timber, which was replaced by truss structure using all-aluminum suspended by the existing pylons (Table 2.1). The truss elements were made of extruded aluminum and the deck consists of extruded stringers and welded aluminum cross-beams with a special composite plate as the wearing surface. The second structure, built over the Rodan River in Groslee, was a replacement of the 174 m suspended span constructed of steel and wood with three aluminum trusses and a concrete deck. The new structure used 6082-R31 aluminum alloy for the truss elements (Table 2.1). Other road bridges were constructed in Europe such as the Newcastle bridge and Gloucester bridge in England as well as in Chamaliere, France (Table 2.1). Many of the other aluminum bridge structures in Europe service pedestrian traffic and will not be discussed further here [Siwowski 2006].

### 2.2.2.6 Recent Aluminum Bridge Developments

After a decline in the cost of aluminum in the 1990s, there have been movements in Scandinavian countries and the United States to use aluminum in bridges again. In Sweden, a bridge deck system called *Sapa Front* or *Svensson Deck* uses lightweight aluminum deck panels to replace existing steel and concrete composite decks (Figure 2.5). The deck system uses 6063-T6 aluminum alloy extrusions which fit together by a tongue and groove connection to form an orthotropic deck plate. The

extrusions, which consist entirely of aluminum, are placed perpendicular to the direction of traffic and come in small sections, which can be simply snapped together and bolted down to the existing superstructure, thus requiring no welding. The deck system has been used for bridge deck replacements for 20 years on more the 35 structures [Arrien et al 2001, Siwowski 2006].

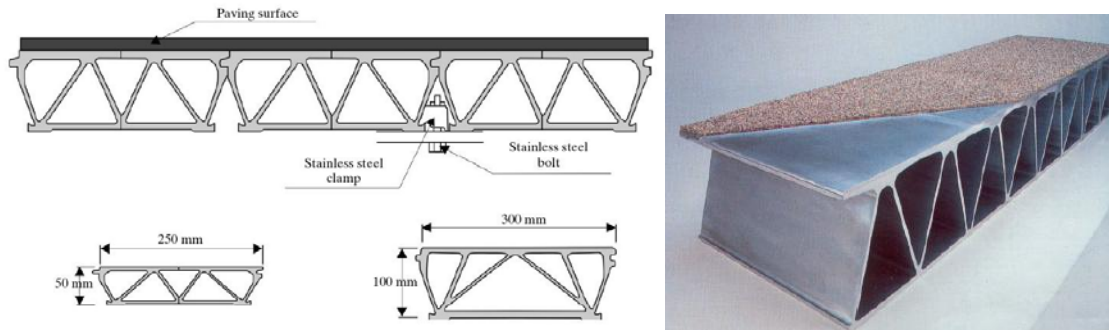


**Figure 2.5: Svensson Deck (left) and Alumadeck (right)**

Also, around this time a different bridge deck system was developed by the Reynolds Metal Company in the United States called the Alumadeck (Figure 2.5). The Alumadeck is an orthotropic deck plate comprised of 6063-T6 aluminum hollow extrusions using a 3/8" (9.5 mm) thick epoxy layer with aggregate for a wearing surface. This deck system has been implemented for two bridge structures in the United States. The first was a rehabilitation for a suspension bridge with a steel deck spanning 320 ft (97.5 m) over the Juniata River near Huntington, Pennsylvania. The new all-aluminum superstructure consisted of 6061-T6 extruded I-beams which supported multiple deck sections placed perpendicular to traffic and welded together at the top flange. The second structure, in Clarksville, Virginia, on Route 58 over Little Buffalo Creek also used the Alumadeck system except the extrusions were oriented parallel to traffic and supported by the existing four longitudinal steel girders, welded on the top and bottom flanges [Das and Kaufman 2007].

The above cases are limited to bridge deck replacements. In 1996, the most recent case of an all-aluminum bridge installation for vehicular traffic was completed in Forsmo, Norway; whereby the existing steel girder bridge with a concrete deck was replaced with two aluminum box girders. The box girders span 39 m using 6082 and 6005 aluminum alloys, and are placed longitudinally with the top flange serving as the bridge deck (Figure 2.6).



**Figure 2.6: All-aluminum bridge in Norway (left) and floating bridge in Netherlands (right) [Siwowski 2006]**

Another new development in the Netherlands is the construction of a single lane floating bridge near Hedel in 2003 (Figure 2.6). The structure consists of rectangular aluminum modules filled with polystyrene, connected together forming a stiff road bridge spanning 70 m. The bridge modules are anchored into the riverbed using steel pipe piles. A 10 m wide drawbridge can also be installed to allow the passage for watercraft [Siwowski 2006].

### **2.3 Fatigue of Aluminum Welds**

In aluminum structural components, the welds are highly susceptible to fatigue damage, thus the structural design of an aluminum component may be controlled by the fatigue resistance of the welds. The fatigue resistance of a weld is a function of the weld geometry, weld defects, residual stresses, and mechanical properties of the weld metal, heat affected zone, and base metal [Burk and Lawrence 1978]. In welded structures subjected to repeated loading there is potential for the propagation of cracks over time. Cracks generally originate at locations where there is a change in geometry, such as a weld toe, because these sites have higher stress concentrations than the parent metal. In general, the more severe the change in geometry (or detail category), the higher the stress concentration, and thus, the lower the fatigue strength. Fatigue may be a concern in aluminum structures in particular, because the absolute fatigue strength is lower than that of steel. The heat generated during the welding process lowers the strength of the aluminum by removing the effects of cold-working [Gitter 2006]. The welding process imposes tensile residual stresses on the structure due to differential cooling in the weld metal and the parent material. Increasing tensile residual stresses in the weld generally result in decreased fatigue strength [Menzemer and Fisher 1993]. In the 1990s, three major testing programs were conducted on the fatigue behaviour of aluminum weldments in the United States and Europe, and are discussed in this chapter.

### 2.3.1 Comparing CA and VA Fatigue Test Data

Design S-N curves provide a relation between a nominally applied stress range,  $\Delta S$ , and the number of stress cycles to failure,  $N$ . Under constant amplitude loading, the maximum and minimum stresses define the stress range and  $R$ -ratio. Fatigue resistance curves are provided for specific detail types including plain members, different welded connection types, and bolted connections.

The Palmgren-Miner linear damage rule is used by many design codes and specifications in conjunction with design S-N curves to determine fatigue life. These expressions are provided below,

$$\Delta S = S_{\min} - S_{\max} \quad (2.1)$$

$$R = \frac{S_{\min}}{S_{\max}} \quad (2.2)$$

$$\text{Failure Criterion: } \sum \left( \frac{n_i}{N_i} \right) = 1.0 \quad (2.3)$$

$$N_f = \sum n_i \quad (2.4)$$

where  $N_f$  is the number of cycles to failure,  $n_i$  is the number of cycles at each stress range  $i$ , and  $N_i$  is the number of cycles for a design S-N curve at stress range  $i$  that constitutes failure. Failure is defined by the summation of all applied stress ratios equal to 1.0 [Stephens *et al.* 2001].

Many design codes and specifications use a constant amplitude fatigue limit (CAFL) in the fatigue life calculation, which defines that any stress cycles applied below this limit are non-damaging. If all stress cycles applied in the full spectrum of loading are below the CAFL a fatigue life calculation is not required in many cases. The Palmgren-Miner rule holds true for constant amplitude loading, but is not directly applicable to variable spectrum loading.

Under variable amplitude loading, different stress ranges are imposed either in blocks or with each successive stress cycle. An equivalent or characteristic constant amplitude stress range is required to present variable spectrum loading on design S-N curves. One of the most common approaches employs Miner's sum and takes the following form,

$$\Delta S_{eq} = \left( \frac{\sum n_i \cdot \Delta S_i^m}{\sum N_i} \right)^{1/m} \quad (2.5)$$



where  $\Delta S_{eq}$  is the equivalent constant amplitude stress range,  $\Delta S_i$  is the stress range at  $i$ ,  $n_i$  is the number of cycles for a given stress range  $i$ ,  $N_i$  is the number of cycles to cause failure under stress range  $i$ , and  $m$  is the slope of the design S-N curve.

Another approach commonly used in bridge applications is to calculate a characteristic constant amplitude stress range by applying and removing a known load to the structure, which is representative of the true in-service VA loading in the sense that fatigue failure under the constant amplitude stress range due to the imposed characteristic load should occur in the same number of cycles as the under the true VA loading. Many design codes use this approach. For example in CSA-S6 and AASHTO characteristic stress ranges are determined by *driving* a single code design truck over the bridge and recording the maximum and minimum stress at the critical location. This stress range is then multiplied by a correction factor (0.52 in CSA-S6 or 0.75 in AASHTO) to ensure that the fatigue damage imposed by the code truck and real traffic will be similar. The corrected stress range due to the code truck is then compared with design S-N curves to determine design life (Figure 2.7). As discussed in [Walbridge and Coughlin 2009] the fatigue correction factors have been calibrated assuming  $m = 3$ , which is a typical assumption for steel.

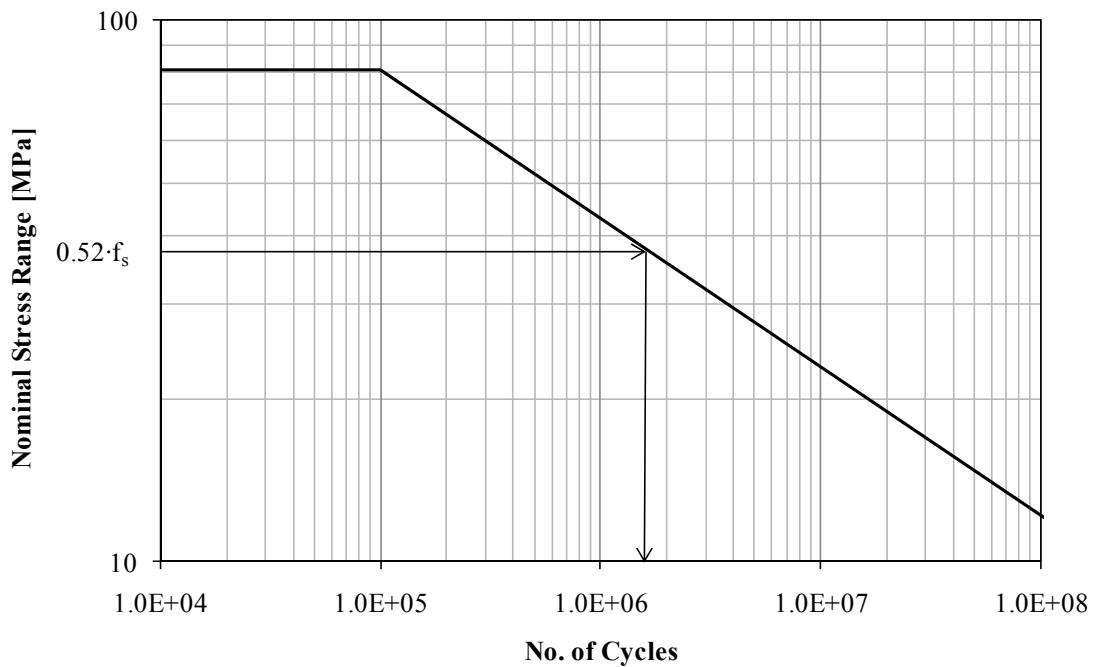


Figure 2.7: Characteristic CA stress range representation

### 2.3.2 Testing at the ATLSS Laboratory at Lehigh University

Menzemer [1992] conducted a series of constant amplitude fatigue tests on both small- and full-scale specimens. 32 small-scale tests were fatigue tested under axial loading for both cover plates and cruciform joints (Figure 2.8). Twelve beams, with geometry shown in Figure 2.8, were tested under four point bending, resulting in test data for 48 cover plate details, 96 stiffeners, and 24 butt splices. The plate thickness and weld dimensions of all small- and full-scale specimens remained constant. The specimens were all fabricated from 5456-H116 aluminum.

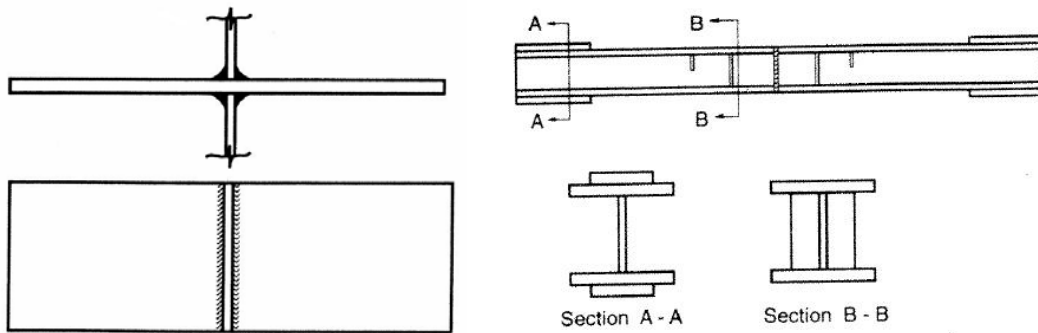


Figure 2.8: Small-scale cruciform joints (left) and full-scale beam specimens (right)

The testing results for the small-scale axial cruciform specimens and the full-scale beam stiffeners were compared, revealing distinct differences between the mean regression lines for the results (Figure 2.9). The difference between the two sets of test data increase as life (cycles) increases. The testing data for the beam stiffeners were also compared to the existing Aluminum Association design curve for Detail Category C at the time of the study. The test data showed this curve to be unconservative; thus, a more conservative design curve was proposed [Menzemer and Fisher 1993].

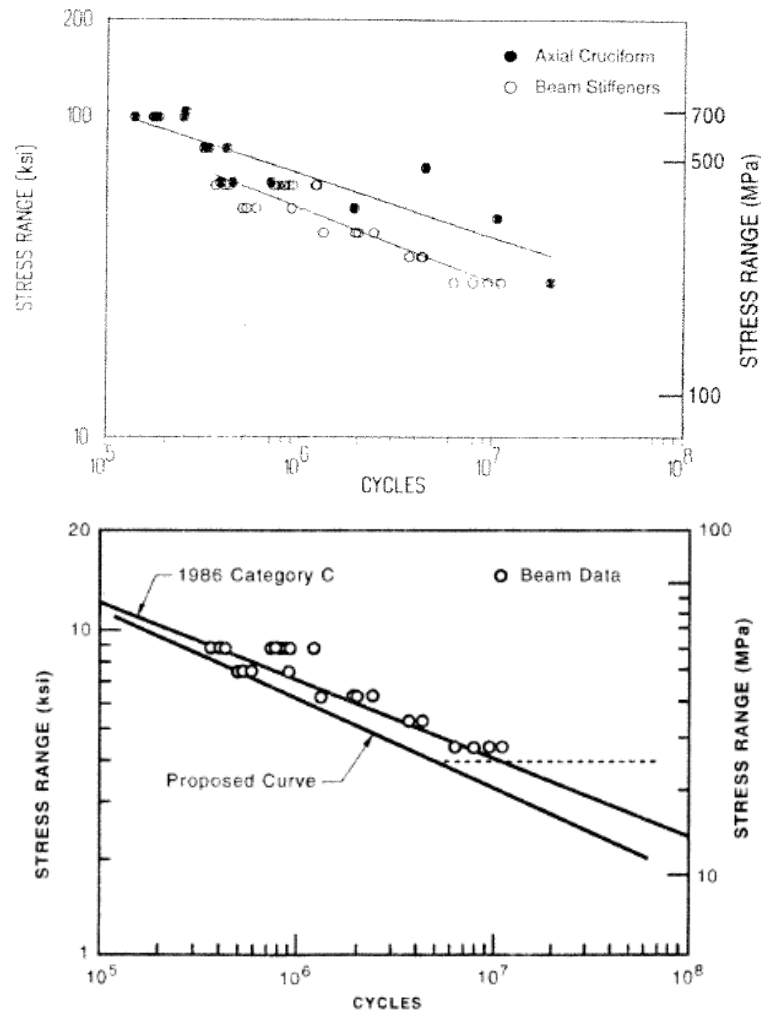


Figure 2.9: ATLSS test data for axial cruciform and beam stiffeners [Menzemer and Fisher 1993]

The fatigue resistance of aluminum components under variable amplitude loading was predicted using a linear elastic fracture mechanics analysis. In this reference it is noted that test data for aluminum weldments under variable spectrum loading is scarce. Testing under variable amplitude loading is thus noted as a recommended area of future work.

### 2.3.3 Testing for the ERAAS Fatigue Document

Jaccard *et al.* [1995] discuss the testing conducted for the creation of the European Recommendations for Aluminum Alloy Structures (ERAAS) Fatigue Design document. The tests were conducted mainly on full-scale specimens with data provided by Alusuisse-Lonza Services, Austria Metal

(AMAG), and Technische Universität München (TUM). Tests using small-scale specimens were used to differentiate the impacts of R-ratio and plate thickness,

A total of 1247 tests were conducted in this series including 983 tests by Alusuisse, 90 tests by AMAG, and 174 tests by TUM. Not all of the tests from Alusuisse were considered in this study and an additional series of tests were conducting by TUM on full-scale specimens providing another 361 test results. In total, the testing program completed included 282 tests for non-load carrying fillet welded transverse beam stiffeners tested under constant amplitude loading between a stress range,  $\Delta S$ , of 60 MPa and 100 MPa and plotted against ERAAS Detail Category E1-35 N/mm<sup>2</sup> for full and half stiffeners (Figure 2.10). Jaccard *et al.* [1995] note that longer lives were experienced for *R*-ratios of -1.0 compared to an *R*-ratio of 0.1 and found no differences in behaviour between full and half stiffeners. A wide scatter band of testing data and the lack of testing beyond lives of 10<sup>6</sup> cycles is evident. For a non-load carrying fillet welded stiffener a proposed slope of  $m = 3.37$  for 35 N/mm<sup>2</sup> at  $2 \times 10^6$  cycles was concluded from testing data. At this time, concurrent to testing of aluminum at these institutions, testing was also underway for welded aluminum at EPF-Lausanne, and at TNO-Delft. Testing data from all available sources was reviewed in the development of the ERAAS fatigue design curves [Jaccard *et al.* 1995].

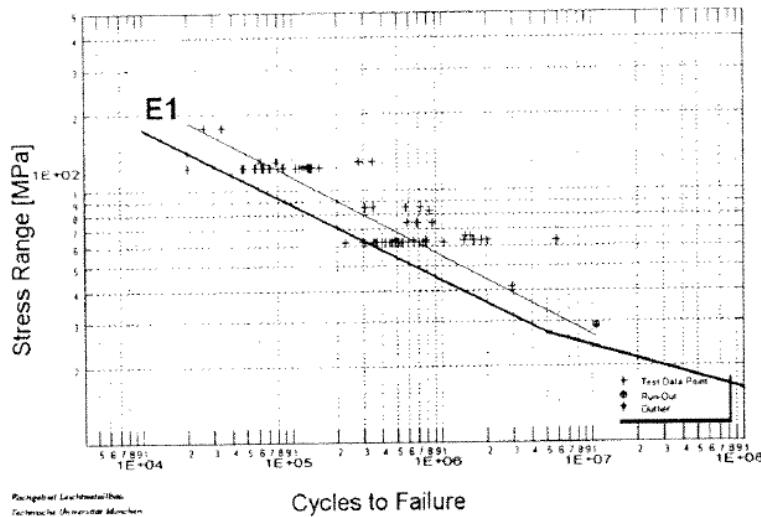


Figure 2.10: ERAAS test data for a non-load carrying web stiffener [Jaccard *et al.* 1995]

### 2.3.4 EUREKA Research Project

A research project was undertaken in 1989, EUREKA project EU 269 – Design of Aluminum Structures under Fatigue Loading, to further expand the knowledge of fatigue design for aluminum. The project was completed with assistance from multiple laboratories in Spain, Portugal, Italy, Denmark, Great Britain, and The Netherlands. Three different joining types were examined in this study, including welded, adhesive-bonded, and bolted. Welded joints were the focus of the study as they were considered to be the predominant joint type for aluminum structures. For the purpose of this study, only the research on welded joints will be discussed herein. Fatigue testing of welded aluminum joints was limited to four detail types using both small- and large-scale specimens fabricated from 6061-T6 aluminum (Figure 2.11).

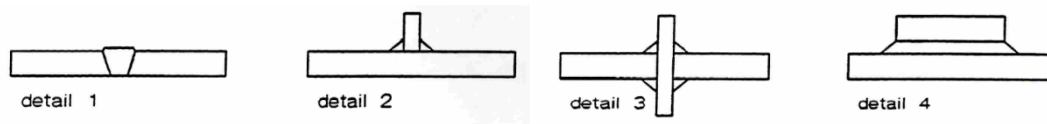


Figure 2.11: Fatigue details tested for the EUREKA research program

In addition to the consideration of differing detail types, plate thicknesses of 6, 12, and 24 mm were tested to quantify thickness effects on fatigue. Most testing was conducted under constant amplitude loading with an  $R$ -ratio of 0.1, with a smaller sample of additional tests performed under variable amplitude loading to investigate the impact of spectrum loading. The tested fatigue lives ranged from  $10^4$  to  $10^7$  cycles. Comparisons are provided below between small- and large-scale test results as well as tests under constant and variable amplitude loading (Figure 2.12, Figure 2.13, Figure 2.14).

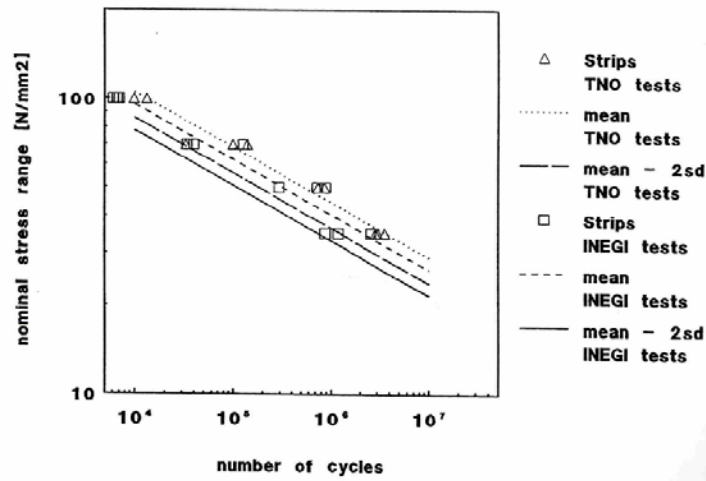


Figure 2.12: EUREKA test data for a cruciform joint with  $t = 12$  mm [Soetens *et al.* 1995]

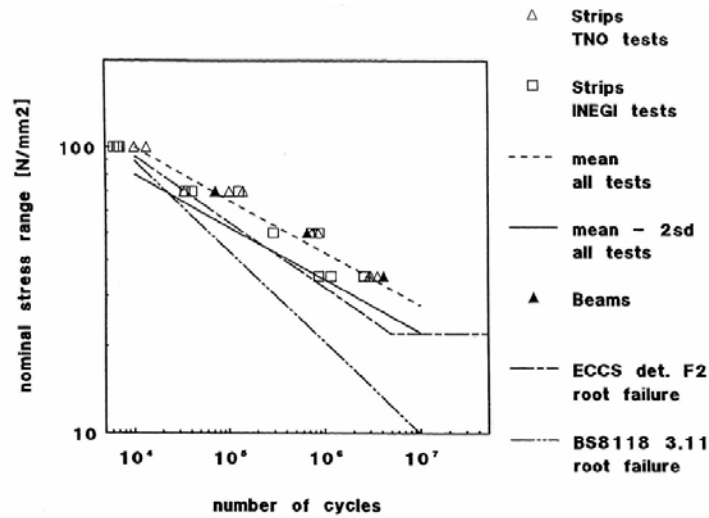


Figure 2.13: EUREKA test data for cruciform joint and beam stiffeners [Soetens *et al.* 1995]

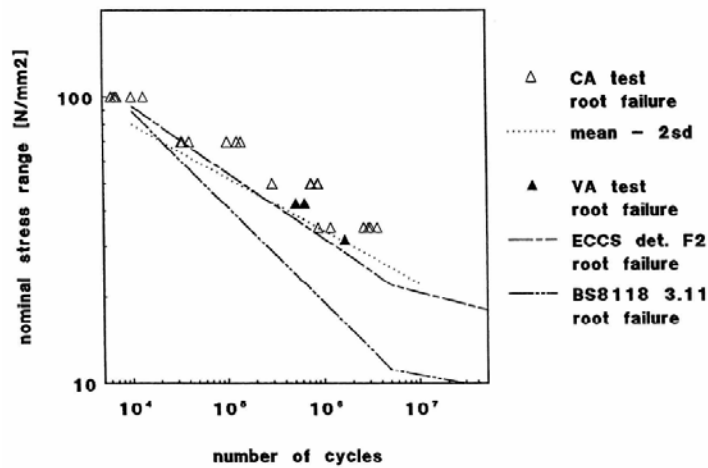


Figure 2.14: EUREKA CA/VA test data for a cruciform joint with  $t = 12$  mm [Soetens *et al.* 1995]

A fairly wide scatter in the testing data is apparent in all cases. The testing data shows a difference in fatigue life between small- and large-scale tests [Soetens *et al.* 1995].

## 2.4 Current Design S-N Design Curves

Several codes and specifications are available for the fatigue design and analysis of welded aluminum structures. The design codes and specifications from the following sources are discussed in this section: the Canadian Standards Association (CSA), The Aluminum Association (AA), the British Standards Institute (BSI), the European Committee for Standardization (CEN), and the International

Institute of Welding (IIW). All of these codes and specifications employ design S-N curves to characterize the resistance of aluminum fatigue details.

In the following sections, the similarities and differences of the design S-N curves used in each of the above-mentioned codes or specifications are discussed.

### 2.4.1 Canadian Standards Association

The only design code in Canada currently available for the design in aluminum structures is *Canadian Standards Association: Strength Design in Aluminum (CAN/CSA-S157-05)*. The most recent version of CAN/CSA-S157-05 (CSA-S157) was published in 2005. For the purpose of fatigue design, seven detail categories are specified in this code. The corresponding design S-N curves are illustrated in Figure 2.15.

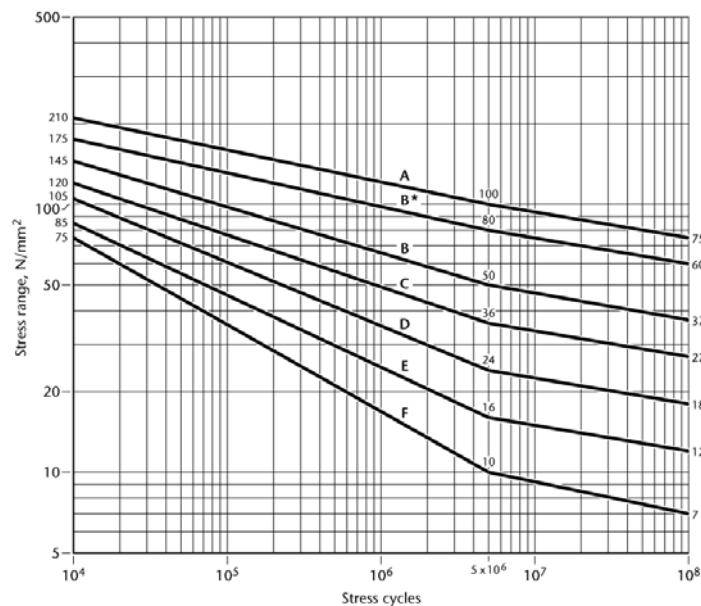


Figure 2.15: CSA-S157 design S-N curves [CSA 2005]

Each detail categories design S-N curve has a different initial slope,  $m$ , ranging from 3.08 to 8.38, but each has a constant amplitude fatigue limit at  $5 \times 10^6$  cycles. For longer fatigue lives under variable amplitude loading, the design curves have a second slope,  $m'$ , common to all detail categories of 10.41, excluding Detail Categories B and F which have second slopes,  $m'$ , of 9.95 and 8.40, respectively. The code states that the design curves in Figure 2.15 (with CAFL at  $5 \times 10^6$  cycles) can be used where cyclic stress ranges are of a constant amplitude.

For variable amplitude load spectra, the design curves can be used in accordance with the Palmgren-Miner's rule for cumulative damage. If all of the stress ranges in the variable amplitude stress spectrum fall below the CAFL (that is, the stress range at  $5 \times 10^6$  cycles), the code states that an infinite fatigue life can be assumed. It is understood that these curves were not statistically calibrated and represent a lower bound solution [Sharp *et al.* 1996].

## 2.4.2 The Aluminum Association

In the United States, design codes available for the design of aluminum include *The Aluminum Association: Aluminum Design Manual* (ADM 2005) and the *AASHTO LRFD Bridge Design Specification* (AASHTO). The most recent edition of ADM 2005 was published in 2005 and serves as the main source for the design of aluminum in the United States of America (*Note: a new version of this manual was just released in 2010, shortly after the writing of this thesis had commenced*). AASHTO follows similar design guidelines as prescribed by ADM 2005, but provides additional provisions as required for the design of bridges. For fatigue design of aluminum welded details, mechanically fastened joints, and plain members, ADM 2005 provided a set of six detail categories, along with corresponding single-slope design S-N curves for characterizing fatigue resistance (Figure 2.16).

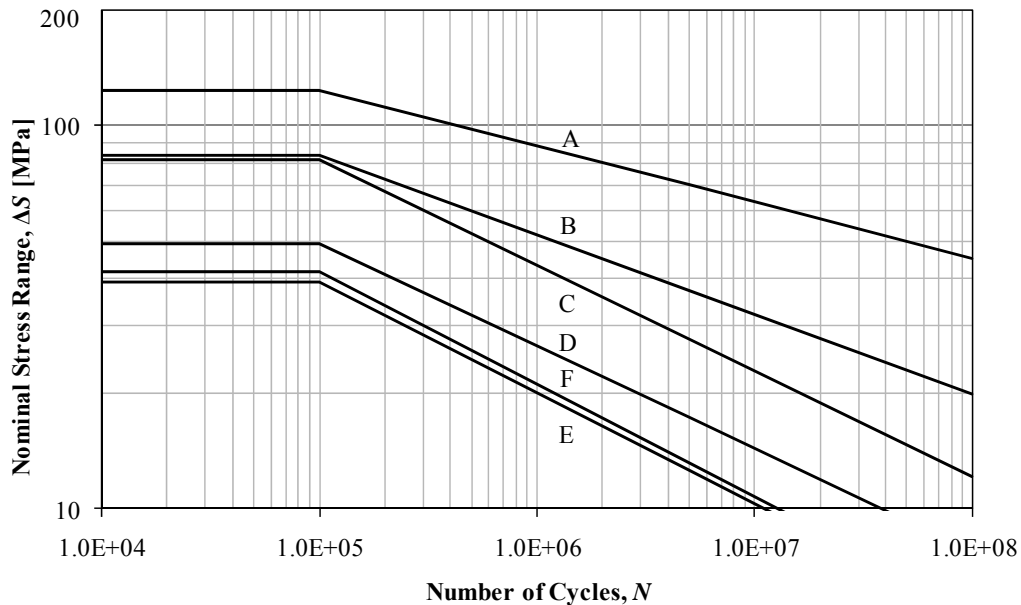
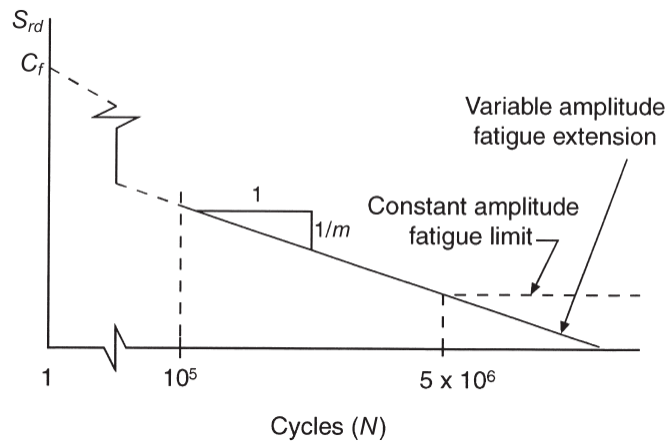


Figure 2.16: ADM 2005 design S-N curve [AA 2005]



ADM 2005 design curves were derived through the analysis of test data from ATLSS Laboratory at Lehigh University and the Technical University of Munich, with predominance placed on test data from full- or large-scale tests. Lower bound curves were fit to the testing data representing 95% confidence for a 97.5% probability of survival [Menzemer and Fisher 1993].

Each detail category utilizes a different design S-N curve slope,  $m$ , ranging from 3.42 to 6.85. Under constant amplitude loading, if the applied stress range is less than the allowable stress range (Figure 2.16) the fatigue resistance of the detail is adequate. Consideration of fatigue is not required if the applied constant amplitude stress range is less than the CAFL. ADM 2005 uses a constant amplitude fatigue limit at  $5 \times 10^6$  cycles, but unlike CSA-S157, a second slope beyond the CAFL for variable amplitude loading analysis is not used. The Aluminum Association takes a conservative approach in the formulation of the design S-N curve by using a variable amplitude fatigue extension which simply extends past the CAFL at the same slope. Menzemer and Fisher [1993] note that many life prediction models support a different slope beyond the CAFL, but with limited testing data under variable amplitude loading, a conservative approach is taken.



**Figure 2.17: ADM 2005 design S-N curve representation [AA 2005]**

Under variable amplitude loading, similar to CSA-S157, ADM 2005 states that if the maximum stress range is less than the CAFL, then it is not required to consider the effects of fatigue (i.e. the fatigue life is effectively infinite). To determine the effects of the cumulative damage from variable loading spectra, the use of a Palmgren-Miner's rule (in a slightly rearranged format) is recommended [AA 2005].

### 2.4.3 European Committee for Standardization

The design of aluminum structures in Europe is performed using *Eurocode 9 Design of aluminum structures: Structures susceptible to fatigue* (prEN 1999-1-3), which was issued in 2006. Part 1-3 of prEN 1999-1-3 (Eurocode 9) outlines design rules for structures that are susceptible to fatigue.

Eurocode 9 was formulated through a collaborative review of design specifications from Britain, France, and Germany, as well as the ERAAS document. Eurocode 9 provides 45 different detail types with 42 associated detail categories for plain members, different weld types, and bolted connections, to determine fatigue resistance. These detail categories originate from 22 stress range levels (design S-N curves in most European standards are identified by the stress range at which the curve crosses  $2 \times 10^6$  cycles) and initial slopes,  $m_1$ , ranging from 3.4 to 7.0. All design S-N curves in the code are two-slope curves, excluding those associated with the detail categories for plain members and bolted connections, which use single-slope curves. When a second slope is warranted beyond the CAFL, the slope is generally taken as:  $m_2 = m_1 + 2$ . The design S-N curves in this code are set at two standard deviations below the mean of experimental data. Figure 2.18 shows the design S-N curves for fillet welds in Eurocode 9.

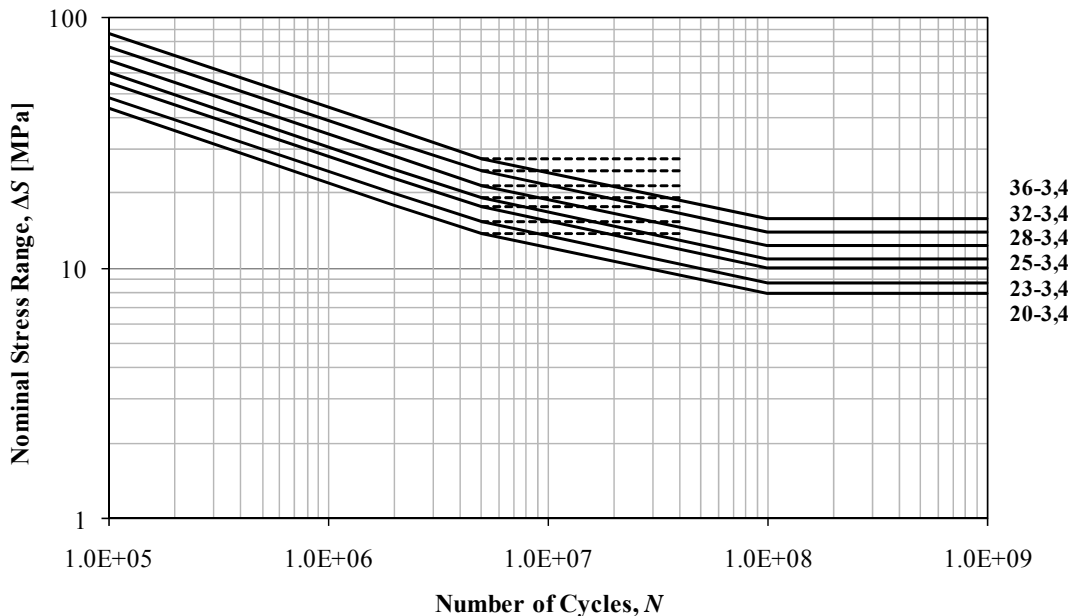


Figure 2.18: Eurocode 9 design S-N curves for fillet welds [CEN 2006]

Six curves are provided for fillet welded details, as shown in Figure 2.18. Each fatigue detail is represented by a two-slope fatigue curve identified by the fatigue strength at  $2 \times 10^6$  cycles (ie. 28 or

28 MPa) and the initial slope (ie. 3,4), denoted on the right of the figure. The constant amplitude fatigue limit for all fatigue details occurs at  $5 \times 10^6$  cycles, except plain members, which have a CAFL of  $2 \times 10^6$  cycles. Although constant amplitude stress cycles below the CAFL are considered non-damaging, the code notes that occasional loading events above this limit will cause a crack to propagate, thus allowing stress cycles under the CAFL to cause further damage. Therefore, the code uses a secondary slope,  $m_2$ , between  $5 \times 10^6$  and  $10^8$  cycles. The code notes that the second slope may be conservative for certain loading spectra. A cut-off limit is also provided in the code at  $10^8$  cycles, thus implying that any stress cycles below this limit cause no damage. For safe life design, the code uses the Palmgren-Miner Rule with the recommendation that the cumulative damage should not exceed 1.0, although the code does offer different levels of allowable cumulative damage in the annex [CEN 2006].

#### **2.4.4 British Standard Institute**

The code of practice for the design of aluminum in Britain is completed using *British Standards Institute: Structural Use of Aluminum* (BS 8118). Published in 1992, BS 8118 provides design methods for the fatigue resistance of aluminum alloys. BS 8118 provides nine detail categories for design, represented by a two-slope fatigue resistance S-N curves with initial slopes,  $m_1$ , ranging from 3.0 to 4.5. The design S-N curves in this code are set at two standard deviations below the mean of experimental data (Figure 2.19).

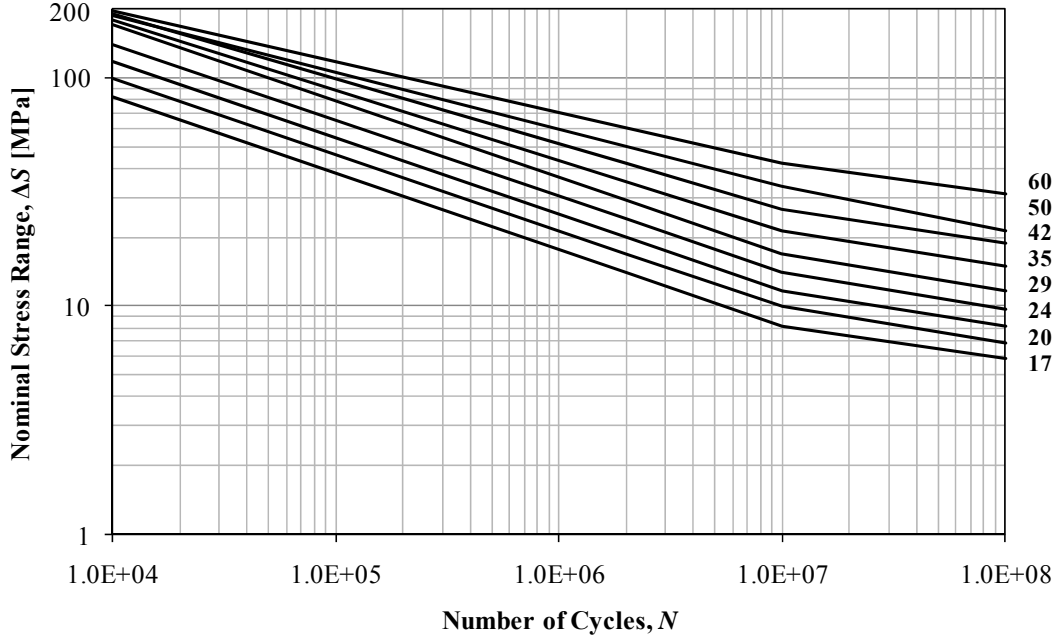


Figure 2.19: BS 8118 design S-N curves [BSI 1992]

Each fatigue detail is represented by a two-slope fatigue curve identified by the details fatigue strength at  $2 \times 10^6$  cycles. The knee point of the design S-N curve is located at  $10^7$  cycles where second slope of  $m_2 = m_1 + 2$  is used up to the variable amplitude cut-off stress at  $10^8$  cycles. The second slope is provided beyond  $10^7$  stress cycles is representative that in a variable load spectrum, stress cycles below the CAFL can be damaging. The constant amplitude cut-off stress or CAFL occurs at  $10^7$  cycles, unlike CSA-S157 and Eurocode 9 where the CAFL occurs at  $5 \times 10^6$  cycles. Safe life design is the design philosophy and the code uses the Palmgren-Miner Rule as the failure criterion for general or variable amplitude loading satisfying the following condition with the recommendation that the cumulative damage cannot exceed 1.0 [BSI 1992].

#### 2.4.5 International Institute of Welding

The *International Institute of Welding: Fatigue design of welded joints and components* (document XIII-1965-03/XV-1127-03 (IIW 1965)) includes recommendations for the fatigue design of aluminum welded joints and components. The IIW 1965 recommendation includes two-slope design S-N curves for 14 detail categories, which are each distinguished by a fatigue class (FAT) corresponding with the fatigue strength at  $2 \times 10^6$  cycles.

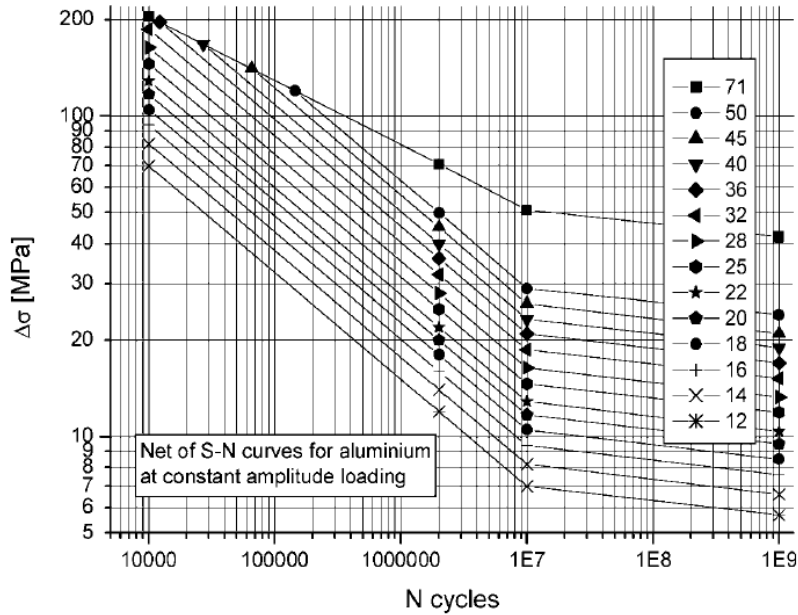


Figure 2.20: IHW design S-N curves under CA loading [Hobbacher *et al.* 2005]

Similarly to (BS 8118), the CAFL for all fatigue classes occurs at  $10^7$  cycles. Unlike all of the other codes discussed in this chapter, all of the curves in the IHW 1965 have a common slope of  $m_1 = 3.0$  up to the CAFL, excluding FAT 71, which has a slope of  $m_1 = 5.0$ . The fatigue resistance of welded components under constant amplitude loading below the CAFL is recognized as being somewhat uncertain. Rather than specifying a horizontal cut-off at the CAFL, as most codes assume, IHW 1965 states that based on past experimental data, this line should be declining gently at a rate of 10% per decade (in terms of cycles) corresponding to a slope of  $m_2 = 22.0$  for constant amplitude loading (see Figure 2.26).

Under variable amplitude loading, the slope,  $m_2$ , beyond the CAFL is modified according to the expression  $m_2 = 2 \cdot m_1 - 1$ . Therefore, for variable amplitude loading, IHW 1965 recommends a second slope of  $m_2 = 5.0$  for all welded fatigue details (Figure 2.21).

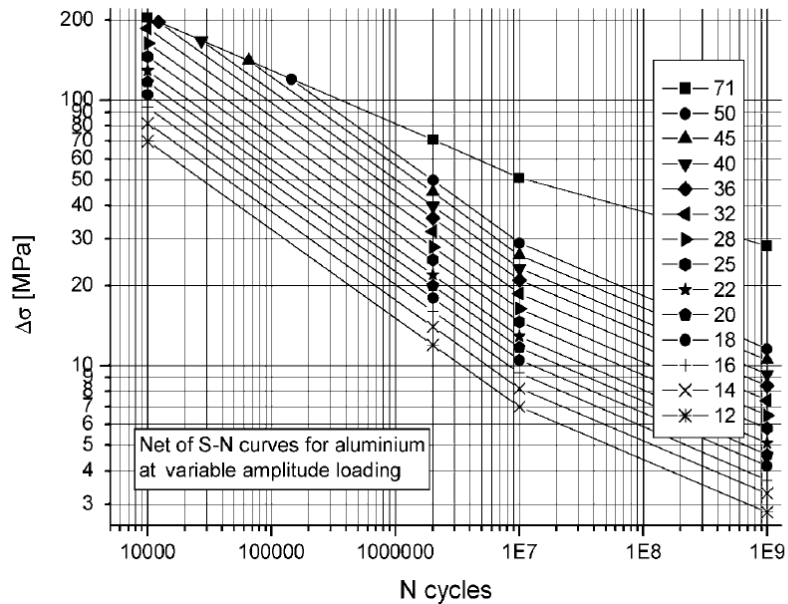


Figure 2.21: IAW design S-N curves under VA loading [Hobbacher *et al.* 2005]

Under variable amplitude loading, a cumulative damage procedure is used where the Palmgren-Miner Rule (with a critical damage index of 1.0) and a design S-N curve for variable amplitude loading (Figure 2.21) are utilized. Although this method is used in many design codes, recent research has indicated that it may be unconservative [Hobbacher *et al.* 2005]. Thus, IAW 1965 recommends using a lower critical damage index of 0.5 instead of 1.0. It is also recommended in certain cases to calculate the equivalent stress range using the constant amplitude fatigue design curve, neglecting the CAFL. As described for the cumulative damage calculation for both CSA-S157 and ADM 2005, if the maximum stress range is less than the CAFL, then an infinite life can be assumed for the welded detail and no further calculation is required. IAW 1965 recommendation notes that under very high cycle loading this approach may not be suitable for aluminum.

#### 2.4.6 Code Comparison for the Design S-N Curve

Design S-N curves from various codes and recommendations for the most common welded aluminum fatigue details have been compared elsewhere. Maddox [2003] provides a review of the most recent design codes and specifications including BS 8118, Eurocode 9, IAW 1965, ADM 2005, and CSA-157. Significant differences are found in the design specifications and recommendations listed above, specifically in the design S-N curves used, classification of details, and differing requirements for the fatigue life calculations. With these differences, the fatigue life of a detail can vary depending on the

code or recommendation used [Maddox 2003]. These significant differences are apparent among the various design standards, although many use the same testing data to calibrate the design curves. These differences are apparent mainly because the knowledge in areas such as the CAFL and variable amplitude spectrum loading is relatively limited, and in general, due to different perspectives on fatigue design [Menzemer 2000].

A summary of the historical developments made in the past for fatigue design is presented by Maddox [2003] to explain the large discrepancies between the design process used in Europe and North America. In the 1970s, the British Standard Institute provided the most complete design standard for aluminum. The development of design rules for fatigue in steels served as a basis for the fatigue design rules and specifications for aluminum, whereby these specifications were formulated based on the differences in elastic modulus between steel and aluminum. The main concerns were that the methods used at that time were too simplistic or conservative and did not provide a true representation of the fatigue resistance of aluminum. Also, the test data from small-scale test specimens used to formulate the design curves did not account for higher residual stresses present in full-scale beams and elements. The formation of the ECCS committee for development of the Eurocode allowed for the creation of a large database containing large-scale test results from projects around Europe, which allowed for revisions to the British Standard, and eventually, the European Standard. Based on the developments made in Europe, fatigue specifications were created and revised by The Aluminum Association and the Canadian Standards Association [Maddox 2003].

Figure 2.22 provides a comparison, compiled for the current study, of design S-N curves from existing codes and recommendations for one detail: a non-load carrying fillet welded transverse stiffener [AA 2005, BSI 1992, CEN 2006, Hobbacher *et al.* 2005, CSA 2005].

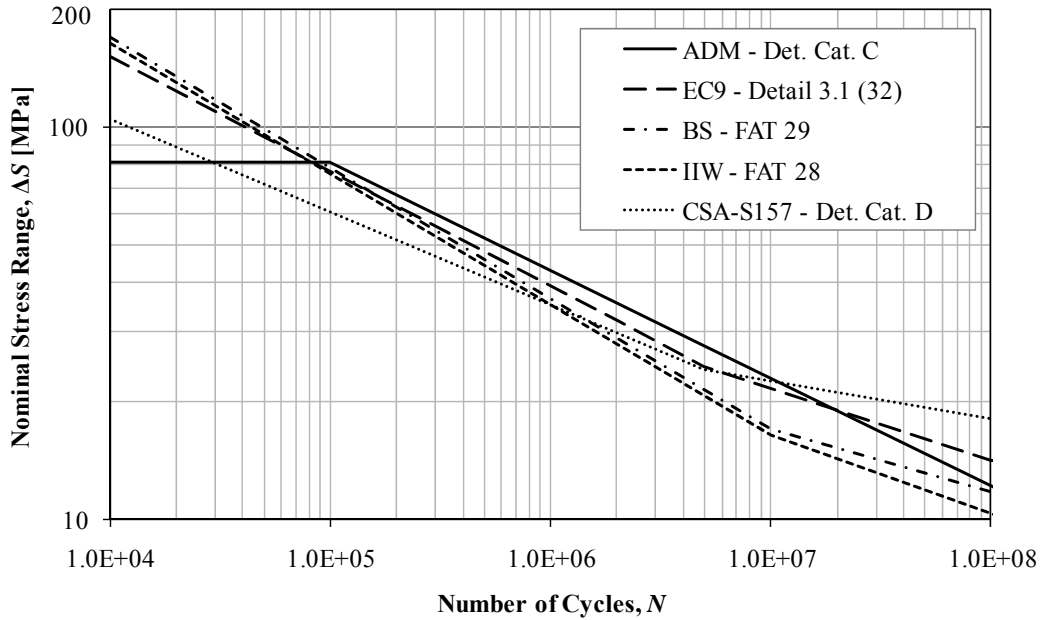


Figure 2.22: Design S-N curve comparison for a non-load carrying transverse stiffener

Differences between the S-N curves are apparent in Figure 2.22 and can be attributed to a lack of fatigue data for full-scale specimens and details tested under variable amplitude loading [Menzemer 2000]. The most apparent difference between the specifications is the use of either a single-slope curve, as used by ADM, or the use of multi-slope curves as adopted by Eurocode 9, BS 8118, CSA-S157, and IIW 1965. ADM 2005 uses a simplified and conservative approach of extending the S-N curve beyond the CAFL at the same slope, while the secondary slope in other specifications is shallower in the high cycle portion of the S-N curve (Figure 2.23).

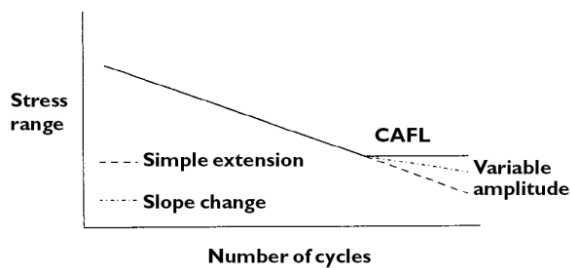


Figure 2.23: Differences between single- and two-slope S-N design curves [Menzemer 2000]

This reduced slope indicates that beyond the constant amplitude fatigue limit, damage occurs at a different rate [Menzemer and Fisher 1993]. A number of references [Maddox 2003; Menzemer 2000] identify aluminum weld behaviour in the high cycle domain and under variable amplitude loading



conditions as areas where further study is required. Available fatigue data under variable amplitude spectrum loading is very limited and tests have been conducted to date for only one fatigue detail, a non-load carrying longitudinal attachment. Thus, the reduction in slope beyond the CAFL assumed in the specifications listed here is based on fracture mechanics analysis alone and not experimental data [Menzemer 2000].

Discrepancy between the different design codes is apparent with regards to definition of the constant amplitude fatigue limit. A majority of design specifications assume a CAFL at  $5 \times 10^6$  cycles but there are exceptions, such as the British Standard and the IIW recommendations, where a CAFL limit at  $10^7$  cycles is assumed. The ease of extrusion of aluminum alloys allows for many complex structural shapes and details, thus causing more difficulty in implementing the detail classification method. To address this issue, many modern codes and specifications are starting to include provisions for using the hot-spot or structural stress approach for fatigue design [CEN 2005]. This approach allows the critical local stress range to be determined by a coarse finite element analysis, thus facilitating the fatigue design of structural details that have not been previously tested.

## 2.5 Fatigue Load Correction Factors

The fatigue resistance curves specified in various standards are discussed herein. The approaches used by two highway bridge design codes CSA-S6 and AASHTO for determining the design fatigue loading are discussed, with a focus on the background behind the fatigue correction factors. The fatigue correction factor represents the difference between the fatigue damage caused by the code truck versus realistic traffic and facilitates the use of the code truck for fatigue design.

### 2.5.1.1 Canadian Highway Bridge Design Code

In CSA-S6, the fatigue design criteria for steel, takes the following form,

$$0.52 \cdot f_{sr} \leq F_{sr} \quad (2.6)$$

where  $f_{sr}$  is the stress range determined by passing the CL-625 truck over a bridge, and  $F_{sr}$  is the fatigue strength for a critical detail category and corresponding fatigue life [CSA 2006]. In reality, it is expected that the CL-625 truck may pass over a structure very few times, and a majority of the loading induced on the structure are in fact smaller trucks. Thus, the fatigue correction factor of 0.52, applied to the calculated stress range, is introduced. The establishment of this correction factor value essentially involved modifying the fatigue correction factor in AASHTO to account for the fact that

legal loads for Canadian traffic are higher and the CL-625 code truck is heavier than the AASHTO code truck [CSA 2006].

The CL-625 is an idealized five-axle truck used for design with a gross weight of 625 kN (Figure 2.24).

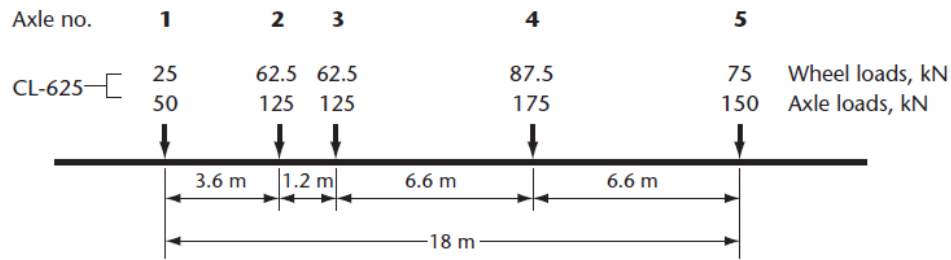


Figure 2.24: CSA CL-625 design code truck [CSA 2006]

For design of highway systems that include interprovincial transport the CL-625 truck must be used. A single CL-625 truck placed in the centre of one design lane is used for the fatigue limit state. In the fatigue design criteria, the fatigue stress range resistance,  $F_{sr}$ , for a given detail is determined by identifying the detail category for the critical section and calculating the fatigue life based on a design life of 75 years, the number of cycles for each CL-625 truck passage established by the member type and span, and the average daily truck traffic (ADTT) for the site. The calculated fatigue stress range,  $f_{sr}$ , determined by the passage of the CL-625 truck for the critical detail, in conjunction with the fatigue correction factor, 0.52, represents the load effect that must not exceed the resistance,  $F_{sr}$  [CSA 2006].

### 2.5.1.2 AASHTO LRFD Bridge Design Specification

Section 7 of the AASHTO LRFD Bridge Design Specification includes provisions for the design of aluminum highway structures. The design provisions in this section for load-induced fatigue state that each detail must satisfy the following criterion:

$$\gamma(\Delta f) \leq (\Delta F)_N \quad (2.7)$$

where  $\gamma$  is the load factor of 0.75 for fatigue,  $\Delta f$  is the stress range determined by the passage of the fatigue design truck over the bridge, and  $(\Delta F)_N$  is the nominal fatigue resistance of the corresponding detail category [AASHTO 2007]. A traffic survey [Snyder *et al.* 1985] of weigh-in-motion (WIM) data, from 30 sites across the United States, included axle weights and spacings for 27513 trucks was used to calibrate the fatigue load correction factor,  $\gamma$ , equal to 0.75. The calibration of this factor is

explained in Moses *et al.* [1987]. In this reference, a fatigue design truck representative of actual truck traffic is established by conducting an equivalent weight calculation using the following expression:

$$W = \left( \sum f_i \cdot W_i^3 \right)^{1/3} \quad (2.8)$$

where  $W$  is the effective gross weight of the fatigue design truck,  $W_i$  is the gross vehicle weight (GVW) associated with interval  $i$  in a GVW histogram generated with the real traffic survey data, and  $f_i$  is the of the total truck population associated with interval  $i$ . Equation (2.7) is based on Miner's sum for a single-slope design S-N curve with a slope of  $m = 3$ , which represents the current slope assumed for the design of steel structures. It is stated in AASHTO, that fatigue load correction factor is representative of realistic traffic loading with respect to the load effects on steel structures and components. It appears that a detailed calibration was not completed, considering design of aluminum structures. Using (2.7) along with the survey of American truck data provided by Snyder *et al.* [1985] a gross weight of the fatigue design truck of 54 kip (240.2 kN) is calculated [Moses *et al.* 1987]. The current fatigue design truck in AASHTO, which for reasons of convenience is the same truck used for static design, consists of the same axle spacing proposed by Moses *et al.* [1987] but has a gross weight of 72 kip (320.3 kN). Thus, by applying a correction factor of 0.75 to the fatigue design truck in AASHTO the design truck proposed by Moses *et al.* [1987] is attained (Figure 2.25).

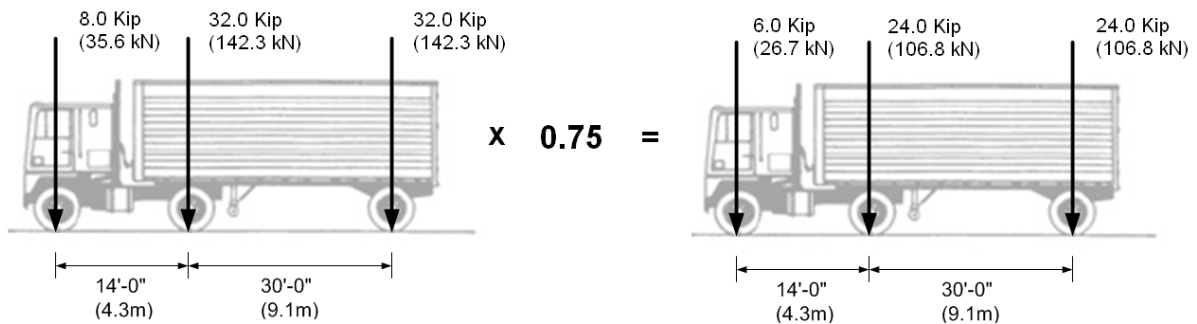


Figure 2.25: AASHTO fatigue design truck (left) and fatigue design truck proposed by Moses et al. [1987] (right)

## 2.6 Overload Traffic Events

When considering strength design of a bridge structure, it is important to encompass the maximum load effects into design. In fatigue design, the failure criterion is defined by cumulative damage, thus the design considers a wide spectrum of loading including both large and small trucks. Since a majority of real truck loads are smaller, and the maximum observed truck loads or overload events are

rare, small or average loads tend to have a larger impact on the fatigue life. Despite this fact, fracture mechanics analysis by Menzemer and Fisher [1993], lead to the conclusion that under realistic loading conditions, certain overload events may cause variations in the fatigue life.

Overloads come from a variety of sources and can be modelled in different ways; i.e. by considering overloaded trucks in excess of the legal load or due to the occurrence of multiple trucks passing over a bridge simultaneously. Herein, past analyses considering these two conditions are reviewed.

#### 2.6.1.1 Overloaded Trucks

Consideration of overload events represented by a truck in excess of legal load or a maximum observed load have been demonstrated by Menzemer and Fisher [1993]. In a fracture mechanics analysis, overload events were introduced into the load histories used. The assumed overload events consisted of a stress of 1.0 ksi (6.9 MPa) in excess of the maximum stress in the load spectrum occurring at a frequency ranging between 0% and 0.1% (see analysis results in Figure 2.27).

The fracture mechanics analysis confirmed that with an increase in the overload event frequency, or loading in excess of the CAFL, the fatigue life is decreased in the high cycle regime. This decrease in fatigue life is only apparent in the high cycle regime, and thus above the CAFL, overload events have little effect on fatigue resistance [Menzemer and Fisher 1993]. Further justification of the magnitude and frequency of the overload events used in this study is limited.

In CSA-S6, the CL-625 design code truck was established to model overload events for various axle groupings based on measured data, for the purpose of facilitating static strength design. Thus, the CL-625 truck itself is representative of the maximum observed loading conditions for various multiple axle configurations. This concept is explained graphically in Figure 2.26.

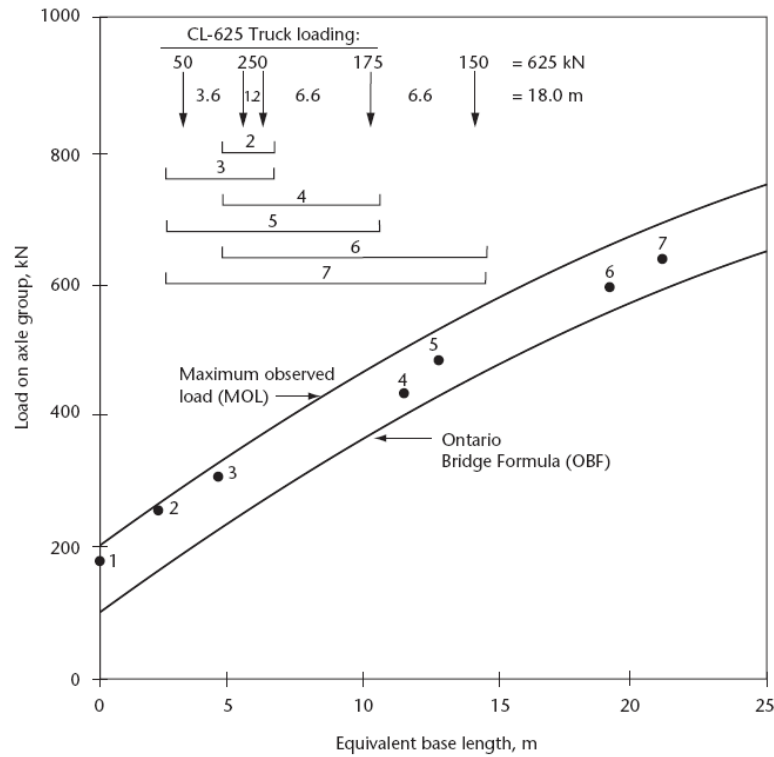


**Figure 2.26: Comparison of the CL-625 with maximum observed loading conditions [CSA 2006]**

Figure 2.26 compares the CL-625 design truck with curves based on observed data of the relationship between the axle group base length and weight for different numbers of axles ranging from two to five. Based on this comparison, it can be concluded that the CL-625 truck is representative of the maximum observed load for any axle group equivalent base length [CSA 2006].

### 2.6.1.2 Multiple Occurrence of Trucks

Overload events can also occur due to the passage of multiple trucks simultaneously across a bridge. In accordance with the calibration of AASHTO and CSA-S6, research by Nowak [1999] reviewed the impact of the passage of two trucks simultaneously side-by-side across a bridge structure. The live load model proposed by Nowak [1999] for the calibration of the design codes mentioned previously considers multiple presence loading of trucks in one and two lanes. The first case of multiple occurrence, considered the passage of two trucks in one lane, one after another, where the trucks are correlated by weight. Secondly, loading was considered in two lanes where two trucks, correlated by weight, pass over a bridge simultaneously side-by-side.

The database used to develop the live load model consisted of truck data from an Ontario survey completed by the Ministry of Transportation of Ontario (MTO) in 1975. The traffic survey completed by the MTO consisted of 9250 trucks including axle weights and spacings, but only trucks with higher loads were included in the study. American traffic data at the time of the study was noted as unreliable, thus the Canadian data was used for the study. Uncertainties in the analysis, regarding the data, included the small database size in relation to the truck traffic over the 75 year life of a bridge structure and the potential that overloaded trucks in excess of the legal load limit may purposely bypass truck weigh stations.

Overloads due to traffic in one lane consisted of two cases: a single truck overload, represented by the maximum occurrence over the 75 year design life of a bridge, and two trucks in the same lane passing one after another with varying headway distances and degrees of correlation by weight. Nowak [1999] defined headway distance as the distance from the rear axle of the first truck to the front axle of the second truck and varied this distance between 5 and 30 m in the analysis. Three levels of correlation, by truck weight, were considered in the Nowak live load model; no correlation, 50 percent or partial correlation, and full correlation. From the analysis it was found that, on average, every 50<sup>th</sup> truck is followed by another truck. Based on correlation of truck weight it was assumed that every 150<sup>th</sup> truck is partially correlated, every 500<sup>th</sup> truck is fully correlated, and all other cases are not correlated.

Overloads are also considered for traffic in two lanes whereby trucks pass over a bridge structure simultaneously side-by side. Two cases were investigated: one lane loaded and the other unloaded; and both lanes loaded considering three levels of truck axle weight correlation. Superposition of the two trucks was used to model the multiple presence of trucks. From the analysis it was found that, on average, every 15<sup>th</sup> truck simultaneously passed across a bridge side-by-side with another. Every 150<sup>th</sup> truck passage represents simultaneous passage of two trucks over a bridge with a 50 percent weight correlation or partial correlation. Every 450<sup>th</sup> truck passage represents simultaneous passage of two trucks over a bridge with full correlation. All other simultaneous passages of trucks over a bridge structure were said to have no correlation [Nowak 1999]. The Nowak live load model for multiple presence loading has been used by a number of other sources [Moses *et al.* 2001, Kulicki 2007, Sivakumar 2007].

## 2.7 Fracture Mechanics

Historically, fracture mechanics analysis has served as a useful tool for extending our understanding of the fatigue behaviour of aluminum welds beyond the conditions (i.e. loading conditions, detail geometries) covered by the limited available fatigue test data. Fracture mechanics theory assumes that a structure or component contains an initial crack or flaw, which is allowed to propagate through cyclic loading to failure. The fatigue resistance of a material is dependent on the rate at which a crack will grow. Menzemer [1992] indicates that the fatigue life of a component can actually be split into two parts; crack initiation ( $N_i$ ) and crack propagation ( $N_p$ ), as shown below,

$$N_{total} = N_i + N_p \quad (2.9)$$

The initiation stage of the fatigue life can be defined as the time required for a crack-like defect to initiate and grow to a length (or depth) of approximately 0.01 in (0.254 mm). A strain-life approach is normally used to predict  $N_i$  in smooth components. The crack propagation stage of the fatigue life can be defined as the time required for the crack to grow to a length that defines failure of the component. For predicting  $N_p$ , fracture mechanics is often used. In general, for smooth specimens, the crack propagation stage is relatively short; therefore, for components with long life most the fatigue life is spent in the crack initiation stage. This is not the case for welded components, as they contain crack-like defects due to the fabrication process [Menzemer 1992]. Thus, in contrast to smooth specimens, the crack propagation phase for welded components takes up a majority of the fatigue life. Although for welded components the crack initiation phase is relatively short, the arbitrary line between crack initiation and propagation is undefined.

In the next sections, two major sources using a fracture mechanics approach to predict the fatigue life of aluminum welds are described. A fracture mechanics analysis requires a number of input parameters; research to characterize some of these is described here including: cyclic material constants, residual stresses, initial crack size, and crack shape.

### 2.7.1 Concurrent to testing at the ATLSS Laboratory

Concurrent with the fatigue testing of aluminum weldments completed by Menzemer and Fisher [1993] at the ATLSS Laboratory at Lehigh University, a linear elastic fracture mechanics (LEFM) analysis was performed to predict fatigue behaviour beyond the limits of the available test data. The analysis was first conducted for constant amplitude loading and the results were verified with the test data. The verified model was further enhanced and then used to make predictions under variable

amplitude loading conditions. Crack growth was assumed in the model to occur according to Paris' law,

$$\frac{da}{dN} = C \cdot \Delta K^m \quad (2.10)$$

where  $da/dN$  is the crack growth rate,  $\Delta K$  is the stress-intensity range, and  $C$  and  $m$  are material constants. Using the fracture mechanics model, a series of design S-N curves are presented and compared to the experimental test data for beam stiffeners. The influences of the initial crack size and crack shape ratio are investigated through variation of the parameters in the model. The typical weld geometry of a stiffener is assumed to have a weld toe angle of  $45^\circ$  and a weld toe radius of  $3/16$  in (4.762 mm).

Three different loading histories were used in the study; constant amplitude and linear or Rayleigh variable amplitude distributions. The load histories used were scaled to generate the equivalent stress range desired. Under realistic loading conditions, certain overload events, or load cycles exceeding the constant amplitude fatigue limit, may cause variations in the fatigue life. Therefore, overload events were included the load histories as one of the considered parameters. The overloads used in the model consisted of a stress of 1.0 ksi (6.9 MPa) in excess of the maximum stress in the load spectrum occurring at a frequency ranging between 0% and 0.1% (Figure 2.27).

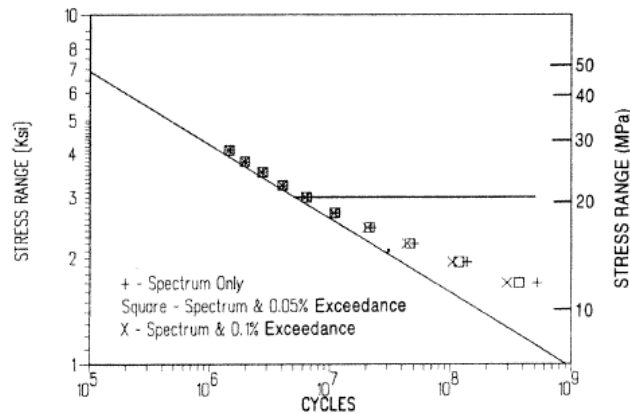


Figure 2.27: ATLSS LEFM analysis for overload events [Menzemer and Fisher 1993]

The fracture mechanics analysis confirmed that with an increase in the overload frequency, in the high cycle regime, the fatigue life decreases. Above the constant amplitude fatigue limit, overload events have little effect on fatigue resistance. The variable amplitude stress histories are categorized



using an equivalent constant amplitude stress range as determined using a transformation of Miner's sum, similar to equation (2.4) shown above, which represents the same amount of damage as the variable stress history.

In the fracture mechanics analysis, Menzemer [1992] assumed various crack shapes ranging from a crack shape ratio ( $a/c$ ) of 0.25 to 1.0. Note: in all cases, the initial crack was assumed to be a semi-elliptical surface crack with depth,  $a$ , and half-width,  $c$ . The initial defect depth,  $a_i$ , was also varied in the analysis from 0.0005 in (0.0127mm) to 0.002 in (0.0254mm). The basis for the chosen initial defect depth range was concluded from approximately 100 initial defect measurements.

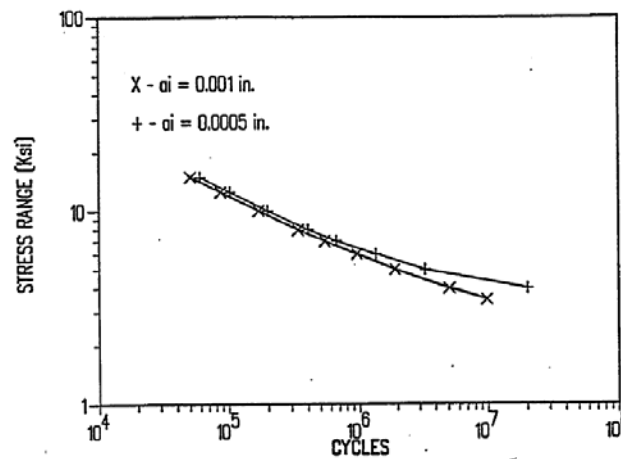


Figure 2.28: ATLSS LEFM analysis for beam stiffeners with varying initial crack sizes [Menzemer 1992]

Figure 2.28 shows that by varying the initial crack size in the fatigue life prediction a decrease in initial crack size will cause an increase in the fatigue life.

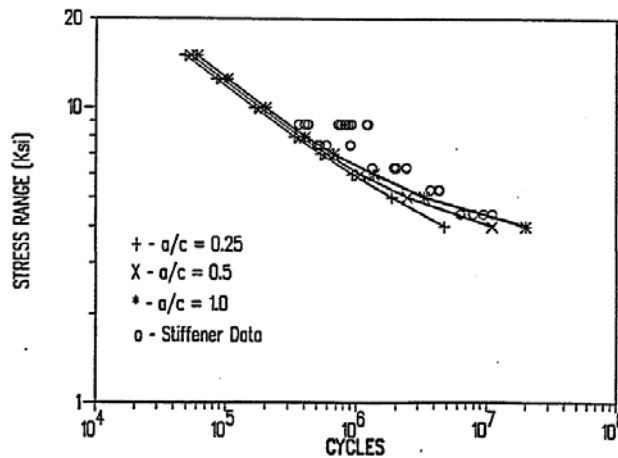


Figure 2.29: ATLSS LEFM analysis for beam stiffeners with varying crack shape ratios [Menzemer 1992]

The effect of the crack shape ratio was seen to have a more pronounced impact on the fatigue resistance in the high cycle regime. In general, the higher the crack shape ratio the longer the fatigue life. Figure 2.29 shows that using a crack shape ratio of 0.5 the predicted life curve represents a lower bound of the test data. In general, the fracture mechanics analysis provides a conservative estimate of the test data for the beam stiffeners. This could be due to one or several of the input parameter choices, or due to the presence of a significant crack initiation stage, which is causing an increase in the fatigue life of the test specimens. The data also confirms that a decrease in initial crack size causes an increase in the fatigue life [Menzemer 1992, Menzemer and Fisher 1993].

### 2.7.2 Concurrent to the EUREKA Research Project

The EUREKA research program also included a theoretical analysis for fatigue life prediction of aluminum weldments using a LEFM-based approach. Based on crack growth data determined for the 6061-T6 aluminum parent material, the heat affected zone, and the weld metal, crack growth calculations were conducted. The Paris relationship was again used to relate the crack growth rate and the stress intensity factor range. The goal of the fracture mechanics analysis was to provide a representative design S-N curve of the test data so that fatigue resistance can be determined for stress ranges not tested experimentally. Parameters describing specimen geometry and plate thickness were varied to match the test data. Verification of the model was completed by a comparison with the fracture mechanics analysis. By varying the initial crack depth between  $a_i = 0.05$  mm and  $a_i = 0.5$  mm the analytical results were shown to match the experimental test data [Soetens *et al.* 1995].

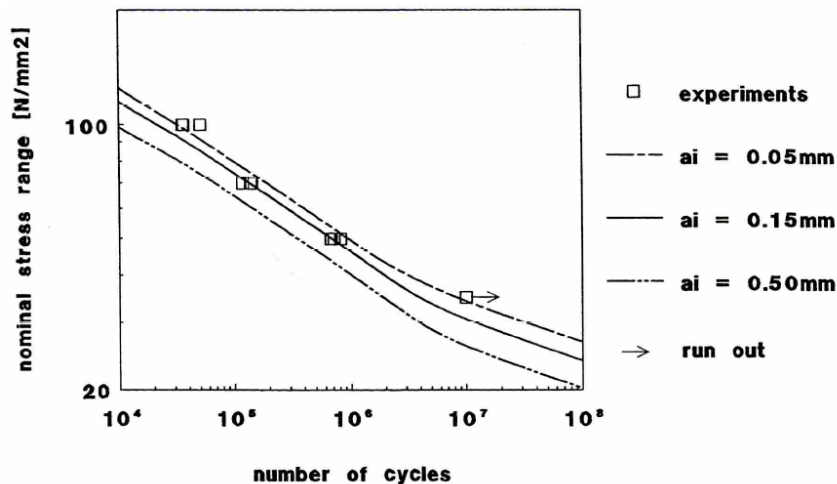


Figure 2.30: EUREKA LEFM analysis [Soetens *et al.* 1995]

On this basis, Soetens *et al.* [1995] concluded that the employed fracture mechanics model provides a valid representation of the fatigue life of the structural details tested and the use of crack growth models is an effective tool when analyzing aluminum structures for fatigue.

### 2.7.3 Initial Crack Size and Crack Shape

In a fracture mechanics analysis, the fatigue strength of a material or component is directly influenced by the assumed size of the initial crack or crack-like flaw. In general, it can be assumed that all welds are imperfect, and thus, contain flaws (i.e. [Smith & Smith 1982] for steel welds). Flaws can include porosity, inclusions, incomplete penetration, and incomplete fusion. It is from these flaws due to the welding process that cracks tend to propagate.

Documented use of initial crack sizes in fracture mechanics analysis is limited for aluminum. Menzemer [1992] observed initial flaw sizes ranging from 0.0005 in (0.0127 mm) to 0.006 in (0.0508 mm). Scanning Electron Microscopy (SEM) was used to examine the failure surfaces for size and orientation of initial flaws or defects (Figure 2.31).

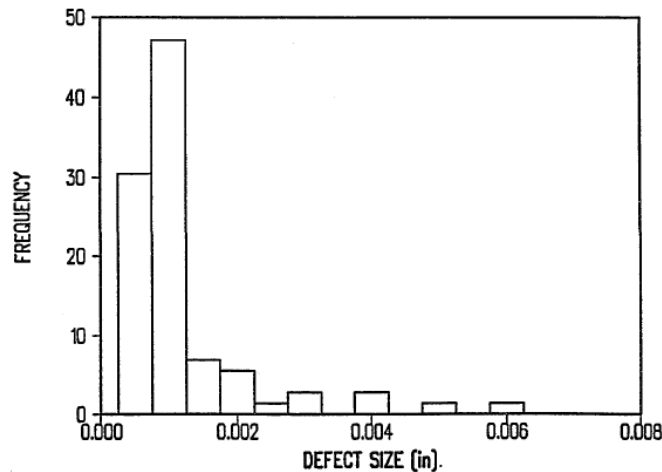


Figure 2.31: Defect histogram for initial flaws of welded aluminum components [Menzemer 1992]

Figure 2.31 provides a histogram summarizing results for approximately 100 measurements using SEM. It was concluded that the most frequent defect size was 0.001 in (0.0254 mm), and porosity was the most recurring defect type. Thus, in a fracture mechanics analysis conducted, three initial crack sizes were used, representing the highest defect frequencies measured; 0.0005 in (0.0127mm), 0.001 in (0.0254mm), and 0.002 in (0.0508 mm).

Along with an estimation of the initial crack size, an empirical crack shape expression was developed, for a stiffener detail, to provide a representation of the crack shape evolution, as the crack grows through the specimen thickness,

$$c = 3.274 \cdot a^{1.241} \quad (2.11)$$

This relationship was determined using a fracture mechanics analysis for maximum stress concentrations ranging from 4.0 to 5.0, and the three initial crack sizes noted above. The expression is noted to be a realistic representation of the crack shape as it accounts for the combination of multiple crack fronts as observed on test specimens [Menzemer 1992].

Burk and Lawrence [1978] stated the importance of the initial crack size assumption on the results of fracture mechanics-based fatigue life predictions. The initial flaw was defined in this reference as the crack size when the crack initiation portion of fatigue life is complete. Provided there are no cracks or crack-like flaws already present prior to the start of loading, an approximation of this crack length (or depth) for two-stage fatigue life models was made under the assumption that it must be greater than the threshold crack size,

$$a_{th} \geq \frac{1}{\pi} \left( \frac{\Delta K_{th}}{\Delta S} \right)^2 \quad (2.12)$$

where  $a_{th}$  is the threshold crack size,  $\Delta K_{th}$  is the threshold stress intensity factor, and  $\Delta S$  is the applied stress range. It was assumed that the crack initiation life of a welded component is the same as a smooth specimen, if both are the same material and undergo the same stress-strain history. By assuming an initial crack size, a fracture mechanics approach was used to predict the propagation fatigue life. Thus, a two-stage fatigue life model for 5083 butt welded aluminum alloys was employed. Crack propagation life calculations, for welded components, were conducted in this study based on the assumption of an initial crack length of 0.01 in (0.25 mm), which is found to be the crack size at the end of the crack initiation phase.

Burk and Lawrence [1978] also noted another approach, where the crack initiation phase was assumed to be very short or nonexistent, and the total fatigue life can be represented by the propagation life due to small defects present at the weld toe, from the welding process. For welded components, the initial crack size was taken as the length of defects due to the welding process. It was stated that when failure originates at the weld toe or due to porosity, the initial crack size is unclear. A proper estimate of the initial crack size is critical as it has a large impact on the fatigue life.

The EUREKA research project, similarly to the research conducted by Menzemer [1992], compared different initial crack sizes used in a fracture mechanics analysis to the fatigue test data. Three initial crack sizes were used to represent the experimental data; 0.05 mm, 0.15 mm, and 0.5 mm. Based on the experimental data and fatigue life predictions in Figure 2.30, an initial crack size of 0.05 mm in the fracture mechanics analysis was found to best represent the fatigue test data.

A study undertaken by Kosteas and Bompard [1995] included an analysis of fracture surfaces to properly quantify imperfections and fatigue crack initiation sites to further enhance life prediction models using fracture mechanics. The fracture surface from a test specimen for a welded beam stiffener using 7020 aluminum alloy was examined microscopically to determine dimensions of the crack. Approximate dimensions determined from the fracture surface are 0.1 mm in depth and 1.0 mm in width, which were used to represent a semi-elliptical crack surface in a fracture mechanics analysis. An empirical relationship of the crack shape for several structural details developed by Fisher *et al.* [1989] was used in this analysis. For a web stiffener, the relation between  $a$  and  $c$  can be determined from the following expression,

$$c = 1.403 \cdot a^{0.951} \quad (2.13)$$

Based on measurements of initial crack defects, crack growth calculations were first conducted using assumed initial crack sizes of 0.05 mm and 0.1 mm. Using these assumed initial crack sizes, very good correlation between experimental and analytical results was found. The influence of the initial crack size was further investigated as there is still uncertainty regarding the initial crack measurements. Figure 2.32 shows the relationship between the initial crack size and the total fatigue life.

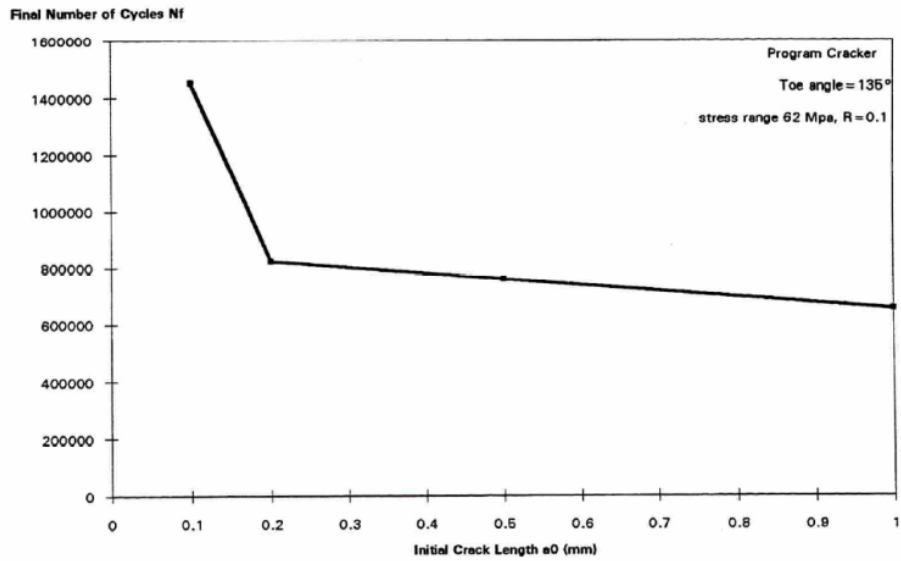


Figure 2.32: Influence of initial crack length on fatigue life [Kosteas and Bompard 1995]

Based on this investigation, it was found that as the initial crack length increases, the fatigue life decreases. It is also apparent looking at Figure 2.18 that for an initial crack length between 0.1 mm and 0.2 mm, the change in the predicted fatigue life is significant. For initial crack lengths greater than 0.2 mm the change in the predicted fatigue life is marginal.

### 2.7.4 Residual Stresses in Welded Aluminum Components

Due to the significant heating and cooling associated with the welding process, tensile residual stresses are present in welded aluminum components, causing a significant reduction in fatigue resistance due to their effect on the mean stress at the joint. Through testing, Menzemer and Fisher [1993] note that residual stresses have a significant impact on the fatigue strength of aluminum; therefore, realistic residual stress estimations must be including in a fracture mechanics analysis. In this reference, residual stress measurements were conducted prior to and after testing to confirm that these stresses did not vary as a result of the imposed cyclic loads. A significant difference was observed in the residual stresses present in the full- and small-scale specimens. The beam stiffener and cover plate details in the full-scale specimens were seen to contain residual stresses equal to 80% of the parent metal yield strength. Conversely, the small-scale specimens contained residual stresses equal to 40% to 50% of the parent metal yield strength. This difference is due to differences in the constraints present in the details during welding. Therefore, the conclusion is drawn that small-scale specimens are not representative of real structures, as they do not contain high residual stresses.

Kosteas [1988] conducted residual stress measurements on large-scale 7020 and 5083 aluminum alloy beams with varied weld details, and concluded that there was no difference in these stresses for the different alloys. Aluminum weldments are assumed in this reference to contain three areas in the weld region with differing mechanic properties; the weld metal, the heat-affected zone, and the parent metal. In 7020 aluminum, the yield strengths of the parent material and heat affected zone are 300 and 185 MPa, respectively. From testing, residual stresses for certain details in large-scale test beams were typically found to have a magnitude as high as 75% of the yield strength in the HAZ (or 46% of the parent material yield strength). Residual stresses were the highest in longitudinal and transverse fillet welded beam stiffener details, reaching 180 MPa. All residual stress measurements were taken prior to testing, and thus, it is not certain whether the initial residual stresses were maintained over the life of the component.

Burk and Lawrence [1978] conducted a study investigating the effect of residual stresses on welds and found that much of the scatter in the existing fatigue test data for welds can be attributed to the presence of residual stresses. In this study, tests of 5083-O aluminum alloy butt welds were conducted. Residual stress measurements were taken using an x-ray diffraction technique for one weld. Based on these measurements of one weld, all welds were assumed to contain tensile residual stresses of 125 MPa, representing 95% of the base metal yield strength and 90% of the weld metal yield strength. Predictions made in this study, assuming a two-stage fatigue life model, suggest that the fatigue life is only affected by residual stress for fatigue lives greater than  $10^6$  cycles, and that tensile residual stresses have no effect on the shorter fatigue lives. Predictions that considered residual stresses were found to compare well to the fatigue test results for both aluminum and steel alloy specimens. Material strength was seen to influence the effect that residual stresses have on fatigue life. Specifically, the high strength steels were seen to be influenced more by residual stresses in comparison with the lower strength aluminum alloys.

### **2.7.5 Cyclic Material Constants**

In order to perform strain-life analyses required to predict the crack initiation life,  $N_i$ , according to models such as the one used by Burk and Lawrence [1978], the cyclic stress-strain behaviour of the material must be known. This behaviour may also be required to implement more advanced fracture mechanics models when significant nonlinear material behaviour is expected or assumed.

Burk and Lawrence [1978] conducted tests to determine the cyclic Ramberg-Osgood material constants,  $K'$  and  $n'$ , for aluminum alloys. The test specimens were smooth, with an hourglass shape.

Tests of 5083-O base metal and 5183 weld metal were conducted under strain control at cyclic strain amplitudes between approximately 1.0% and 0.1% strain.

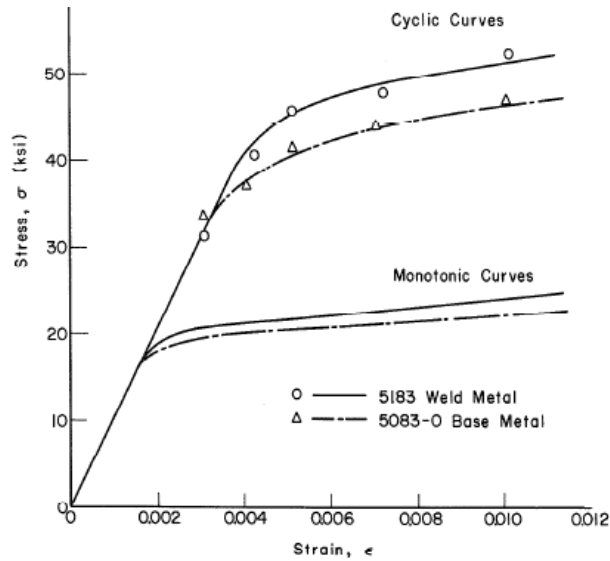


**Figure 2.33: Aluminum cyclic testing data [Burk and Lawrence 1978]**

The cyclic stress-strain properties shown in Table 2.2 were generated from the testing results above. The behaviour of both the base and weld metal is very similar. The yield strength of the weld metal is slightly higher. Although the weld metal has a higher ultimate strength than the base metal, the hardness of both aluminum alloys was seen to be the same [Burk and Lawrence 1978].

**Table 2.2: Aluminum cyclic properties [Burk and Lawrence 1978]**

<b>Material</b>	<b>5083-O</b>	<b>5183</b>
Hardness (DPH/BHN)	106/93	105/92
Modulus of Elasticity (GPa)	71	71
Yield Strength (MPa)	131	138
Ultimate Tensile Strength (MPa)	294	299
Cyclic Yield Strength (MPa)	269	290
Cyclic Strain Hardening Exponent	0.072	0.114
Cyclic Strength Coefficient (MPa)	507	580

The Ramberg-Osgood material model accounts for plastic deformation that occurs beyond yielding of the material and provides a true stress versus true strain relationship,



$$\varepsilon = \varepsilon_e + \varepsilon_p = \frac{\sigma}{E} + \left( \frac{\sigma}{K'} \right)^{1/n'} \quad (2.14)$$

which is represented by both the elastic strain ( $\varepsilon_e$ ) and the plastic strain ( $\varepsilon_p$ ). In relation to stress, the plastic strain is determined using the strength coefficient,  $K'$ , and strain hardening exponent,  $n'$ , for a given material [Stephens *et al.* 2001].

## 2.8 Summary

The key findings in this review of the literature are as follows:

- The material properties of aluminum, including its high corrosion resistance and light weight, are advantageous when considering aluminum as a design material for bridge structures.
- Design examples from the past demonstrate that use of aluminum in bridge structures has been successful and is an economical design option in certain cases.
- Much research and testing has been conducted regarding fatigue of aluminum, but testing is still limited under variable amplitude loading, particularly in the high cycle range. Review of current design codes and specifications for aluminum demonstrates the difference in the S-N curves in the high-cycle range, which highlights the need for more testing and research in this area.
- Use of a fatigue correction factor for aluminum in the North American design codes is based on values derived for steel, which were simply adopted for aluminum.
- The Nowak live load model provides the most up-to-date approach to model simultaneous passage of trucks when considering overload traffic events.
- Fracture mechanics analyses conducted in the past are successful at predicting the fatigue life under variable amplitude loading conditions in the high-cycle range, although large variability in the results remain from study to study. The variability in results is due in part to the input parameters used in the analysis. Many of these parameters used are documented for use in this study.

The literature indicates that use of aluminum in bridge structures is an advantageous design option but is still not widely used due to limitations in research and development. The key findings presented support the objectives outlined in Chapter 1:

- A study to determine the fatigue correction factors for aluminum is required to determine whether the values currently used for steel are adequate.
- Fatigue testing in this study under variable amplitude loading in the high cycle range will provide test data in an area where limited data exists. Testing along with fracture mechanics analysis using the parameters reviewed in the literature will assist in review of discrepancies apparent in current fatigue design codes and specifications for aluminum.

## Chapter 3

### Fatigue Load Correction Factors

Fatigue correction factors are often used in bridge design specifications for verification of the fatigue limit state to relate the fatigue damage due to the code truck model with that due to the real truck traffic. Fatigue stress ranges are determined for critical structural details in design by simulating the passage of a design code truck over the structure or component. The design code truck is an idealized representation of the real traffic, which is normally established to model extreme live load events for static design and not the cumulative damage due to the entire real traffic histogram. Thus, through calibration, a fatigue correction factor can be determined through simulation of the real traffic and comparison of the fatigue damage due to the real traffic and the design code truck. This correction factor can then be applied to the design stress determined using the design code truck to calculate a fatigue stress range that more closely represents the effect of real traffic loading.

In this chapter, a calibration method is described for establishing fatigue correction factors for the design of aluminum details. Following this, the implementation of this procedure is discussed and fatigue correction factors are presented for both the CSA-S6 and AASHTO Bridge Codes. In addition, a related investigation examining the effects of overload events on the calculated fatigue correction factor is presented.

#### 3.1 Calibration Procedure

The following information is required to calibrate the fatigue correction factor using the proposed methodology:

- a code truck model,
- real traffic data for the region of interest,
- influence lines for various critical locations in bridges, and
- a design service life and expected traffic volume.

Design code trucks from both CSA-S6 and AASHTO are used for each respective calibration. The most readily available real traffic data is used from Canadian and American surveys. Figure 3.1 shows the seven influence lines used in this calibration, which cover the following cases:

- positive moment at the mid-span for 1-, 2-, and 5-span beams ( $p_{s-m}$ ,  $p_{2tr-m}$ , and  $p_{5tr-m}$ ),

- negative moment at the intermediate support for 2- and 5-span beams ( $p2tr-a$  and  $p5tr-a$ ), and
- shear at the support for 1- and 2-span beams ( $ps-r$  and  $p2tr-r$ ).

16 bridge spans are considered ranging from  $L = 2$  to 60 m.

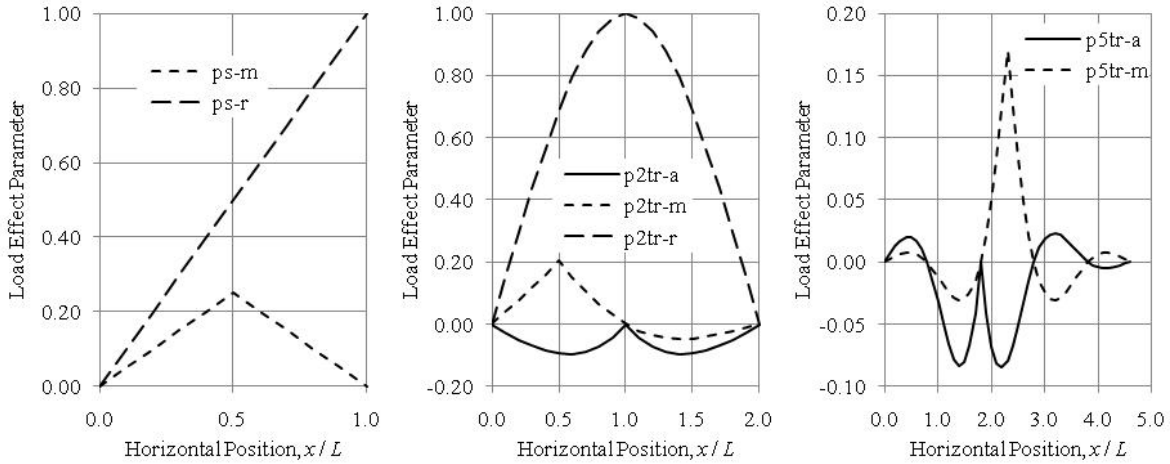


**Figure 3.1: Influence lines used in calibration for one (left), two (centre), and five (right) spans.**

A program written in FORTRAN 95 is employed for each span/influence line combination to determine the fatigue load correction factor. For each case, a database of measured trucks are passed over the influence line in succession (one truck on the bridge at a time, in 0.2 m steps). The load effect is determined for each vehicle position, based on the axle loads and the influence line. Whenever a peak value is observed, it is recorded in a list or load effect history. Figure 3.2 shows a portion of such a history for the mid-span moment in a simply supported bridge (influence line:  $ps-m$ ) with a 30 m span. Once the load effect history for all of the trucks has been generated, the rainflow method is used to count cycles [Downing and Socie 1982]. These cycles are then collected into a histogram (Figure 3.2).

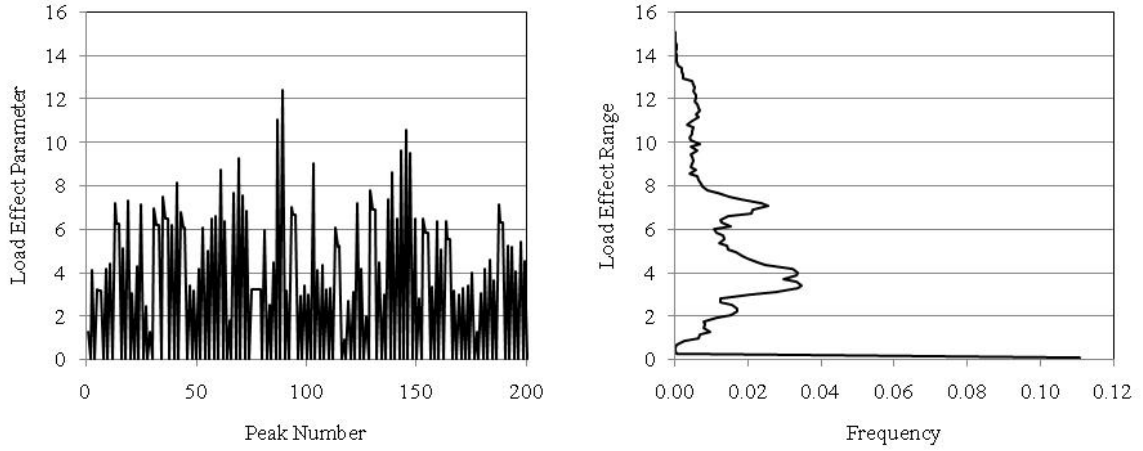


**Figure 3.2: Sample of load effect history (left) and histogram (right) for  $ps-m, L = 30$  m case**

Next, the code truck is passed over the bridge and the maximum load effect range recorded. Following this, the S-N curve shape of interest is compared to the histogram, scaled to the expected total truck traffic volume, where:

$$Total\ truck\ traffic\ volume = Service\ life \cdot ADTT \cdot 365\ days \quad (3.1)$$

Specifically, the S-N curve is assigned an arbitrary vertical position, and then the fatigue damage ratio,  $D_{real}$ , is calculated using Miner's sum. An algorithm is then implemented wherein the S-N curve is shifted vertically until a damage ratio of  $D_{real} = 1.0$  is achieved. The resulting value of the fatigue life constant,  $\gamma$ , is termed  $\gamma_{real}$ . Note that  $\gamma$  is a measure of the vertical position of the S-N curve; specifically:

$$LOG_{10}(N) = LOG_{10}(\gamma) - m \cdot LOG_{10}(\Delta S) \quad (3.2)$$

Next, the S-N curve is again shifted vertically to the value of  $\gamma$  that results in a damage ratio of 1.0 under constant amplitude loading at the load effect range due to the code truck, for a number of cycles,  $N_c$ , equal to the total truck traffic volume multiplied by the number of design stress cycles experienced by the passage of the code truck,  $N_d$ . The resulting value of  $\gamma$  is termed  $\gamma_{code}$ . It can be shown that the fatigue correction factor,

$$\lambda = \left( \frac{\gamma_{real}}{\gamma_{code}} \right)^{1/m} \quad (3.3)$$

By calculating the fatigue correction factor in this way, a result can be obtained without knowing the actual nominal stress influence line (which depends on the bridge cross-section). It is only necessary that the same influence line be used for the real traffic data and the code truck. If a single-slope curve is used, then the result is also independent of the total truck traffic volume. If a two-slope curve is used, however, then different fatigue correction factors will be found depending on the truck traffic volume. The fatigue correction factor calibration procedure is explained conceptually in Figure 3.3 for the  $ps-m$  influence line case with a span of 30 m and  $ADTT = 1000$ .

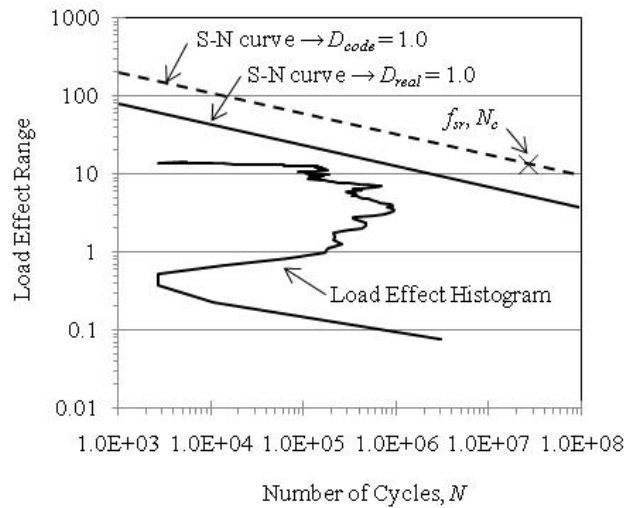


**Figure 3.3: Conceptual explanation of calibration procedure**

In this figure, the solid straight line represents the design S-N curve at the vertical position associated with  $\gamma_{real}$ , the dashed line indicates the position associated with  $\gamma_{code}$ . The calibration procedure is conducted for each aluminum fatigue detail in CSA-S6 and AASHTO.

### 3.2 CSA-S6 Load Correction Factors

Walbridge [2008] demonstrated the calibration procedure, described in the previous section, results in a calculated load correction factor very close to 0.52 (on average) for the single-slope steel design S-N curves in CSA-S6. Herein, a calibration of load correction factors for the design of aluminum structures is presented. At this time, design S-N curves for aluminum are not contained in CSA-S6. Thus, the design curves from AASHTO are first assumed and used for calibration of the fatigue correction factor. The most recent design curves for aluminum published by the Canadian Standards Association in CSA-S157 use two-slope design S-N curves (see Figure 2.15). A calibration of the

CAN-S6 fatigue correction factor based on these curves will also be conducted to demonstrate an application of the proposed methodology involving multi-slope design S-N curves.

### 3.2.1 Calibration Data

The code truck model employed for the CSA-S6 calibration was the CL-625 truck (see Figure 2.24). Axle weight and spacing data for 10198 trucks measured in Ontario in 1995 by the MTO, provided in [MTO 1995], was used to represent the real traffic. This data, along with data from other provinces, was used to calibrate the current code [CSA 2007]. The data from the Ontario survey is summarized in the form of a gross vehicle weight (GVW) histogram in Figure 3.4.

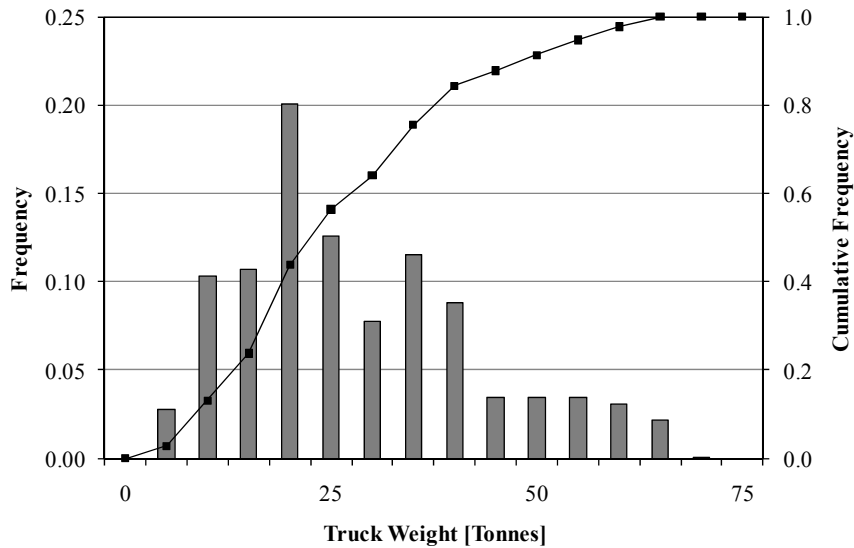


Figure 3.4: GVW histogram for the Ontario traffic survey

CSA-S6 assumes a design service life of 75 years. Table 10.6 in CSA-S6 gives average daily truck traffic (ADTT) values from 50 to 4000 trucks/day for various roadway types (Table 3.1).

Table 3.1: Average annual daily truck traffic [CSA 2006]

Class of Highway	ADTT
A	4000
B	1000
C	250
D	50

The S-N curve shapes (slopes and slope transition points) are needed for the calibration. In CSA-S6, the steel design S-N curve currently has a single slope with  $m = 3.0$ . The single-slope design curves from AASHTO have slopes,  $m$ , ranging from 3.42 to 6.85 (see Figure 2.16 and Table 3.2). CSA-S157 uses two-slope curves, each with a different initial slope,  $m$ , ranging from 3.08 to 8.38 (see Figure 2.15 and Table 3.2). After  $5 \times 10^6$  cycles, the second slope,  $m' = 10.41$  in most cases.

**Table 3.2: Design detail categories for AASHTO, CSA-S6, and CSA-S157**

Detail Category	AASHTO/CSA-S6	CSA-S157	
	$m$	$m$	$m'$
A	6.85	8.38	10.41
B*	-	7.94	10.41
B	4.84	5.84	9.95
C	3.64	5.16	10.41
D	3.73	4.21	10.41
E	3.45	3.72	10.41
F	3.42	3.08	8.40

### 3.2.2 Calibration Results

Typical results of the calibration process in the case of a single-slope design S-N curve for CSA-S6 using AASHTO Detail Category A ( $m = 6.85$ ) are shown in Figure 3.5. The correction factor,  $\lambda_{CSA-S6}$ , varies for the different influence lines and bridge spans. Between 2 and 12 m,  $\lambda_{CSA-S6}$  fluctuates significantly. There is a jump above 12 m, since the factor  $N_d$  changes above this span. From 15 to 60 m,  $N_d = 1.0$  and  $\lambda_{CSA-S6}$  is fairly constant. Similar observations can be made for the correction factor,  $\lambda_{CSA-S6}$  based on the CSA-S157 design S-N curves.



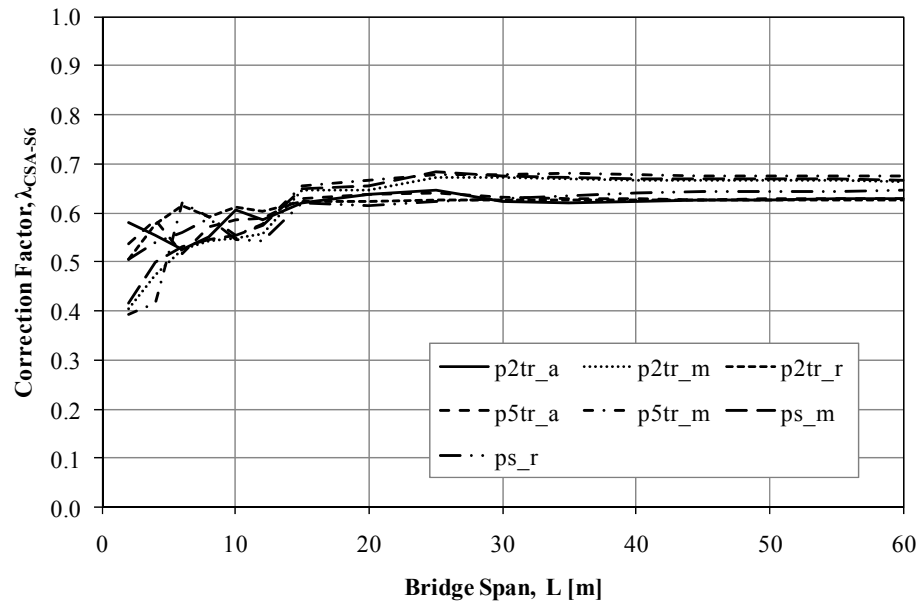


**Figure 3.5: CSA-S6 correction factor results for CSA-S6 Detail Category A ( $m = 6.85$ )**

In Figure 3.6 and Figure 3.7, correction factor values,  $\lambda_{CSA-S6}$ , are presented for all detail categories in both AASHTO and CSA-S157, respectively. These correction factors are reported as average values, denoted in all figures using a black curve, and maximum values, denoted in all figures using a grey curve, obtained for the seven influence lines, between the spans of 15 and 60 m. The seven influence lines considered in this calibration are thought to be representative, and therefore, provide a reasonable estimate for most influence lines likely to be seen in practice. It should be noted however, that the influence lines considered were not necessarily chosen to reflect the most likely locations of for fatigue cracking in highway bridges, but rather to cover a broad range of likely load history characteristics that can be expected in bridge structures.

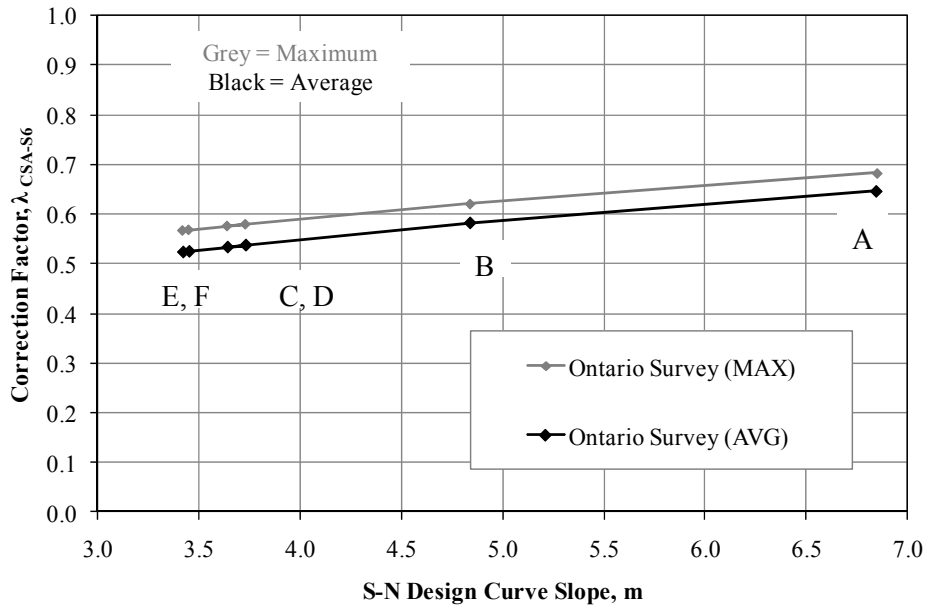


Figure 3.6: CSA-S6 calibration results using AASHTO design S-N curves

In Figure 3.6, it can be seen that  $\lambda_{CSA-S6}$  is greater than 0.52 (the value for  $m = 3.0$  in steel design) in all cases. In general,  $\lambda_{CSA-S6}$  increases with  $m$ . Table 3.3 provides a summary of the fatigue correction factor,  $\lambda_{CSA-S6}$ , for each detail category including  $m = 3.0$ .

Table 3.3: CSA-S6 fatigue correction factor results corresponding to AASHTO detail categories

Detail Category	$m$	$\lambda_{CSA-S6}$	
		Average	Maximum
A	6.85	0.65	0.68
B	4.84	0.58	0.62
C	3.64	0.53	0.58
D	3.73	0.54	0.58
E	3.45	0.53	0.57
F	3.42	0.52	0.57
-	3.0	0.50	0.55

One significant benefit of the described calibration method is that it can also be used to calibrate correction factors for multi-slope S-N curves. In Figure 3.7, correction factor values,  $\lambda_{CSA-S6}$ , are presented corresponding to the design S-N curves for CSA-S157.

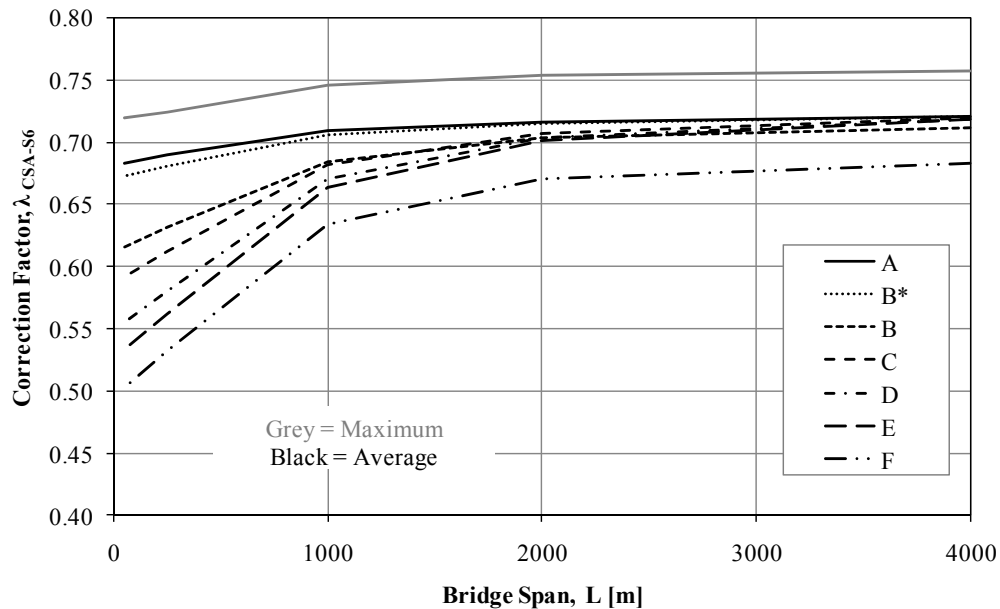


Figure 3.7: CSA-S6 calibration results using CSA-S157 design S-N curves

In Figure 3.7, it can be seen that  $\lambda_{CSA-S6}$  increases as the truck traffic volume (ADTT) increases. In general, the  $\lambda_{CSA-S6}$  versus ADTT curves converge at higher ADTT levels on the  $\lambda_{CSA-S6}$  value associated with the shallower  $m'$  slope.

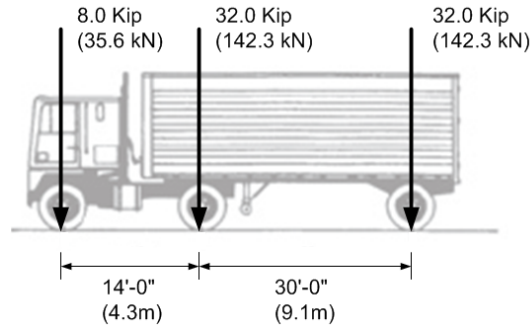
### 3.3 AASHTO Load Correction Factors

Currently in the AASHTO Specification, the fatigue load correction factor for both steel and aluminum is 0.75. The original calibration of this factor was completed using the steel design S-N curves (see Section 2.4.2), and subsequently it appears that the specification adopted the same correction factor for aluminum. In this section, the calibration procedure outlined in Section 3.1, is first verified using the AASHTO fatigue design truck and the existing steel design S-N curves. Further simulations are then conducted to determine the fatigue correction load factors for the current AASHTO aluminum design S-N curves.

#### 3.3.1 Calibration Requirements

The code truck model employed for this calibration was the AASHTO fatigue design truck, HS20-44 (Figure 3.8). Similar sets of data to the Ontario survey have been compiled in the United States using weigh-in-motion (WIM) systems. An explicit WIM database, including axle weights and spacing for all measured trucks has not been published, however. Thus, for this calibration, a real traffic database

had to be constructed given GVW histograms and typical axle spacing and weight distributions for different truck types.







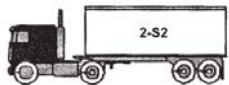
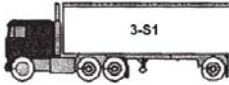
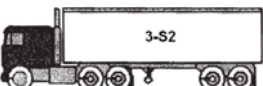
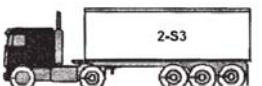
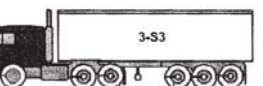


**Figure 3.8: AASHTO fatigue design code truck (HS20-44) [AASHTO 2007]**

In general, the establishment of a representative real traffic sample for the United States in its entirety is not a straight forward task, since truck weight limits and traffic compositions tend to vary from one region to the next. For the purposes of the current study, however, the survey results compiled by Moses *et al.* [1987] were used. These results were thought to be adequate, as they were compiled from studies conducted in several different states. In Moses *et al.* [1987], idealized axle weights and spacings for six truck categories are formulated (Table 3.4), including 11 different truck types (Table 3.5). These truck categories and types served as the basis for the formulation of a representative real traffic sample.

**Table 3.4: United States truck category axle weights and spacings [Moses *et al.* 1987]**

Truck Category	Truck Type	Axle Load (%)				Axle Spacing (ft [m])		
		1	2	3	4	1	2	3
Two axle singles	SU2	40	60	-	-	16 [4.88]	-	-
Three axle singles	SU3	30	70	-	-	18 [5.49]	-	-
	SU4							
Two axle semi-trailers	2-S1	27	40	33	-	12 [3.66]	32 [9.76]	-
Three axle semi-trailers	2-S2	23	35	42	-	12 [3.66]	28 [8.54]	-
	3-S1							
Four axle semi-trailers	3-S2	18	45	37	-	14 [4.27]	32 [9.76]	-
	2-S3							
Five axle semi-trailers	3-S3	17	29	42	12	10 [3.05]	25 [7.62]	25 [7.62]
	2-S1-2							
	3-S1-2							

**Table 3.5: United States truck categories and types [Moses *et al.* 1987, Harwood *et al.* 2003]**

Truck Category	Truck Type
Two axle singles	SU2 
Three axle singles	SU3 
	SU4 
Two axle semi-trailers	2-S1 
Three axle semi-trailers	2-S2 
	3-S1 
Four axle semi-trailers	3-S2 
	2-S3 
	3-S3 
Five axle semi-trailers	2-S1-2 
	3-S1-2 

A nationwide truck survey was conducted in the 1980s encompassing truck data from many states across the United States [Snyder *et al.* 1985]. WIM data was recorded for 27513 trucks from 30 sites in California, Georgia, Arkansas, Texas, Illinois, New York, and Ohio. An overall GVW histogram based on this WIM data is shown in Figure 3.9.

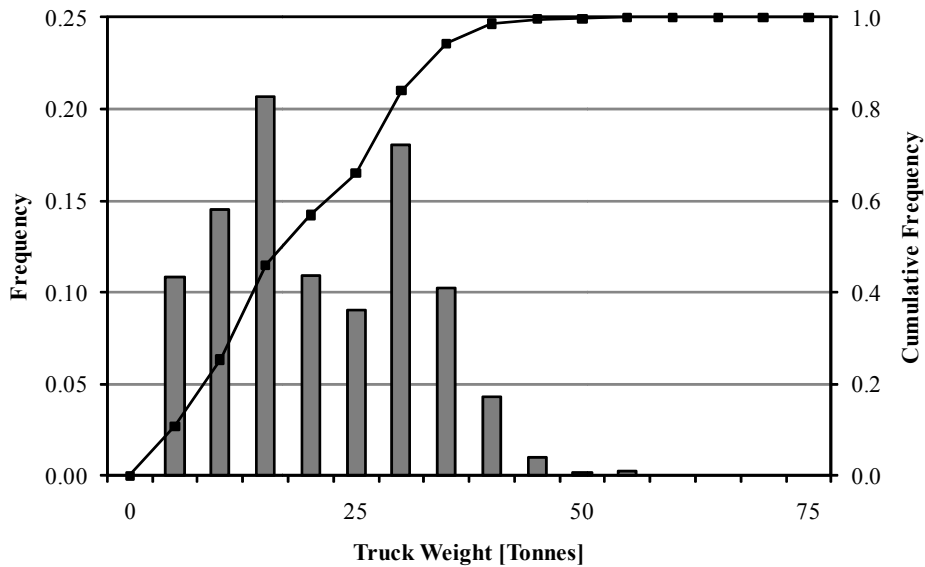


Figure 3.9: GVW histogram for an American survey of 27513 trucks [Snyder *et al.* 1985]

Of the 27513 trucks from this survey, 25901 trucks fall within the six truck categories outlined by Moses *et al.* [1987]. By reducing the traffic database by 1612 trucks, a comparison of GVW histograms is conducted to ensure the excluded data does not include extreme loads events that should not be excluded (Figure 3.10).

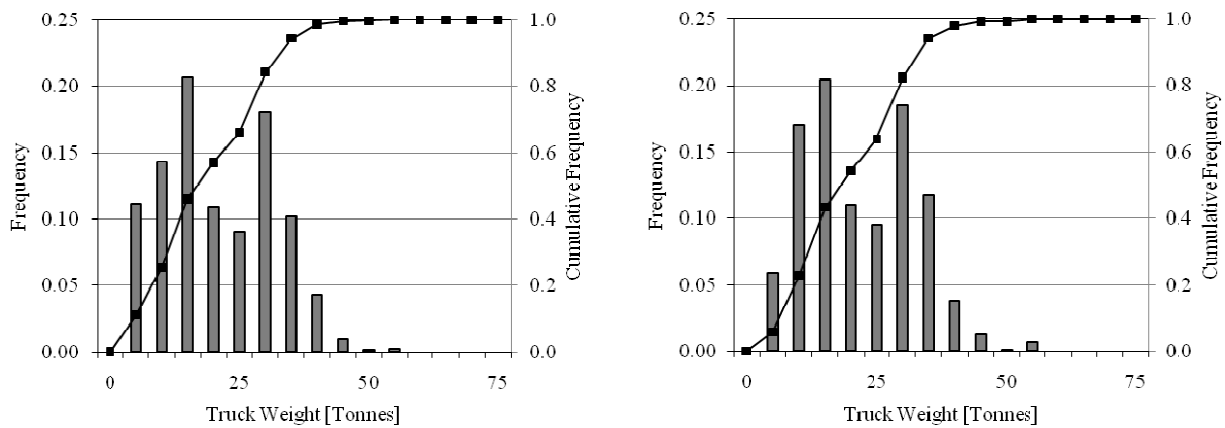


Figure 3.10: GVW histograms for American truck data included (left) and excluded (right) in this study

Both sets of data in Figure 3.10, 25901 trucks and 1612 trucks, respectively, follow the same distribution as the global database of 27513 trucks in Figure 3.9. Since the data for the 1612 excluded trucks does not include any extreme load event and follows the same distribution as the original database, use of the 25901 truck database is valid. Thus, the GVW data for 25901 trucks, from the survey conducted by Snyder *et al.*[1985], are used in conjunction with the axle weights and spacing for the six truck categories proposed by Moses *et al.* [1987] to develop a database of simulated real traffic.

The original survey by [Snyder *et al.* 1985] provided detailed GVW histograms for all 11 truck types considered in this study. Given these histograms, each of the 11 truck types was assigned idealized axle weights, defined as a percentage of the GVW per axle, in accordance with the six truck categories formulated by Moses *et al.* [1987]. Based on the GVW histogram for a given truck type along with the allocation of total vehicle weight to each axle for that type, a simulated database of real traffic was generated for all 11 truck types. This data for all the truck types or truck categories was combined to generate a database of truck traffic representative of the entire truck fleet for use in analysis.

### **3.3.2 Calibration Results**

Typical results of the calibration process described above for the case of a single-slope design S-N curve with a slope of  $m = 3.0$  (ie. the S-N curve for steel) are shown in Figure 3.11, which is typical of the current steel design S-N curves in CSA-S6 and AASHTO. The AASHTO fatigue code truck and simulated American traffic models were used in this calibration.

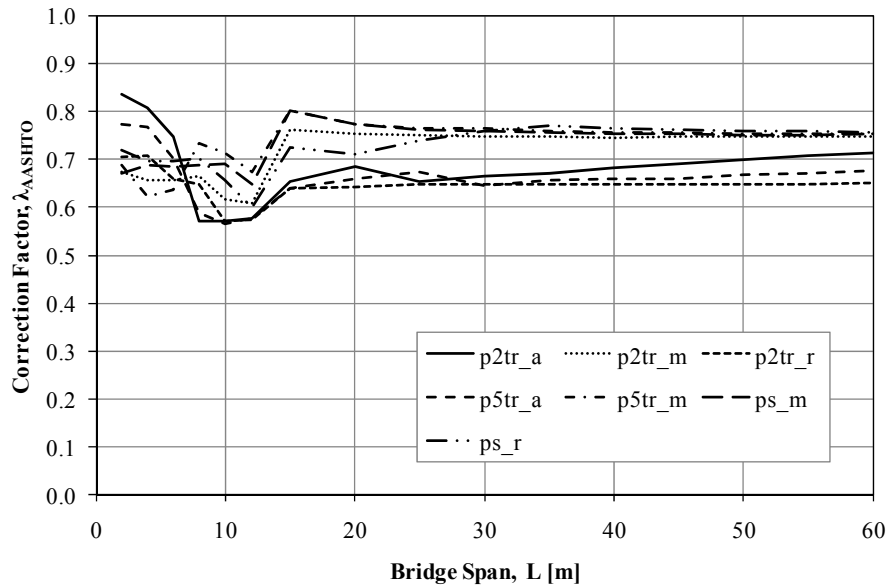


**Figure 3.11: AASHTO correction factor results for single slope S-N curve with  $m = 3$ .**

As seen in this figure, the correction factor,  $\lambda_{AASHTO}$ , varies for the different influence lines and bridge spans. Between bridge spans of 2 and 12 m,  $\lambda_{AASHTO}$  fluctuates significantly. There is a jump above 12 m, since the factor  $n$  (or  $N_d$ ) changes above span of 40 ft (12 m). From 15 to 60 m,  $\lambda_{AASHTO}$  is fairly constant. Using the simulated American traffic, Figure 3.11 shows that four of the seven influence lines converge on a correction factor of 0.75 as the span increases to 60 m. This is the value currently specified in AASHTO for this factor, which confirms that the simulated American traffic is suitable for performing similar calibrations for the aluminum design S-N curves.

In Figure 3.12,  $\lambda_{AASHTO}$  values are presented for each of the AASHTO detail categories. Again, in this figure, the black curve is based on average values obtained for the seven influence lines, between the spans of 15 and 60 m. The grey curve denotes the upper bound for the same influence line and span range.



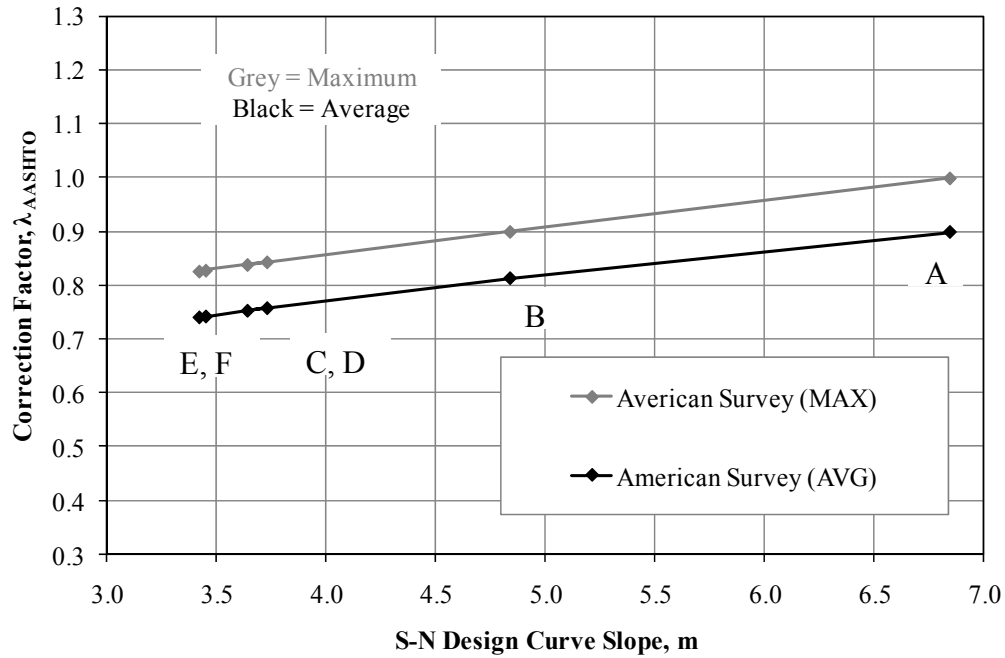


Figure 3.12: Calibration results for AASHTO aluminum design S-N curves

Looking at this figure, it can be seen that  $\lambda_{AASHTO}$  can be significantly greater than 0.75 (the value for  $m = 3.0$ ). In general,  $\lambda_{AASHTO}$  increases with  $m$ . For Detail Category A, these results suggest  $\lambda_{AASHTO}$  should be in the 0.9 – 1.0 range to ensure a level of safety consistent with the current design provisions for steel. For Detail Categories C to F, the current value of 0.75 may still be adequate. Table 3.3 provides a summary of the fatigue correction factor,  $\lambda_{AASHTO}$ , for each detail category including  $m = 3.0$ .

Table 3.6: AASHTO fatigue correction factor results

Detail Category	$m$	$\lambda_{AASHTO}$	
		Average	Maximum
A	6.85	0.90	1.00
B	4.84	0.81	0.90
C	3.64	0.75	0.84
D	3.73	0.76	0.84
E	3.45	0.74	0.83
F	3.42	0.74	0.83
-	3.0	0.72	0.80

### **3.4 Effect of Overload Events**

The real traffic databases used for the calibration presented in the previous section represent traffic at a specific site for a certain period of time. Although traffic surveys provide a realistic representation of average truck traffic, they may not capture the effects of overloaded trucks or trucks travelling side-by-side. Over the 75 year design life span of a bridge structure, it will experience many heavy loaded trucks; the realistic databases used are small in comparison. It can also be assumed that many overloaded trucks purposely by-pass or avoid weigh-stations. Thus, small databases may not be representative of the passage of overloaded trucks over the life of a bridge structure [Nowak 1999].

For the purpose of this study, trucks in excess of a legal load and multiple trucks travelling simultaneously side-by-side are defined as overload events. The effects of overload events on the calibration of the fatigue load correction factor are investigated in this section. Analysis on the effect of overload events is separated into two cases; firstly, whereby an overload event is represented by an overloaded truck above the legal load and secondly, whereby an overload event is represented by the multiple occurrence of trucks passing over a bridge side-by-side. The effects of overload events on the fatigue load correction factor are investigated using both the Canadian and American traffic databases described earlier.

#### **3.4.1 Case One: Overloaded Trucks**

An overload event can be defined as the passage of a truck over a bridge that is loaded in excess of the legal load that the bridge is designed to accommodate. For shorter span structures or components, overloads may be due to overweight axles or axle groups, rather than entire trucks. As discussed previously in Section 2.6, the CSA-S6 Bridge Code, similar to other design codes, uses a design truck with axle weights and spacings calibrated based on the maximum observed loads on bridges. The design truck is therefore representative of the maximum observed truck loads on bridges for a variety of axle configurations, and thus represents a critical design case for trucks with any number of axles. It can be assumed, however, that in certain instances a truck passing over a bridge structure may carry a load in excess of the design truck. Examples of such instances include mobile crane trucks and trucks used in the forestry industry. Four design trucks from the Forest Service Bridge Design and Construction Manual (FBDM) [MOF 2002] were reviewed. Figure 3.13 provides an example of an off-highway design truck used for bridge design in the forestry industry.

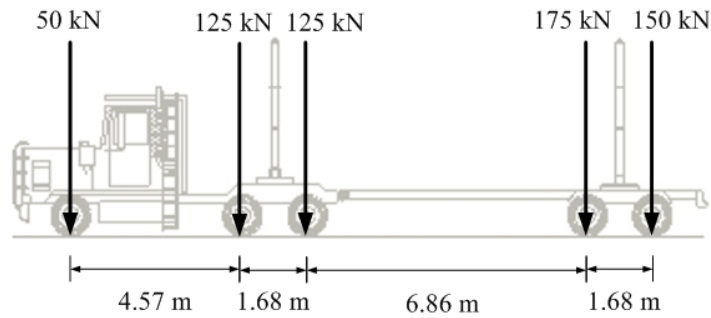


Figure 3.13: FBDM L-165 design truck

Although this is an example of an off-highway truck, it is assumed that trucks such as those used by the forestry industry may travel illegally on interprovincial highways from time to time. Similar to the study prescribed by CSA-S6 for the CL-625 truck discussed previously in Section 2.6, the four FBDM design trucks were assessed in accordance with the MOL allowance. The same seven axle groups used in the CL-625 study, were adopted for the five-axle FBDM design trucks: L-75, L-100, L-150, and L-165 (see Figure 2.26). Figure 3.14 provides a comparison of the four FBDM design trucks to the CL-625 truck, the MOL, and OBF.

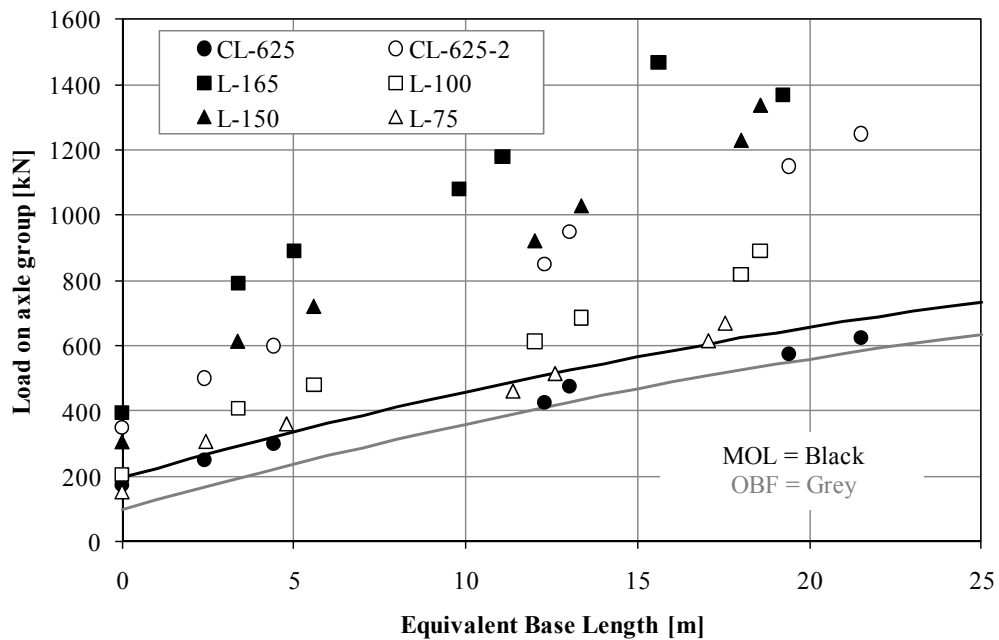


Figure 3.14: FBDM design truck comparison to the MOL and OBF

The equivalent base lengths for all trucks included in this analysis were calculated as outlined by O'Connor and Shaw [2000]. The load effect determined by various axle groups for FBDM trucks,

demonstrate loads in excess of the MOL and OBF. The equivalent base lengths and axle group loads were also determined for two times the axle loads of the CL-625 truck (CL-625-2), which serves as a simulated overload truck here. Both the L-150 and L-165 trucks exhibit loading in excess of the CL-625-2 overload truck.

Agarwal and Lane [1980] conducted a similar study of permissible weights of mobile crane trucks manufactured at that time and found that a portion of those trucks reviewed did not satisfy weight requirements for Single Trip and Annual permits. These crane trucks not satisfying weight restrictions, similar to the FBDM trucks, also exceed the MOL and OBF.

The effect of overloaded trucks on the fatigue correction factor for both Ontario and American traffic will be discussed herein. The original truck databases for the Ontario and American traffic will be modified to include overloaded trucks applied at different frequencies. An overloaded truck is defined as two times the axle weights of the design code truck for the Canadian and American code trucks; CL-625 and HS20-44, respectively (Figure 3.15). This was considered to be a reasonable assumption, since both codes assume the life of a fatigue detail is infinite if the stress range imposed by the code truck is less than 50% of the constant amplitude threshold. The overloaded truck is applied at frequencies of 0.01% and 0.1%.

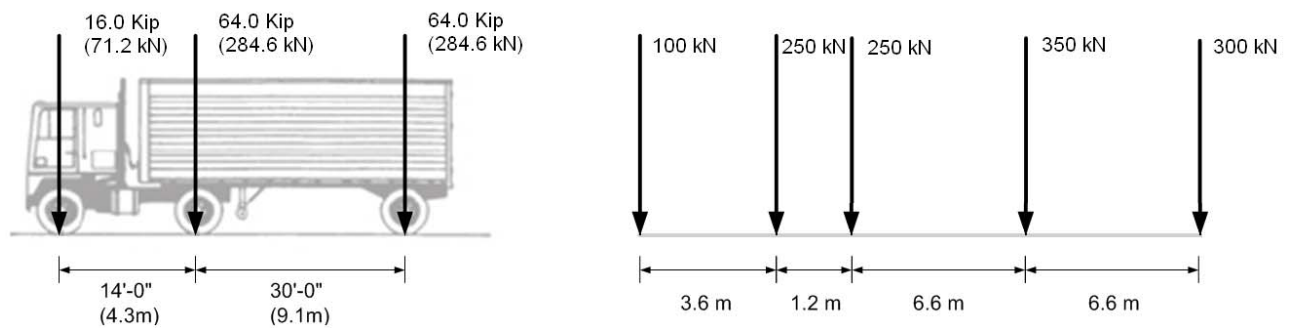


**Figure 3.15: Overloaded trucks using modified HS20-44 (left) and modified CL-625 (right)**

The database for Ontario traffic was reduced to a size of 10000 trucks and modified to include 1 or 10 overloaded trucks representing overload frequencies of 0.01% and 0.1%, respectively. Using the calibration procedure outlined in Section 3.1, fatigue load correction factors were generated for the two databases including overloaded trucks and compared to the correction factors previously determined using the original Ontario traffic database. The results are summarized in Figure 3.16.

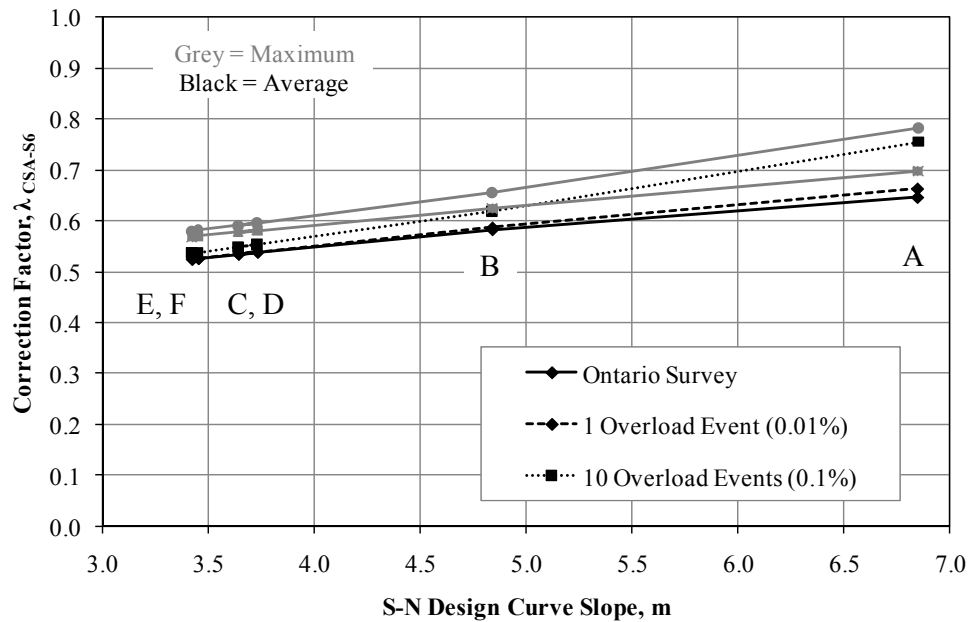


**Figure 3.16: CSA-S6 correction factor results for overload events**

Figure 3.16 shows little difference in the fatigue load correction factor between the original Ontario traffic and overloaded trucks applied at a frequency of 0.01%. A more pronounced variation in the correction factor is seen applying overloaded trucks at a frequency of 0.1%, especially for the higher detail categories. To determine the sensitivity of the fatigue correction factor to the extreme case of two times the axle weights of the CL-625 truck, results were also formulated using overload trucks with 1.5 and 1.0 times the CL-625 truck axle weights at the critical frequency of 0.1% (Figure 3.17).

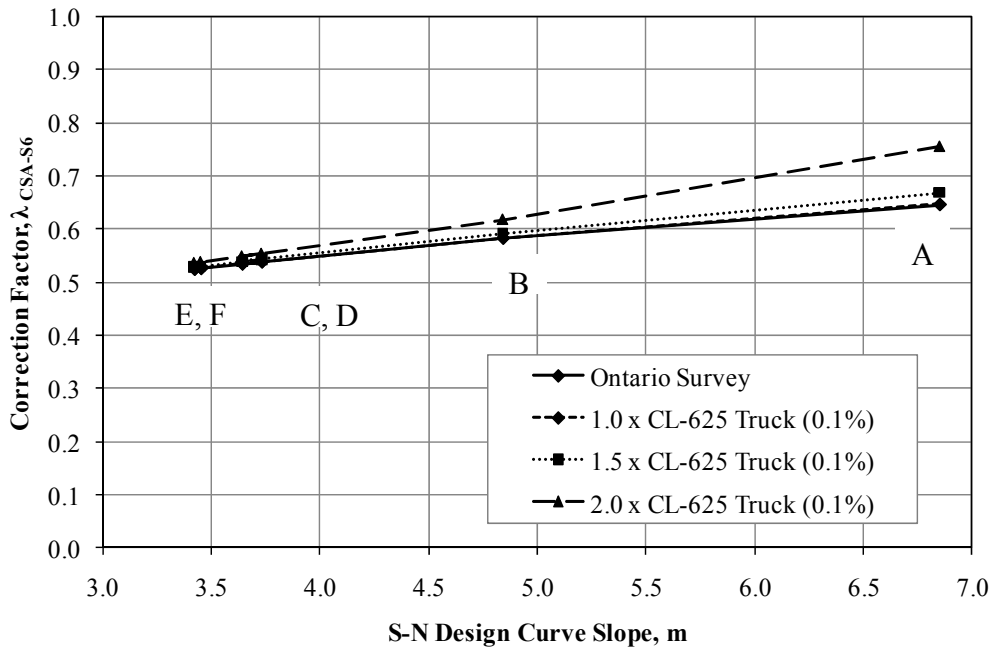


Figure 3.17: CSA-S6 correction factor results for CL-625 amplified by 1.0, 1.5, and 2.0

Figure 3.17 shows that by amplifying the CL-625 axle loads by 1.0 or 1.5 times has little effect on the fatigue correction factor. Thus, a change in the fatigue correction factor, due to overloaded trucks, is only warranted when considering an overload of two times the axle loads for the CL-625 truck.

Similarly, the database for American traffic was reduced to a size of 20000 trucks and modified to include 2 or 20 overloaded trucks representing frequencies of 0.01% and 0.1%, respectively. Using the calibration procedure outlined in Section 3.1, fatigue load correction factors were generated for the two databases with overload events and are compared to the correction factors previously determined using the original American traffic database. The results are summarized in Figure 3.18.

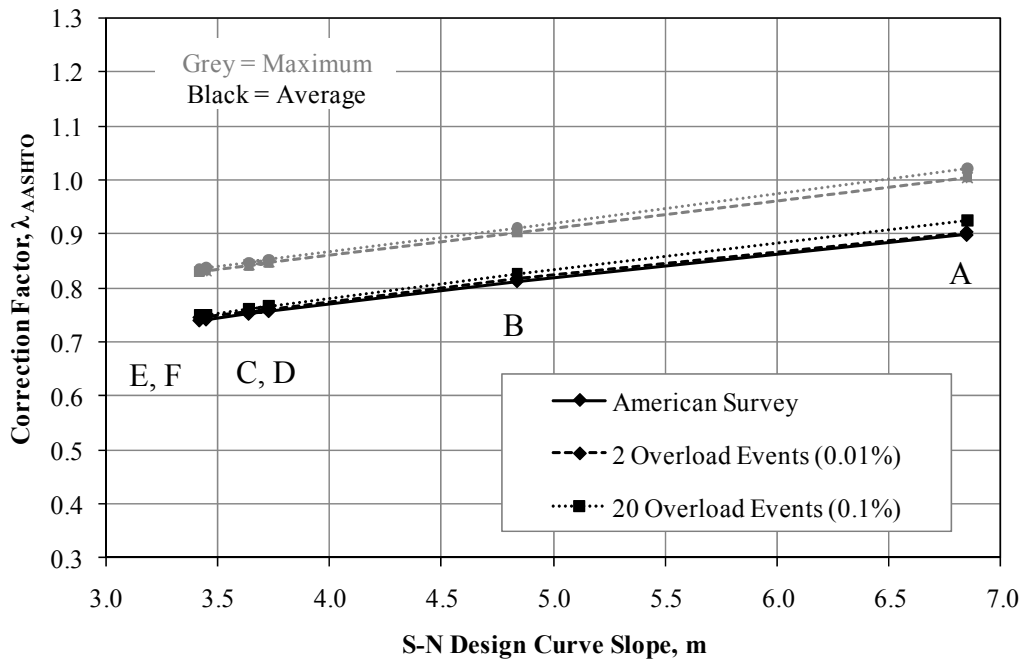


Figure 3.18: AASHTO correction factor results for overload events

Similar to the Ontario traffic, Figure 3.18 shows little difference in the fatigue load correction factor between the original American traffic and overloaded trucks applied at a frequency of 0.01%. In contrast to the Ontario data, the correction factors with overloads at a frequency of 0.1% are also very similar to the original American traffic. In general for both cases, there is little influence in the fatigue load correction factor from overloaded trucks at frequencies of 0.01% and 0.1%. This may be due in part to the HS20-44 truck being lighter than the CL-625 truck.

### 3.4.2 Case Two: Multiple Occurrences of Trucks

Overload events are also assumed to occur as a result of the passage of two trucks simultaneously side-by-side across a bridge structure. As discussed in Chapter 2, Nowak [1999] notes that occurrences of the passage of two trucks simultaneously can be modelled by two cases; firstly, where one lane is fully loaded and the other lane is unloaded, and secondly, where both lanes are loaded. When both lanes are loaded, the distribution of load between the two lanes is defined by three levels of correlation; no correlation, partial correlation, and full correlation, where correlation is based strictly on the axle weights. Based on observations made by Nowak [1999] it can be assumed that every 15<sup>th</sup> truck passage over a bridge (on average) is accompanied by a simultaneous side-by-side passage of another truck. Every 150<sup>th</sup> truck passage represents simultaneous passage of two trucks

over a bridge with a 50 percent weight correlation or partial correlation. Every 450<sup>th</sup> truck passage represents simultaneous passage of two trucks over a bridge with full correlation. All other simultaneous passage of trucks over a bridge structure are said to have no correlation. Nowak's live load model is widely used and relatively straightforward to implement and is thus adopted for use herein.

The problem is first bounded by adopting two simplified cases for the multiple occurrences of trucks. Firstly, to determine a lower bound solution, the original truck database is altered to include the passage of two fully correlated trucks at every 450<sup>th</sup> truck passage. Thus, the axle weights of every 450<sup>th</sup> truck are doubled to simulate two trucks, with the same axle weights and spacings, crossing the bridge structure simultaneously side-by-side. A second case was used to generate an upper bound solution to determine the effect of overload events on the fatigue load correction factor. This case was formulated by altering the original truck database by including the passage of two fully correlated trucks at every 15<sup>th</sup> truck passage. Similarly to the first case, the axle weights of every 15<sup>th</sup> truck are doubled to simulate two trucks, with the same axle weights and spacings, crossing the bridge structure simultaneously side-by-side.

Once the problem is bounded by the two cases for multiple occurrences of trucks listed above, a third case using Nowak's live load model is formulated using different levels of correlation (zero, partial, and full) by truck weight. This final case will serve as a realistic representation, as to the effect of overload events on the fatigue load correction factor. Both the Ontario and American truck databases, previously outlined in this chapter, will serve as the original truck databases for use in all cases herein.

#### 3.4.2.1 Fully Correlated Trucks every 450<sup>th</sup> Passage

The case where two fully correlated trucks pass across a bridge every 450<sup>th</sup> occurrence represents a lower bound solution. For simplicity, this scenario does not consider zero and partial correlation, and only considers full correlation. Both the Ontario and American truck databases were altered by doubling the axle weights of every 450<sup>th</sup> truck in the database to represent two fully correlated trucks simultaneously crossing a bridge side-by-side.

For the Ontario traffic, two new databases were generated including overloads at every 450<sup>th</sup> truck. The first database used a sample size of 10000 trucks, including overload events, thus representing the size of the original traffic survey. Overload events inputted into the database correspond to the



truck axle weights being doubled at the 450<sup>th</sup> interval, but the truck at the 450<sup>th</sup> interval does not necessarily represent the heaviest truck in the sample. Therefore, for a small sample size such as the 10000 truck database used here, the trucks that are considered overload events may not include the most critical or heaviest trucks in the sample. Thus, another database using a sample size of 100000 trucks, including overloads, is used to increase the probability that the trucks with critical or higher weights will be included in the study. To develop the larger database, the original Ontario database of 10198 trucks was randomized ten times to generate a random sample of 100000 trucks. Using the calibration procedure outlined in this chapter, fatigue load correction factors are generated for the two databases with overload events and are compared to the correction factors previously determined for Ontario traffic (Figure 3.19).

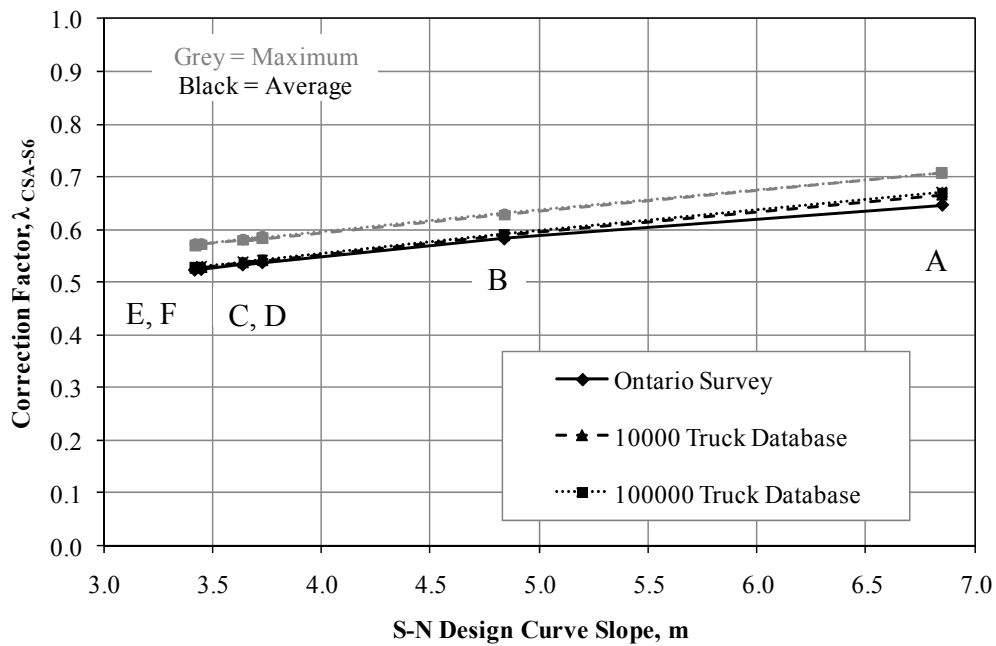


Figure 3.19: CSA-S6 correction factor results for overloads every 450<sup>th</sup> truck passage

Figure 3.19 shows that the presence of overload events has little effect on the fatigue load correction factor in the case of two fully correlated trucks passing across a bridge every 450 trucks. Comparison of the two databases (10000 trucks and 100000 trucks) in this case, validates that use of a smaller sample size will not affect the fatigue load correction factor.

The same study was also completed for American traffic. Similarly, two databases were generated, the first using the original sample size of American traffic (25000 trucks), and the second using a random sample of 100000 trucks from the American traffic survey. These two databases were then

modified to include an overload event of two fully correlated trucks travelling simultaneously every 450<sup>th</sup> passage across a bridge. Again, using the calibration procedure outlined in this chapter, fatigue load correction factors are generated for the two databases with overload events and are compared to the correction factors previously determined for American traffic (Figure 3.20).

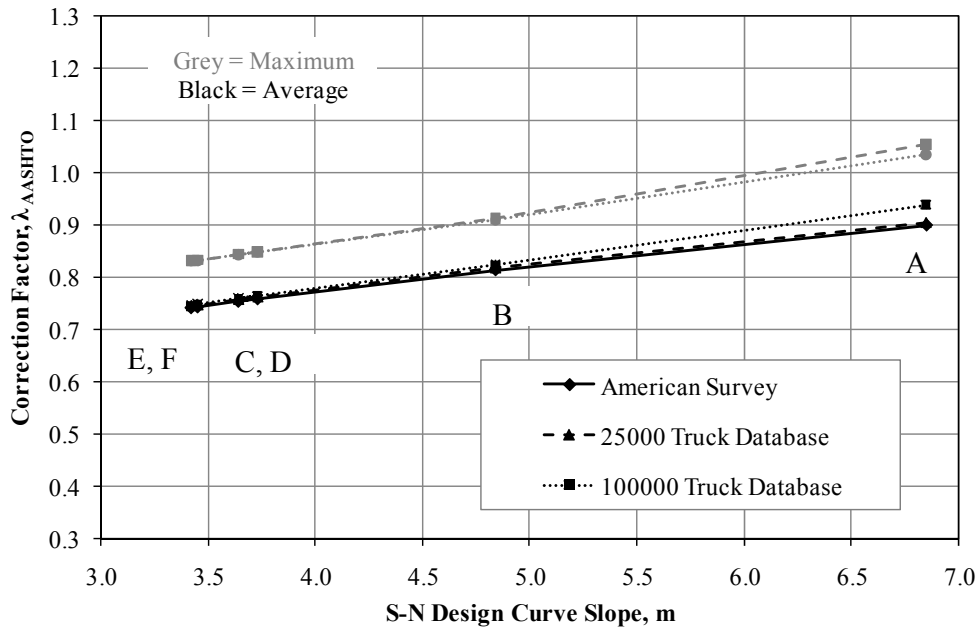


Figure 3.20: AASHTO correction factor results for overloads every 450<sup>th</sup> truck passage

Similarly to the Ontario traffic data, Figure 3.20 shows that the presence of overload events has little effect on the fatigue load correction factor in the case of two fully correlated trucks passing across a bridge every 450 trucks. Comparison of the two databases (25000 trucks and 100000 trucks) in this case, validates that also for American traffic the use of a smaller sample size has little affect on the fatigue load correction factor.

### 3.4.2.2 Fully Correlated Trucks every 15<sup>th</sup> Passage

The case where two fully correlated trucks pass across a bridge every 15<sup>th</sup> occurrence represents an upper bound solution as it accounts for the fact that every 15<sup>th</sup> truck is side-by-side with another but for simplicity assumes fully correlation for all occurrences and does not consider the cases of zero and partial correlation. Both the Ontario and American truck databases were altered by doubling the axle weights of every 15<sup>th</sup> truck in the database to represent two fully correlated trucks simultaneously crossing a bridge side-by-side.

For the Ontario traffic, three new databases were generated including overloads at every 15<sup>th</sup> truck. All three databases contain the same sample size of 10000 trucks, but the original Ontario traffic survey used to generate each sample was randomized. Each database was then modified to include an overload event of two fully correlated trucks travelling simultaneously every 15<sup>th</sup> passage across a bridge. Using the calibration procedure outlined in this chapter, fatigue load correction factors are generated for the three databases with overload events and are compared to the correction factors previously determined for Ontario traffic (Figure 3.21).

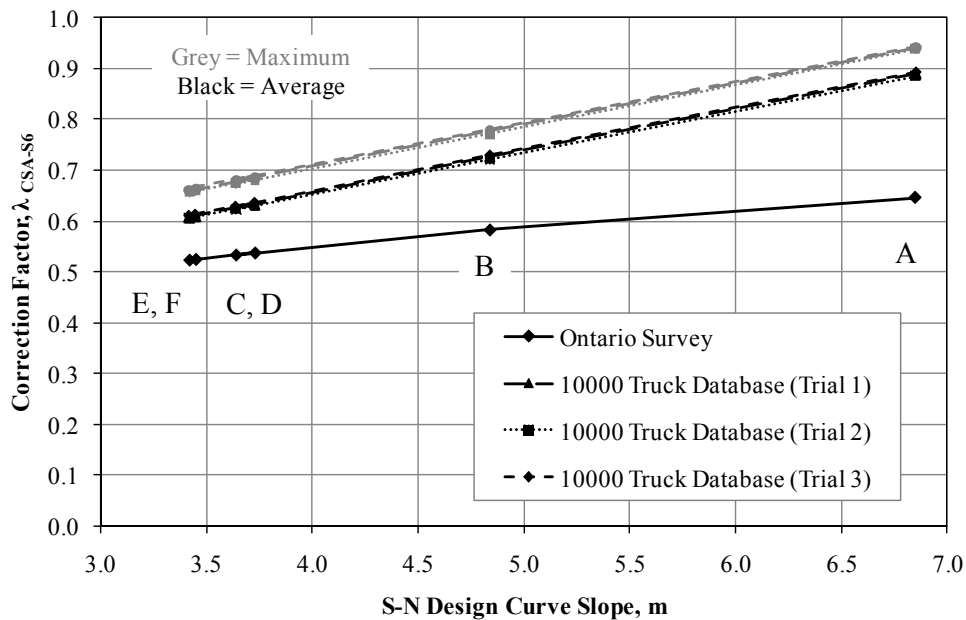


**Figure 3.21: CSA-S6 correction factor results for overloads every 15<sup>th</sup> truck passage**

Figure 3.21 shows that the presence of overload events every 15<sup>th</sup> truck has a significant effect on the fatigue load correction factor in the case of two fully correlated trucks passing across a bridge. There is little difference between the three randomized 10000 truck databases, which confirms that the order of trucks does not affect the fatigue load correction factor.

The same study was also completed for American traffic. Similarly, three databases were generated, all using a randomized sample of the American traffic survey. These three databases were then modified to include an overload event of two fully correlated trucks travelling simultaneously every 15<sup>th</sup> passage across a bridge. Again, using the calibration procedure outlined in this chapter, fatigue load correction factors are generated for the two databases with overload events and are compared to the correction factors previously determined for American traffic (Figure 3.22).

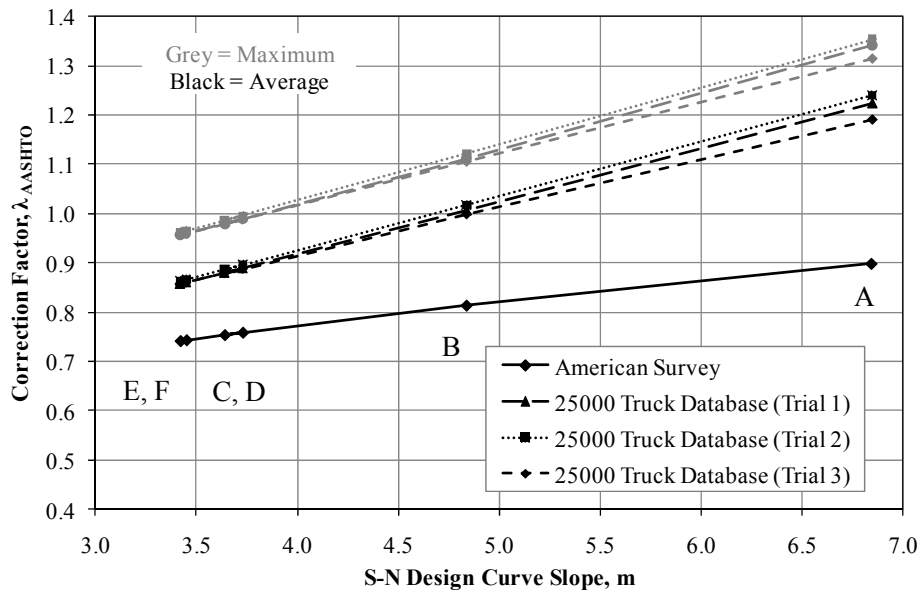


Figure 3.22: AASHTO correction factor results for overloads every 450<sup>th</sup> truck passage

Similarly to the Ontario traffic data, Figure 3.22 shows that the presence of overload events has a large effect on the fatigue load correction factor in the case of two fully correlated trucks passing across a bridge every 15 trucks. The difference between the correction factor for the original traffic survey and those including overload events is even more pronounced than the same study using the Ontario traffic. It is assumed this is true because the American traffic database is formulated based on idealized truck weights and spacings. Due to simplifications for axle weights and spacing for a large range of trucks, the average axle weights are greater for the American survey. Again, there is little difference between the three randomized databases for American traffic, thus the order of occurrence of truck types will not affect the fatigue load correction factor.

### 3.4.2.3 Three Levels of Correlation every 15<sup>th</sup> Passage

The final case used Nowak's [1999] live load model to provide a realistic representation of the effects of multiple presence loading of trucks. The FORTRAN 95 program used to determine the fatigue correction factor was altered to account for the three scenarios, zero, partial, and full correlation, when trucks pass over a bridge simultaneously. Nowak's live load model assumes no correlation for every 15<sup>th</sup> truck passage, 50 percent or partial correlation for every 150<sup>th</sup> truck passage, and full correlation for every 450<sup>th</sup> truck passage. To accomplish this, the truck database was sorted by truck weight from lightest to heaviest. Each truck in the database was assigned a number ( $w_i$ ). To determine

which truck was passed across the bridge, a random number ( $z_i$ ) was generated between 0 and 1 which corresponds to the cumulative distribution of the truck database to select a truck ( $w_i$ ) with associated axle weight and spacing. In the case of a simultaneous truck passage, two random numbers ( $z_1, z_2$ ) were generated and the axle weights and spacing's for two trucks ( $w_1, w_2$ ) were combined using superposition and passed over a bridge (Figure 3.23).

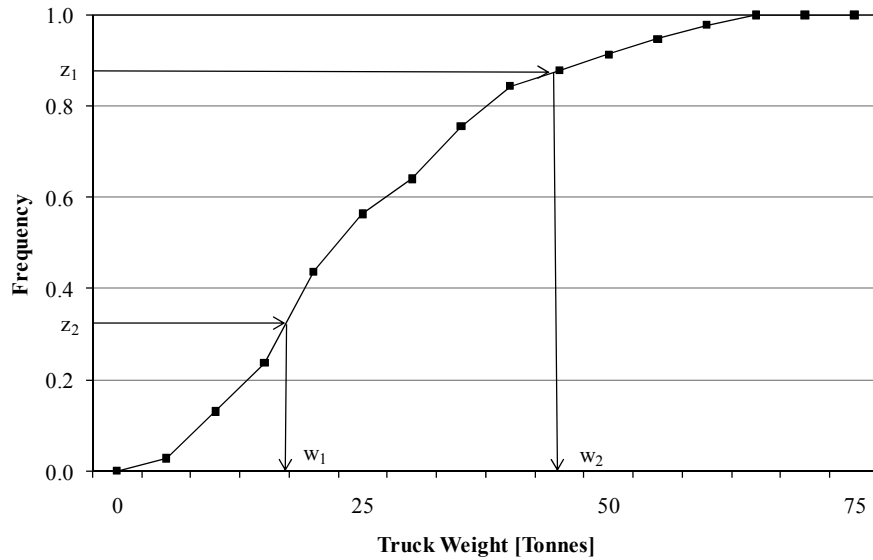


**Figure 3.23: Truck simulation based on GVW cumulative distribution**

The program passes two trucks simultaneously across a bridge on every 15<sup>th</sup> occurrence. At every 15<sup>th</sup> truck passage the program generated two random numbers to model no correlation between truck weights,

$$w_1 = z_1 \quad ; \quad w_2 = z_2 \quad (3.4)$$

At every 150<sup>th</sup> truck passage the program generated two random numbers, but to model 50 percent correlation the second truck weight was determined according to the following,

$$w_1 = z_1 \quad ; \quad w_2 = 0.5 \cdot z_1 + 0.5 \cdot z_2 \quad (3.5)$$

At every 450<sup>th</sup> truck passage the program generated a single random number applied to both trucks to model full correlation as shown below,

$$w_1 = z_1 \quad ; \quad w_2 = z_1 \quad (3.6)$$

To validate the program, additional simulations were completed for the cases presented above in Sections 3.4.2.1 and 3.4.2.2. Results using the Ontario survey and the random truck generation program rendered the same results.

For the Ontario traffic, the FORTRAN 95 program was run for 10198 trucks. Thus, using the calibration procedure outlined in this chapter, fatigue load correction factors were generated using Nowak's [1999] live load model to simulate overload events and compared to the upper and lower bound solutions previously determined for Ontario traffic (Figure 3.24).

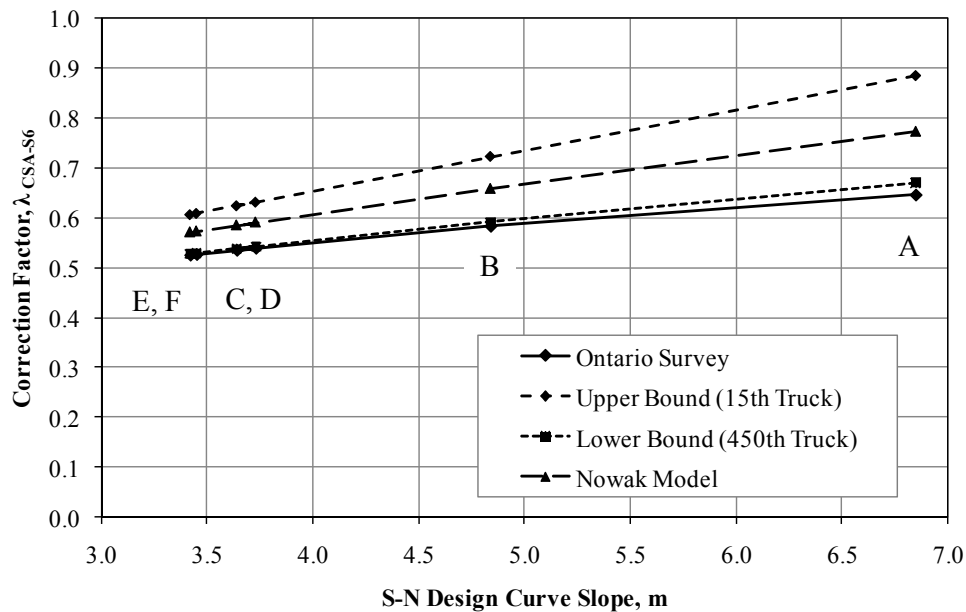


**Figure 3.24: CSA-S6 correction factor results using Nowak and modified Nowak models**

The fatigue correction factor results using the Nowak live load model fall between the bounds, providing further verification of the results. In contrast to the Ontario survey, the live load model proposed by Nowak [1999] shows that overload events have an effect on the fatigue correction factor as shown in Figure 3.25. The model is also run for the case of 100000 trucks, which provides similar results to the first case of 10198 trucks, to eliminate any probability that certain data in the survey is excluded in the study.

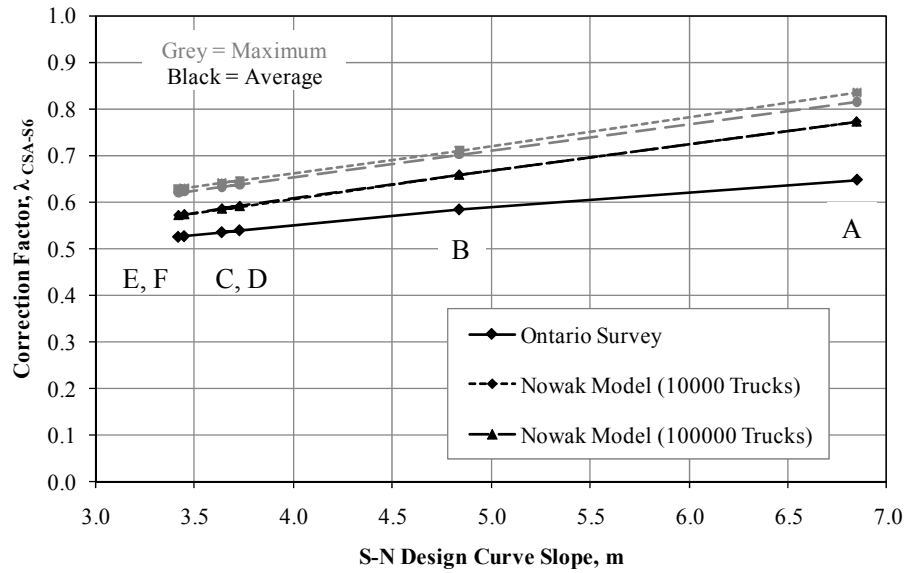


Figure 3.25: CSA-S6 correction factor results using Nowak model

The same study was also completed for American traffic. Similarly, the FORTRAN 95 program is run for 25901 trucks, representing the sample size of the American survey. Thus, using the calibration procedure outlined in this chapter, fatigue load correction factors are generated using Nowak's live load model to simulate overload events and are compared to the upper and lower bound solutions previously determined for American traffic (Figure 3.26).

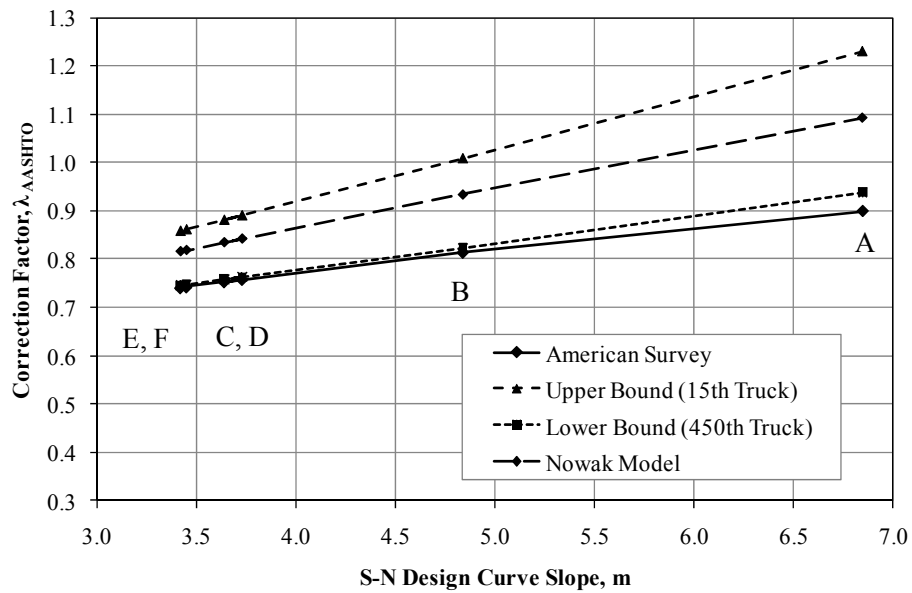


Figure 3.26: AASHTO correction factor results using Nowak and modified Nowak models

Similar to the analysis using Ontario traffic, the fatigue correction factor results using the Nowak live load model fall between the bounds. Thus, in contrast to the fatigue correction values for the American survey, using the live load model proposed by [Nowak 1999] it is apparent that overload events have an effect on the fatigue correction factor as shown in Figure 3.27. Again, the model is also run for the case of 100000 trucks, which provides similar results to the first case of 25901 trucks, to eliminate any probability that certain data in the survey is excluded in the study.

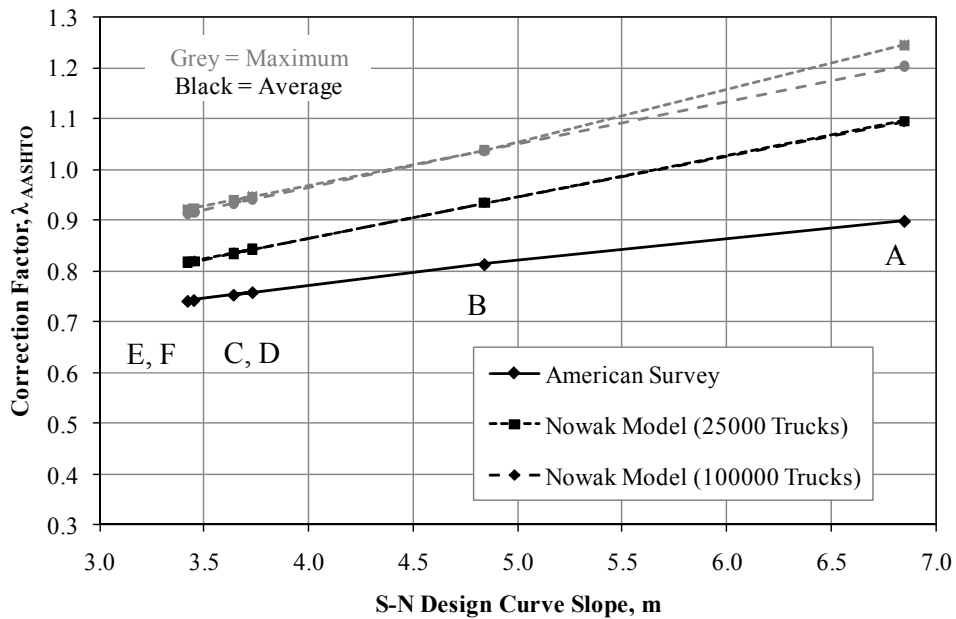


Figure 3.27: AASHTO correction factor results using Nowak model

Through a comparison of the Ontario and American data, it is apparent that in general the presence of overload events has a more pronounced effect on the American data. This can be attributed to the difference between the two truck databases from the Ontario and American surveys. Unlike the Ontario data, the American database uses idealized truck axle weights and spacings, which may cause a more pronounced increase in the fatigue load correction factor as the probability is higher that a heavier truck will be applied as an overload event.

Based on the fatigue correction factors generated using the Nowak live load model, for CSA-S6 and AASHTO, an amplification factor was formulated. In Table 3.7, the amplification factor or ratio of fatigue corrections factors derived using the assumed simultaneous vehicle crossing model and raw truck survey data are compared.



**Table 3.7: Simultaneous truck crossing amplification factor**

<b>Detail Category</b>	<b><i>m</i></b>	<b><math>\lambda_{CSA-S6}</math></b>		<b><math>\lambda_{AASHTO}</math></b>	
		<b>Average</b>	<b>Maximum</b>	<b>Average</b>	<b>Maximum</b>
A	6.85	1.19	1.19	1.22	1.20
B	4.84	1.13	1.13	1.15	1.15
C	3.64	1.09	1.10	1.11	1.11
D	3.73	1.10	1.10	1.11	1.11
E	3.45	1.09	1.09	1.10	1.11
F	3.42	1.09	1.09	1.10	1.11
-	3.0	1.08	1.08	1.09	1.09
<b>Average</b>		<b>1.11</b>	<b>1.11</b>	<b>1.12</b>	<b>1.13</b>

Ratios were calculated for each AASHTO detail category, resulting in amplification factors ranging between 1.08 and 1.22 with an average of 1.12. The amplification factor is a function of detail category and whether the average or maximum fatigue correction factor curves were used.

## Chapter 4

### Fatigue and Materials Testing

The main objectives of the testing program described in this chapter are; firstly to develop a database of constant and variable amplitude fatigue test data for comparison with existing design S-N curves and to expand the existing, limited database of test results of aluminum welds under VA loading, and secondly, to determine material properties of the fatigue specimens for use in a fracture mechanics analysis, which is presented in Chapter 6.

In this chapter, the fatigue testing program is discussed in Section 4.1. This program consisted of fatigue tests on non-load-carrying transverse stiffener specimens under CA and VA loading. In Sections 4.2 to 4.5, additional tests to characterise the material properties of the fatigue specimens are described. These include static tensile, cyclic, microhardness, and residual stress testing.

#### 4.1 Fatigue Testing

In the following sections the fatigue test programs, specimens, and testing apparatus are described in detail.

##### 4.1.1 Test Program

The testing program conducted for this study included the fatigue testing of 32 small-scale non-load carrying fillet welded transverse stiffener details under CA and VA loading conditions. All test specimens were loaded axially. Testing under CA loading was conducted at  $R$ -ratios of -1.0, 0.4, and 0.1 and at varied nominal stress ranges,  $\Delta S$ , to establish the slope and position of the S-N curve for the respective detail category. Various  $R$ -ratios were considered to study the effects of this parameter and to facilitate estimation of the residual stresses (see Chapter 6).

VA testing was conducted using two nominal stress histories developed from Ontario traffic data to simulate realistic cyclic loading conditions. The Ontario truck data used for this purpose was the same data from the 1995 survey used in Chapter 3 to establish fatigue correction factors for aluminum. Based on the Ontario survey, two 200 peak sample histories were extracted. All of the truck weights in the Ontario survey and GVW histogram were taken with trucks in a stationary position, thus these truck weights represent static weights. In accordance with CSA-S6, a dynamic load allowance (DLA) of 1.25 is applied to the static truck axle weights to approximate dynamic loading effects.

The two load effect histories were generated by passing trucks over the influence lines for two different bridge configurations. These configurations were chosen to cover a range of typical load history characteristics typical of highway bridges; the *ps-m* influence line for a 40 m span (referred as load history one or LH1) and the *ps-r* influence line for a 15 m span (referred as load history two or LH2) (Figure 4.1).

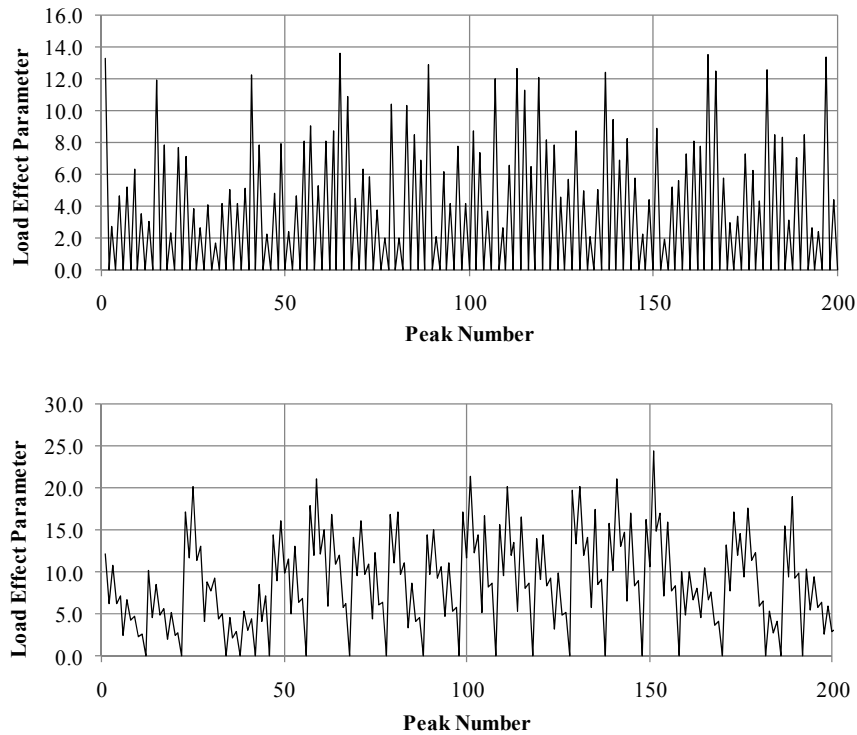


**Figure 4.1: VA load histories for LH1 (top) and LH2 (bottom)**

In Figure 4.1, significant differences between the two load histories is apparent. In load history one, since the bridge span chosen is larger than the truck length, each truck passage tends to cause one large load cycle; therefore, the result is a narrow-banded load history. The second load history can be characterised as wide-banded: as each truck enters and leaves the shorter span, the individual axles cause small load cycles.

By simply scaling the load effect history, testing histories can be generated for different equivalent stress ranges. A nominal equivalent stress range is calculated using Miner's Sum as discussed in Section 2.3.1, but a constant S-N curve slope of  $m = 3.64$  for AASHTO Detail Category C for a non-load-carrying transverse stiffener was used. In this study, a nominal stress,  $S$ , is used determine the stress range for all tests opposed to the local stress or *hot-spot stress* at the weld toe as shown below,

$$S = \frac{F}{A} \quad (4.1)$$

The test matrix for fatigue testing under CA and VA loading is shown in Table 4.1.

**Table 4.1: Fatigue test matrix**

<b>Constant Amplitude</b>		
<b>R-Ratio</b>	<b>Stress Ranges Tested, <math>\Delta S</math> [MPa]</b>	<b>No. Tests (each <math>\Delta S</math>)</b>
-1.0	70(B5), 80(G5), 90(A5), 100(G3) 120(A2), 150(A3), 170(A4), 200(A1)	1
0.1	60(B4), 70(B3), 80(B2), 90(B1)	1
0.4	50(G4), 60(F5), 70(F4), 80(F3)	1
<b>Variable Amplitude</b>		
<b>Load History</b>	<b>Eq. Stress Ranges Tested, <math>\Delta S_{eq}</math> [MPa]</b>	<b>No. Tests (each <math>\Delta S</math>)</b>
LH1	20(C4), 40(E1), 60(C5)	1
LH1	30(E2,E4,E5), 75(C1,C2,C3)	3
LH2	30(H4,H5,J1), 75(H1,H2,H3)	3

\*\*\*Associated Specimen Numbers in Brackets

A majority of the testing was conducted between stress ranges of 60 to 100 MPa, similar to past fatigue testing of aluminum, as discussed in Chapter 2. Further testing above 100 MPa is undertaken to observe the fatigue behaviour at very high stress ranges and testing below 60 MPa provides valuable information, especially under VA loading conditions, regarding the potential for a second-slope of the S-N design curve in the high cycle regime.

#### 4.1.2 Test Specimens

The test specimens were fabricated from 3/8" (9.5 mm) thick 6061-T651 aluminum plate with a transverse attachment fillet welded at the mid-height of the plate. In structural application 6061 aluminum is the most widely used alloy in North America because of its high strength, good corrosion resistance, and weldability; thus, 6061-T651 was chosen for this study. The proof stress of 6061 aluminum alloys is similar to that of mild steel, providing a strong resemblance to structural steel design and making it a common choice for structural design. 6061 aluminum alloy contains elements of aluminum, magnesium, silicon, and copper. Tempering of T651, similar to T6, is obtained by a solution heat treatment followed by artificial aging [Gitter 2005]. All welded joints

were fabricated using gas metal arc welding (GMAW) process with 5356 aluminum weld metal filler. Their geometry is described in Figure 4.2.

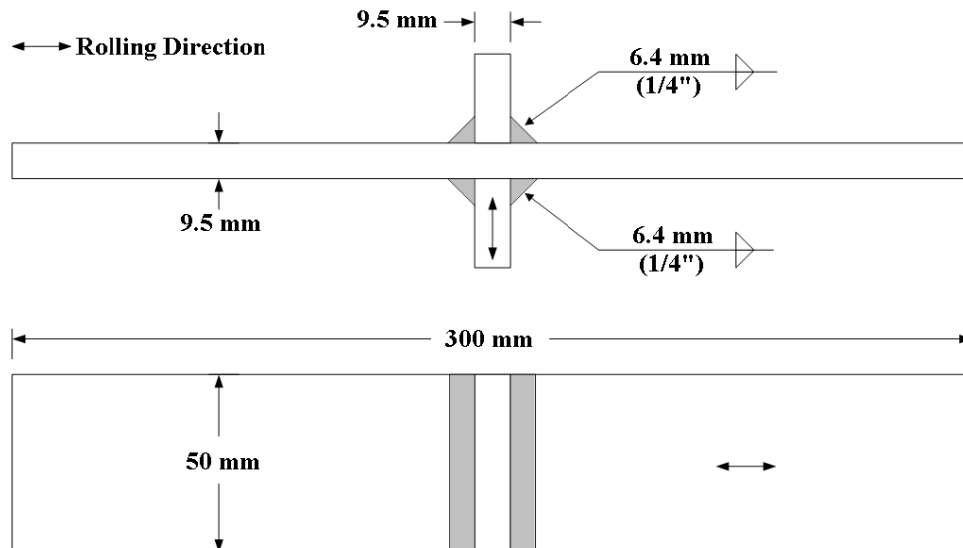


**Figure 4.2: Fatigue test specimen geometry.**

Eight aluminum panels with transverse welded attachments on both sides, similar to that shown in Figure 4.3 (left), were fabricated and subsequently saw-cut into five 50 mm wide specimens per panel (Figure 4.3, right). The rolling direction of the native aluminum plate was maintained in the longitudinal direction of all test specimens (see Figure 4.2).



**Figure 4.3: Specimen fabrication; aluminum panels (left) and saw-cut specimens (right)**

Two different batches of 6061-T651 aluminum panels were fabricated on different occasions; four panels in both batches (eight in total). The aluminum panels were labelled using a letter classification;

A, B, C, E for batch one, and F, G, H, J for batch two. Each panel rendered five fatigue specimens, subsequently labelled by number, from one to five, with the associated panel classification. For example, the first specimen from panel A in the first batch of specimens is labelled A1 and so forth. As-tested specimen dimensions were measured prior to testing, to determine the cross-sectional area of each specimen, so the nominal stress range calculations could be modified accordingly (Table 4.2).

**Table 4.2: Cross-sectional dimensions of fatigue test specimens**

Batch 1				Batch 2			
Specimen	b [mm]	t [mm]	Area [mm <sup>2</sup> ]	Specimen	b [mm]	t [mm]	Area [mm <sup>2</sup> ]
A1	50.09	9.93	497.09	F1	48.75	9.49	462.39
A2	50.49	9.80	494.75	F2	50.00	9.46	472.70
A3	50.14	9.79	490.62	F3	50.36	9.49	477.66
A4	49.40	9.76	481.90	F4	50.10	9.49	475.15
A5	51.82	9.76	505.50	F5	50.32	9.49	477.54
B1	50.41	9.76	491.70	G1	49.59	9.45	468.63
B2	49.78	9.80	487.55	G2	49.99	9.45	472.41
B3	49.35	9.78	482.35	G3	50.09	9.47	474.10
B4	50.18	9.79	491.01	G4	50.60	9.51	480.95
B5	52.40	9.77	511.69	G5	50.82	9.47	481.22
C1	51.40	9.72	499.30	H1	49.48	9.59	474.27
C2	51.35	9.76	501.18	H2	50.48	9.53	480.77
C3	51.14	9.73	497.54	H3	50.04	9.45	472.63
C4	51.26	9.74	499.22	H4	50.80	9.53	483.82
C5	50.09	9.72	486.58	H5	51.71	9.56	494.09
E1	51.32	9.75	500.06	J1	48.94	9.51	465.37
E2	51.68	9.77	504.61	J2	51.90	9.47	491.49
E3	51.31	9.76	500.53	J3	50.84	9.49	482.42
E4	51.08	9.77	498.75	J4	50.20	9.50	476.85
E5	50.97	9.83	501.04	J5	51.10	9.52	486.22

### 4.1.3 Test Equipment and Procedure

Fatigue testing of all specimens was undertaken using a MTS 810 Materials Testing System in the University of Waterloo's Structures Laboratory, which is an integrated testing package with a load capacity of  $\pm 100$  kN, equipped with hydraulic control, hydraulic power, and hydraulic actuated grips (Figure 4.4). The MTS Station Manager software package uses MultiPurpose Testware to input constant and variable amplitude loading spectrums and control station limits.

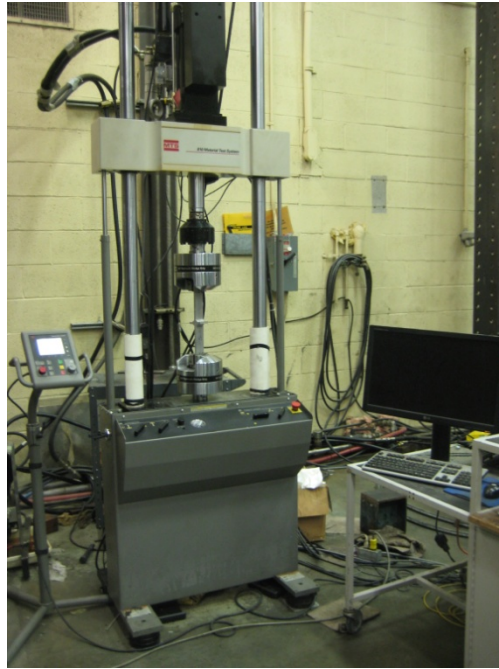


**Figure 4.4: MTS 810 material testing frame**

The fatigue testing was conducted under load control, while data acquisition of the peak axial loads and displacements was recorded through the MTS MultiPurpose Testware software. Each specimen was carefully inspected before testing to ensure no visible flaws and good weld quality. The specimen ends were placed into the hydraulic actuated grips, one fixed to the movable crosshead at the top of the test frame and the other fixed to the stationary grip on the bottom. The duration of each test was governed by the specimen's fatigue life to failure at a cycling frequency of 8 Hz; the only exceptions to this test speed were the variable amplitude tests at equivalent stress ranges of 30 MPa and 20 MPa, which were tested at a frequency of 28 Hz. The testing frequencies at these lower stress ranges were increased to facilitate the extended duration of testing. The station limits for axial load and axial displacement were set to trip at the onset of specimen failure, stopping the test if the axial load or displacement changed dramatically. The axial load limit was set to  $\pm 5$  kN which, if exceeded, stopped the test due to excessive drift of the applied cyclic load peaks. The axial displacement limits were set to  $\pm 0.1$  mm to  $\pm 0.25$  mm which, if exceeded, stopped prior to complete specimen failure. With the axial displacement limits set, the tests generally stopped around the time that a crack visible to the naked eye first appeared.

After crack detection, the fatigue test specimens were sprayed with a dye penetrant, Magnaflux Spotcheck SKL-SP1, to allow the crack shape at the weld toe to be measured later. The dye penetrant

was allowed to cure for a minimum of 48 hours. The specimen was then cyclically loaded to complete failure, under the same CA or VA loading conditions to which it had been previously subjected. Upon complete failure, where (by definition) the specimen was separated into two pieces at the crack site, a semi-elliptical crack shape was fitted to the dyed region of the failure surface to obtain a crack shape ratio measurement (Figure 4.5).

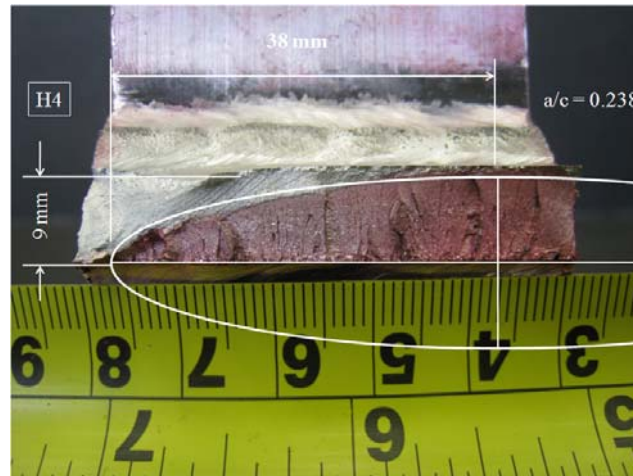


**Figure 4.5: Crack shape ratio estimation using dye penetrant (specimen H4 shown)**

Figure 4.5 shows an example of the crack shape measurements recorded for test specimen H4, where the crack propagated from the weld toe. Based on the semi-elliptical shape fit to the failure surface, the half semi-elliptical width and depth were measured for all specimens tested.

For classification of the crack shape measurements, the specimens were subdivided into five categories, based on the quality of the dye penetrant staining and whether the crack shape exceeds the specimen width. If the quality of the dye penetrant was not satisfactory or the dye penetrant bled outside the fatigue crack region, measurement becomes difficult and less precise. Based on the quality and effectiveness of the dye penetrant staining, three classifications are used: good, satisfactory, and not satisfactory (Figure 4.6).





**Figure 4.6: Dye penetrant quality classification**

Specimens for which the dye penetrant staining quality was not satisfactory were excluded from the analysis, as the crack shape was not well defined and estimation of the crack shape difficult.

Specimens classified as both “good” or “satisfactory” were categorized further, depending on the crack shape exceeding the width of the specimen, on one or both sides. In Figure 4.6, the “good” specimen is representative of the crack shape exceeding the specimen width on one side only and the “satisfactory” specimen is representative of the crack shape exceeding the specimen width on both sides. It was assumed that when the crack exceeds the width of the specimen, the crack shape may be skewed, thus potentially providing less accurate results. Table 4.3 provides a summary of the crack shape classification used, with Class 1 providing the most accurate results and Class 5 the least accurate.

**Table 4.3: Crack shape ratio comparison**

<b>Class</b>	<b>Dye Penetrant Quality</b>	<b>No. Sides Crack Exceeds</b>
1	Good	One
2		Both
3	Satisfactory	One
4		Both
5	Not Satisfactory	N/A

## **4.2 Static Tensile Coupon Testing**

The objective of the static tensile coupon tests performed for the current study was to determine the static material properties of the 6061-T651 aluminum, to facilitate the fracture mechanics analysis presented in Chapter 6. Completion of tensile coupon tests provides the Young’s modulus, yield strength, and ultimate strength.

### **4.2.1 Test Program and Specimen Geometry**

The testing program conducted for this study included tensile testing of five tension coupons under monotonic loading conditions to failure. The tension coupons were fabricated from the same 3/8” (9.5

mm) 6061-T651 aluminum plate used to fabricate the fatigue specimens. During the welding process, the properties of heat treatable alloys such as 6061-T651 aluminum can be altered by the high heat input. The resulting material properties tend to lie somewhere between those of the as-received and fully annealed material. Thus, for the fracture mechanics analysis it was important to have knowledge of the material properties for the upper and lower bounds of the problem; i.e. aluminum in its as-received state (6061-T651) and in a fully annealed state (6061-O). Therefore, tensile tests were conducted on both the as-received and fully annealed aluminum. Five coupon specimens were fabricated according to ASTM E8M-04 (Figure 4.7).

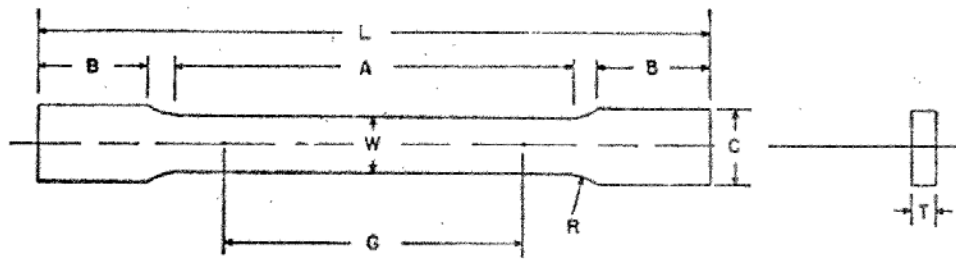


Figure 4.7: Tensile test specimen geometry [ASTM 2004]

Two of the five specimens were subsequently subjected to heat treatment according to ASTM B918M-09 [ASTM 2009] for full annealing.

#### 4.2.2 Test Equipment and Procedure

The MTS 810 material testing frame, mentioned previously, was used to complete all static tensile coupon testing. Full annealing of the aluminum specimens was completed in a heat treatment oven, Thermo Nordmark/Blue M (Figure 4.8). The oven was preheated and maintained at a temperature of 785°F (407°C), before two 6061-T651 tension coupons were laid flat in the oven. To ensure full annealing, the coupons were maintained at a temperature of 785°F (407°C) for a duration of 2-3 hours and cooled at a rate of 50°F/h (28°C/h) until 500°F (280°C), then cooled at an uncontrolled rate to room temperature.



**Figure 4.8: Oven used for full annealing of aluminum specimens**

Similarly to the testing of the fatigue specimens, the tensile coupon testing was conducted under load control, while data acquisition of the axial loads and displacements was recorded through the MTS MultiPurpose Testware software. Each specimen was carefully inspected before testing and the dimensions were recorded for the thickness, width, and gauge length at the critical (reduced) section. The specimen ends were placed into the hydraulic actuated grips, similarly to the fatigue specimens. Each specimen was loaded monotonically beyond yield, unloaded, and reloaded to failure with prescribed loading rates of 1.5 mm/min, 3 mm/min, and 3-15 mm/min for each loading stage, respectively. The MultiPurpose Testware recorded the load and displacement, in N and mm respectively, throughout the test. After failure, the final cross-section dimensions were measured.

### **4.3 Cyclic Coupon Testing**

The objective of the cyclic coupon testing performed for the current study was to determine the cyclic material properties of 6061-T651 aluminum to fit the material behaviour to a Ramberg-Osgood material model. The constants  $K'$  and  $n'$ , associated with this material, were required inputs for the fracture mechanics analysis. Completion of the cyclic tests provided the cyclic strength coefficient ( $K'$ ) and the cyclic strain hardening exponent ( $n'$ ) for as-received and annealed 6061-T651 aluminum.

### 4.3.1 Testing Program and Specimen Geometry

The testing program conducted for this study included cyclic testing of two test specimens under strain control. Similar to the static tension coupon test program, the cyclic testing was completed for both the as-received and fully annealed material. Cyclic coupons were fabricated from the same 3/8" (9.5 mm) 6061-T651 aluminum plate used for the fatigue specimens in an *hourglass* or *dogbone* shape as shown in Figure 4.9.

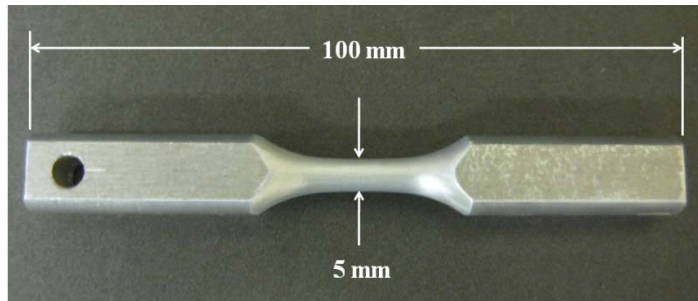


**Figure 4.9: Cyclic test specimen geometry**

One specimen was tested in an as-received state (6061-T651) and another in a fully annealed state (6061-O). The testing was conducted under strain control, by varying the strain in the specimens between  $\pm 0.1\%$  and  $\pm 1.0\%$ , to fit a Ramberg-Osgood material model to the material being tested. At each level of strain tested, load cycles were applied at an  $R$ -ratio of -1.0 for a duration of 10 cycles, and the maximum and minimum load and strain were recorded for each cycle. The level of strain was then increased in increments of 0.1% up to 1.0% and then decreased in increments of 0.1% back to 0.1% strain. This process was repeated until the load was seen to stabilize for each level of strain.

### 4.3.2 Test Equipment and Procedure

Cyclic testing of all specimens was undertaken in a specialized cyclic materials testing frame using a MTS 442 controller with a load capacity of 100 kN, equipped with hydraulic control, power, and actuated grips (Figure 4.4).



**Figure 4.10: Cyclic test frame using MTS 442 controller**

Heat treatment of the cyclic test specimen is completed, in accordance with ASTM B918-18991-1, under the same conditions outlined previously in Section 4.2.1 for static tensile specimens. Full annealing of tensile and cyclic specimens was completed at the same time to ensure the heat treatment conditions were the same. Since the diameter of the cyclic specimens varies along the length, there was a concern that the specimen would *sag* if laid flat and subjected to high temperatures. Thus, an apparatus was fabricated to hang the specimens in the oven while undergoing the full annealing process (Figure 4.11).



**Figure 4.11: Apparatus used to hang specimens during annealing process**

The cyclic specimens were first carefully examined for any scratches or potential stress risers. An M-Coat layer applied at the critical specimen section to give the knife edges of the extensometer

something to *bite* into, without scratching the specimen (Figure 4.12). To apply the M-Coat, the specimen was placed in a lathe and the coating was brushed on as the specimen rotated. A smooth coat was quickly applied, the specimen was then allowed to continue to rotate for 5 minutes to allow the M-Coat to sufficiently harden in a uniform thickness, and the specimen is allowed 24 hours to dry before testing.



**Figure 4.12: Cyclic test specimen with M-Coat**

Once the specimen was placed in the grips, a MTS 632.26 extensometer was attached with small springs on the M-Coated area and stabilized. The Flex v9.11 software package was used to input CA strain cycles, control test speed, and test duration. Readings for load and strain were recorded using voltmeters and converted from volts (V) to kilonewtons (kN) and percent strain ( $\% \epsilon$ ) using machine-specific conversion factors. Each test was completed at a slow test frequency of 0.1 Hz to allow time to manually record the voltmeter readings.

#### **4.4 Microhardness Testing**

As mentioned previously, it is expected that the welding process for heat-treated alloys, such as the 6061-T651 aluminum used in this study, will cause the final material properties in the vicinity of the weld to be somewhere in between those of the as-received and fully annealed material. For the fracture mechanics analysis it was important to determine more precisely the amount of strength loss in the heat affected zone. Material properties for both the 6061-T651 and 6061-O aluminum were determined through tensile and cyclic coupon testing. The objective of the hardness testing performed for the current study was to determine, by indirect means, the strength properties of the aluminum alloy in the HAZ through which the fatigue cracks tended to propagate.

##### **4.4.1 Test Program and Specimen Geometry**

The test program conducted for this study consisted of hardness testing encompassing four cases; the as-received aluminum, the fully annealed aluminum, the weld metal, and the aluminum in the HAZ.

Specimens were fabricated by sectioning existing weld specimens and casting the resulting samples in a plastic resin (Figure 4.13).

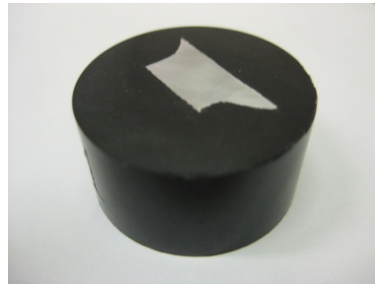


**Figure 4.13: Hardness test specimen**

Once all of the specimens were cast in resin, they were polished to remove all surface imperfections in accordance with [ASTM 2007]. Samples of as-received alloy or base metal (BM), weld metal (WM), and HAZ metal were fabricated from existing untested fatigue test specimens, as shown in Figure 4.14, while the annealed specimens (AM) were fabricated from tensile coupon specimens (Figure 4.14).

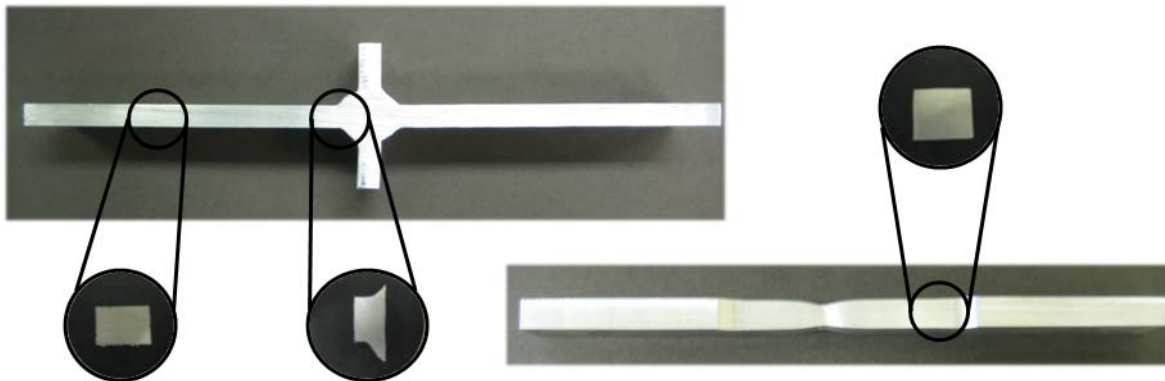


**Figure 4.14: Fabrication of hardness test specimens from existing fatigue and tensile specimens**

Specimens of aluminum in the HAZ provided hardness measurement for both weld metal and HAZ metal since both regions were included in the sectioned samples. Nine hardness tests were conducted according to the test matrix in Table 4.4.

**Table 4.4: Vickers hardness test matrix**

Test	Original Test Type	Material	Test Label
1 - 4	Fatigue	6061-T651	BM
5	Tensile	6061-O	AM
6 - 9	Fatigue	6061-T651 + 5356 weld filler	WM-HAZ

BM = Base Metal    AM = Annealed Metal    WM = Weld Metal    HAZ = Heat Affected Zone

For each specimen, a series of hardness tests are conducted across the thickness of the specimen to determine any changes in hardness across the specimen (Figure 4.15). This is especially crucial for the WM-HAZ specimens, where the largest variations were expected.

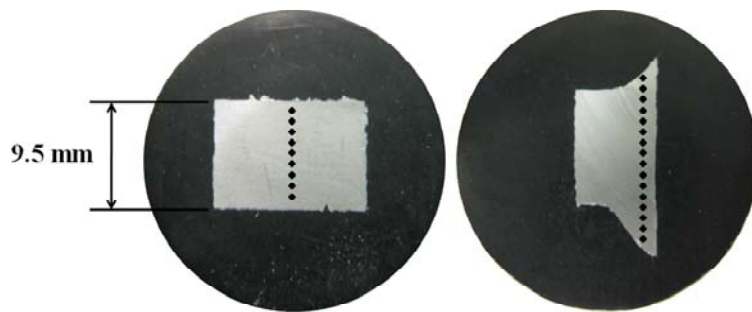


**Figure 4.15: Vickers hardness test locations for BM & AM (left), and WM & HAZ (right)**

#### **4.4.2 Test Equipment and Procedure**

A Vickers hardness testing machine was used to indent the surface of the specimen at multiple locations across its thickness (Figure 4.16). A 200 g load was applied by the indenter to make hardness readings using the Vickers machine. A high powered microscope was then used to measure the size of indentations made by the Vickers indenter (Figure 4.16). The microscope is fitted with a camera and works with Image-Pro 6.3 software to take specimen photographs and hardness measurements.





Figure 4.16: Vickers hardness machine (left) and high-powered microscope (right)

## 4.5 Residual Stress Testing

The objective of the residual stress testing performed for the current study was to determine the residual stresses present in the fatigue testing specimens due to the welding process. Residual stresses have a large impact in the fatigue resistance of aluminum components and for fatigue life prediction using fracture mechanics it is important to have knowledge of the residual stresses present from welding.

### 4.5.1 Test Description

Residual stress testing was outsourced, and conducted by Proto Manufacturing Limited in Oldcastle, ON, Canada. Proto uses x-ray diffraction (XRD) techniques to take residual stress measurements. An un-tested fatigue specimen was used for residual stress testing. XRD is a non-destructive testing technique using the grain structure of the material and comparing it to the atomic lattice spacing; which either expands or contracts under the presence of residual stresses. Proto uses Bragg's Law,

$$\lambda = 2 \cdot d \cdot \sin \theta \quad (4.2)$$

to determine the lattice spacings ( $d$ ). A monochromatic x-ray beam ( $\lambda$ ) is applied to the specimen, which has a lattice spacing ( $d$ ). Interference of the x-ray beam caused by the lattice structure upon application occurs at a measured diffraction angle,  $\theta$ . Since variation in the lattice spacing represents areas of residual stress, different diffraction angles are measured which is represented as a change in

strain. Measured strains are converted to stress to determine the residual stress in the specimen [Pineault *et al.* 1996].

Although XRD surface measurements are non-destructive, to get a profile of the residual stresses through the thickness of the welded plate (ie. along the anticipated crack path) a destructive electron polishing technique was used to remove layers of material and conduct measurements below the surface. Two residual stress profiles were measured at depths up to approximately 1.5mm.

## **Chapter 5**

### **Fatigue and Materials Testing Results**

In this chapter, fatigue testing results for a non load-carrying transverse stiffener, tested under the constant and variable amplitude load histories discussed in Chapter 4, are presented and discussed. In addition, results of materials tests performed to establish input parameter values for use in the fracture mechanics analysis are presented; including results of static tensile, cyclic, microhardness, and residual stress tests.

#### **5.1 Fatigue Testing**

Results of the fatigue tests performed for the current study under constant and variable amplitude loading on 6061-T651 aluminum welded transverse stiffener specimens is presented in this section. The tests were conducted using the specimen details and procedures outlined in Section 4.1. The results of the crack shape measurements for the specimens stained with dye penetrant are also presented.

##### **5.1.1 Test Results and Interpretation**

The fatigue tests were performed under constant amplitude loading at stress ratios of  $R = -1.0, 0.1$  and  $0.4$ . The variable amplitude testing was conducted under the two different load histories (LH1 and LH2) previously outlined in Section 4.1. A log-log plot of the test data is presented in Figure 5.1, and compared with the AASHTO design S-N curve for Detail Category C, which is representative of the non-load carrying welded transverse stiffener tested in this study.

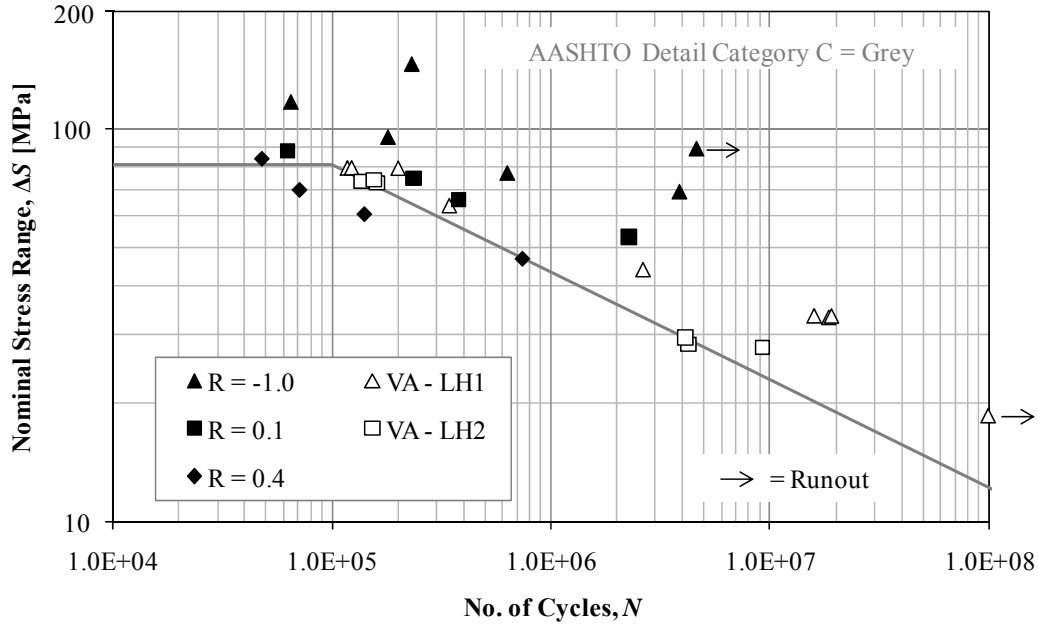


Figure 5.1: Fatigue test data compared with AASHTO design S-N curve for Detail Category C

The constant amplitude test results for stress ratios of  $R = 0.1$  and  $0.4$  show limited scatter and can each be represented by a single straight line on the S-N curve. Noticeable scatter is apparent for the constant amplitude test results for a stress ratio of  $R = -1.0$ . The AASHTO Detail Category C design curve remains conservative for both the  $R = -1.0$  and  $0.1$  test data, but is unconservative when compared with the test results at a stress ratio of  $R = 0.4$ . The test data suggests a slightly shallower slope than that of AASHTO Detail Category C, but the limited small-scale test data presented here is not sufficient to provide recommendations for a change in slope.

The test results for variable amplitude loading are plotted using an equivalent stress range as calculated previously in equation (2.4). The variable amplitude test data at higher stress ranges (ie.  $\Delta S = 75$  MPa) shows limited scatter and little difference between the two different load histories. The variable amplitude test data in the high cycle regime ( $\Delta S = 30$  MPa) shows scatter in the data and differences in fatigue life, between the two load histories tested. Test results under load history one (LH1) are very consistent, and with fatigue lives reaching 20 million cycles, could warrant the use of a second slope on the design S-N curve. However, the test results under load history two (LH2) exhibit some scatter and fall very closely with the AASHTO Detail Category C design curve. In general, the AASHTO design curve remains a conservative estimate of fatigue life as compared to the variable amplitude test data.

A comparison of test data from this study, with the results of tests conducted previously by Menzemer [1992], is shown in Figure 5.2, for constant amplitude loading conditions.

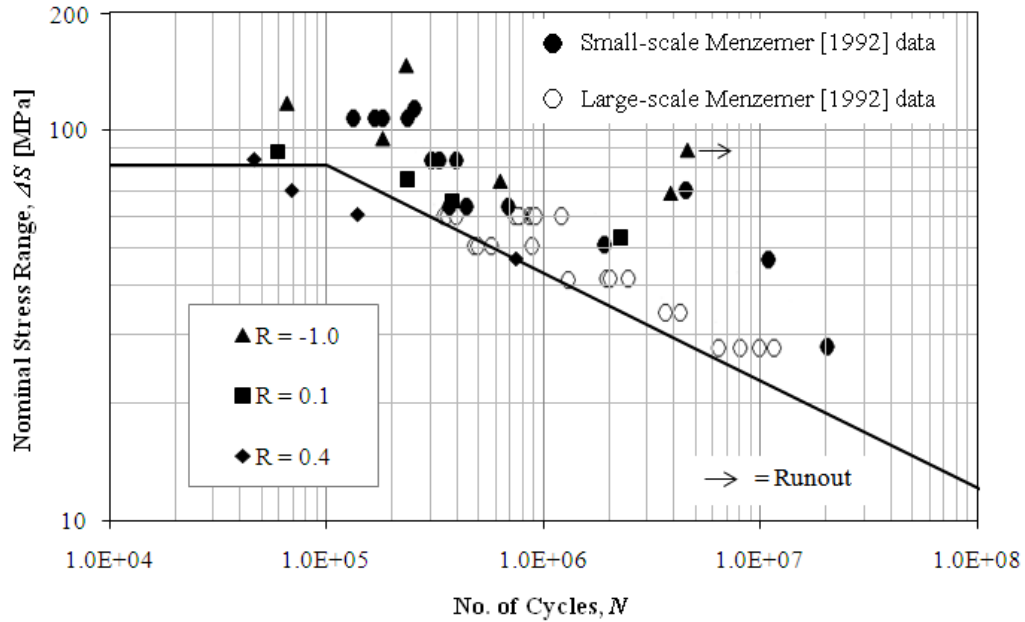
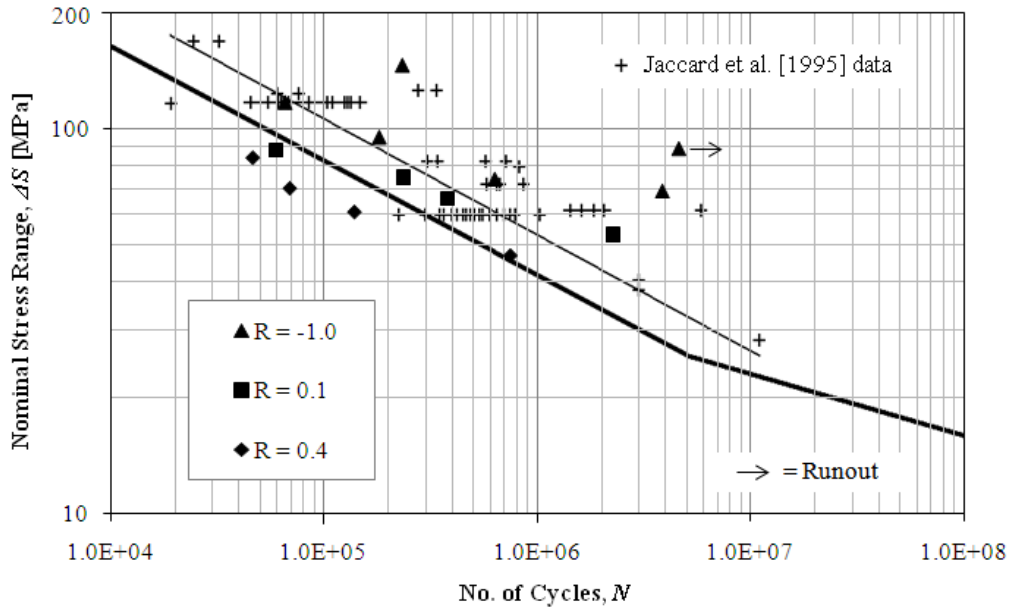


Figure 5.2: CA fatigue data compared with Menzemer [1992] data

All testing by Menzemer [1992] was conducted under constant amplitude loading at an  $R$ -ratio of 0.1 for both small- and large-scale specimens. Test data from this study for  $R = 0.1$  matches closely with the [Menzemer 1992] data, but plots on the low side of small-scale test data. The specimens used by Menzemer had a lower yield strength than the specimens tested in this study, thus not representative of this trend. In [Menzemer 1992], the difference between the mean resistance for small- and large-scale test data is seen to increase as fatigue life increases.

A comparison of the test data from this study, with the results of tests conducted by Jaccard *et al.* [1995], is shown in Figure 5.3, for constant amplitude loading conditions.



**Figure 5.3: CA fatigue data compared with ERAAS data [Jaccard *et al.* 1995]**

All testing by Jaccard *et al.* [1995] was conducted under constant amplitude loading at  $R$ -ratios of 0.1 and -1.0, mainly using large-scale specimens. The thin line represents the mean of the test data and the thick line represents the ERAAS design curve for Detail Category E1, which is representative of a non-load carrying transverse stiffener. The test data from the current study for  $R = 0.1$  and -1.0, generally lies within the range of the [Jaccard *et al.* 1995] data. The mean of the test data for the [Jaccard *et al.* 1995] data goes through the  $R = 0.1$  data from this study.

### 5.1.2 Crack Shape Measurements

Crack shape measurements were taken for all fatigue specimens tested according to the procedure outlined in Section 4.1.3. Of the 31 fatigue tests conducted, 11 specimens were classified as “good”, 8 “satisfactory”, and 12 “not satisfactory”. For the 19 specimens categorized as “good” or “satisfactory”, measurements of the crack shape were taken and the crack shape ratio calculated (Figure 5.4).

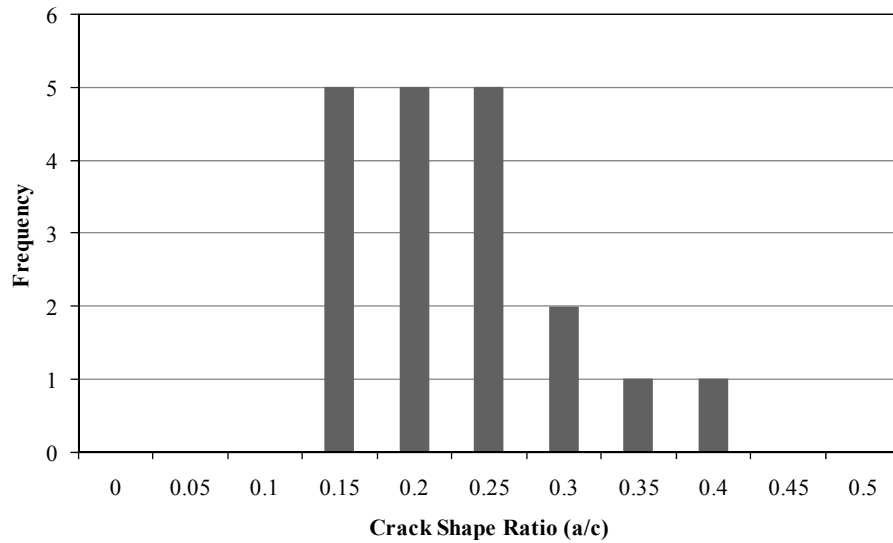


**Figure 5.4: Crack shape ratio histogram**

The mean crack shape ratio of the 19 specimens measured was 0.207 with a standard deviation of 0.067. Maximum and minimum crack shape ratios measured were 0.366 and 0.133, respectively. When considering only the 11 “good” specimens, a mean crack shape ratio of  $0.228 \pm 0.67$  was found. An empirical equation relating the crack depth and width have been formulated by Menzemer [1992] for stiffener details, as outlined in Section 2.7.3. Based on the crack depths measured in this study, the crack shape ratios were calculated using the above relationship and compared to the measured crack shapes (Figure 5.5).

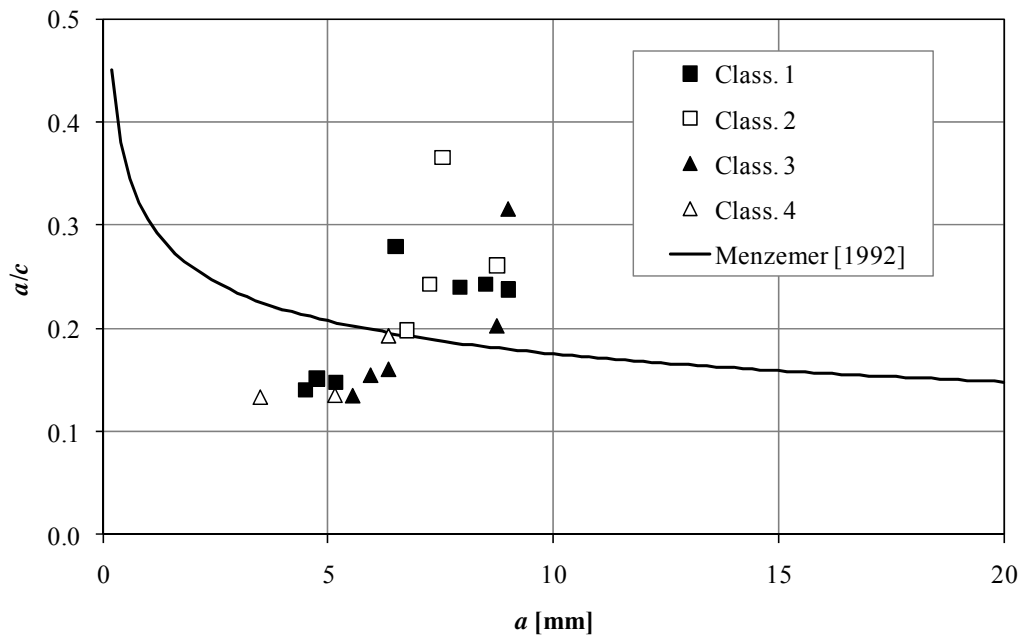


Figure 5.5: Crack shape measurements versus Menzemer [1992] relationship

The crack shape measurements performed for this study suggest an increase in the crack shape,  $a/c$ , with an increase in crack depth,  $a$ , in contrast to the relationship proposed by Menzemer [1992]; although, with such large scatter in the data it is difficult to compare the two. It was found that lower crack shape ratios calculated originated from specimens tested at higher stress ranges, and the opposite effect was also apparent for high crack shape ratios. Also, measurements were only taken for crack depths between approximately 3.0 and 9.0 mm, not accounting for the critical change in crack shape below 3.0 mm. Large variability in the crack shape measurements is apparent, especially as the crack depth increases.

## 5.2 Static Tensile Material Testing

Tensile materials test specimens were fabricated using 6061-T651 aluminum with the geometry described in Section 4.2. Using an axial tensile testing machine, tensile loads were applied to all five specimens until failure. The recorded axial loads and displacements were used to generate stress versus strain plots from which specific mechanical properties of aluminum could be established.



## 5.2.1 Test Results and Interpretation

Five specimens were tested under tensile loading; three consisting of “as-received” 6061-T651 aluminum alloy and two having undergone a full annealing process resulting in 6061-O aluminum. By testing annealed specimens, material properties can be determined and used to simulate the mechanical properties in the heat-affected zone. Measurements of specimen width, thickness, and gauge length obtained prior to testing are shown in Table 5.1.

**Table 5.1: Tensile specimen dimensions before testing and after failure**

Test	Material	Dimensions before Testing [mm]				Dimensions after Failure [mm]			
		Width (W <sub>o</sub> )	Thickness (T <sub>o</sub> )	Gauge Length (L <sub>o</sub> )	Area [mm <sup>2</sup> ] (A <sub>o</sub> )	Width (W <sub>f</sub> )	Thickness (T <sub>f</sub> )	Gauge Length (L <sub>f</sub> )	Area [mm <sup>2</sup> ] (A <sub>f</sub> )
1	6061-T651	12.73	9.75	50.70	124.12	10.50	6.96	61.00	73.08
2	6061-T651	12.73	9.68	50.70	123.23	10.61	6.95	59.82	73.74
3	6061-T651	12.72	9.78	50.70	124.40	10.65	6.44	60.94	68.59
4	6061-O	12.72	9.76	50.70	124.15	9.82	5.81	69.18	57.05
5	6061-O	12.71	9.75	50.70	123.92	9.30	5.32	70.35	49.48

After failure, it is apparent the cross-sectional dimensions of the specimens decrease and an increase in gauge length (extensometer initially 50.7 mm) is evidence of specimen elongation. The gauge length after failure was obtained through measurement by hand, whereas the failure displacement, noted in Table 5.2, was determined from the extensometer. It is apparent from the measurements, that the annealed (6061-O) specimens elongated approximately 10 mm more than the as-received (6061-T651) aluminum. Based on the axial load and displacement data, the yield and ultimate points were identified for each test (Table 5.2).

**Table 5.2: Description of load-displacement data**

Test	Material	Yield Load [kN]	Yield Disp. [mm]	Max Load [kN]	Failure Disp. [mm]
1	6061-T651	24.4	0.141	38.4	9.622
2	6061-T651	31.9	0.187	38.0	9.290
3	6061-T651	28.4	0.166	38.4	9.463
4	6061-O	7.3	0.146	14.7	17.649
5	6061-O	7.8	0.158	14.8	18.335

In Table 5.2, the yield load of the as-received aluminum specimens is significantly higher than that of the annealed specimens, as is the maximum load. Although, the yield and ultimate loads are lower for the annealed aluminum, its failure displacement is twice that of the as-received aluminum. Based on the specimen area and gauge length, as measured prior to testing, the engineering stress and strain

were determined for all specimens. Figure 5.6 shows the stress versus strain relationships for all of the as-received 6061-T651 aluminum specimens.

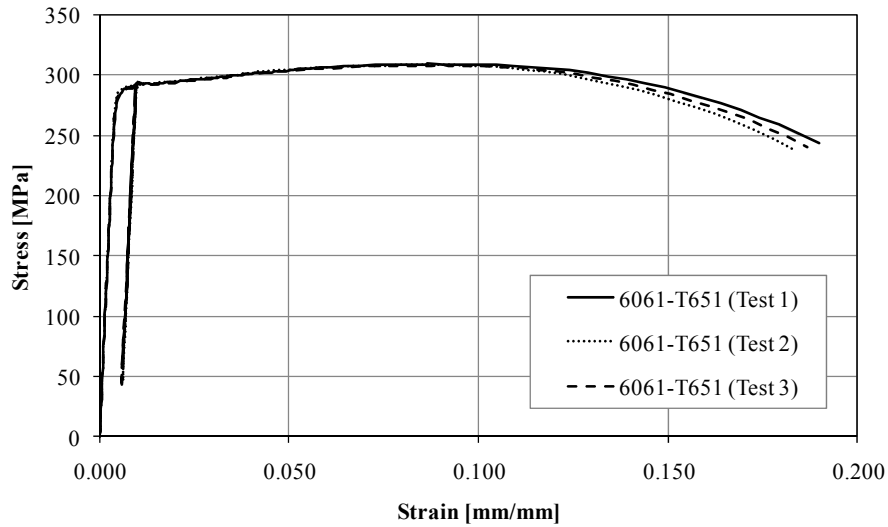


**Figure 5.6: Engineering stress vs. strain for as-received 6061-T651 aluminum**

All of the tests for as-received aluminum show very similar behaviour up to the ultimate strength. At the onset of necking, the behaviour to failure varies slightly between the three specimens, but in general, remains very similar. Figure 5.7 provides similar stress versus strain relationship, for the two annealed 6061-O aluminum specimens.

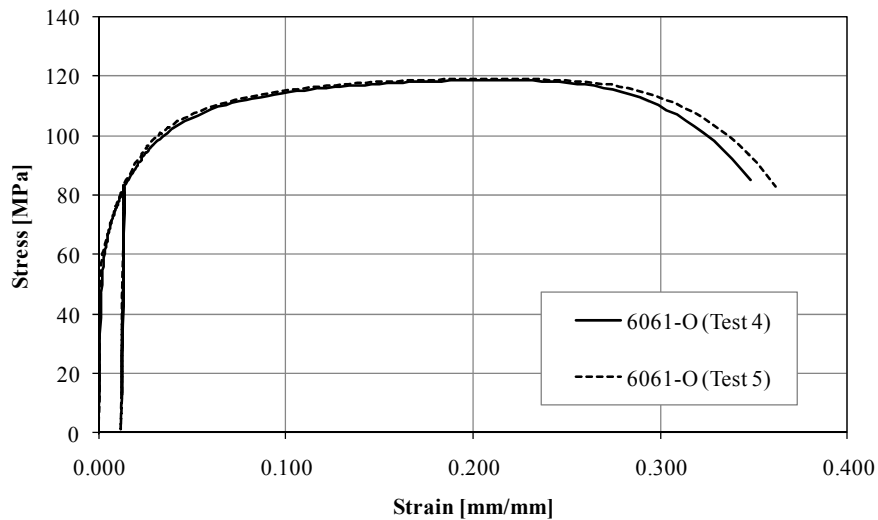


**Figure 5.7: Engineering stress vs. strain for annealed 6061-O aluminum**

Similarly to the as-received aluminum, the behaviour of the annealed specimens remains very similar to the onset of necking, after which the behaviour to failure deviates slightly. Figure 5.8 provides a comparison of the stress and strain relationship between the as-received and annealed aluminum specimens.

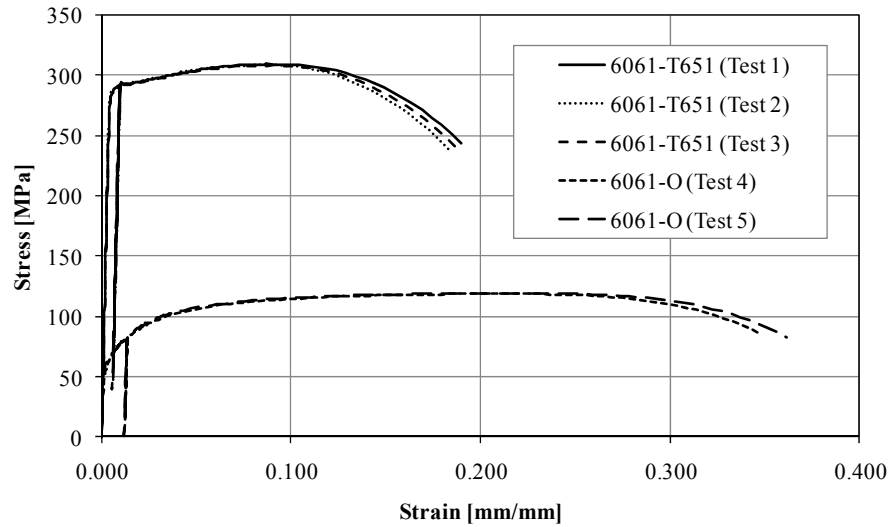


**Figure 5.8: Engineering stress vs. strain for 6061-T651 and 6061-O aluminum**

The difference in the yield and ultimate strengths between the two different specimen types is clear. The yield and ultimate strength for the as-received aluminum specimens is considerable higher than for the annealed specimens. Although the process of annealing has decreased the strength of the aluminum alloy significantly, the ductility has increased substantially. The yield point is clearly defined for the as-received aluminum specimens, but for the annealed specimens this is not the case; thus, the 0.2% rule was used to determine the yield stress. Based on the stress and strain behaviour above, the mechanical properties of both aluminum alloys tested were determined (Table 5.3).

**Table 5.3: Aluminum alloy mechanical properties**

Test	Material	Elastic Modulus (E) [MPa]	Yield Stress ( $f_y$ ) [MPa]	Ultimate Stress ( $f_u$ ) [MPa]
1	6061-T651	70776	287.29	309.46
2	6061-T651	70655	288.38	308.64
3	6061-T651	69923	286.74	308.40
4	6061-O	64778	58.95	118.80
5	6061-O	57095	62.81	119.29

As mentioned previously, the removal of cold working effects by the annealing process is evident in the mechanical properties calculated in Table 5.3. A significant reduction in the yield and ultimate stress is apparent for the annealed specimens in comparison to the as-received aluminum. The softening induced by the heat treatment of the annealing process also causes a slight reduction in the modulus of elasticity of the 6061-O aluminum in comparison to the 6061-T651 aluminum. Table 5.4 provides additional mechanical properties calculated based on the tensile testing data.

**Table 5.4: Aluminum alloy mechanical properties**

Test	Material	Ductility [% EL]	Ductility [% RA]	Toughness [J/m <sup>3</sup> ]	Resilience Modulus (U <sub>r</sub> ) [J/m <sup>3</sup> ]
1	6061-T651	20.32	41.12	5.52E+07	1.17E+06
2	6061-T651	17.99	40.16	5.29E+07	1.17E+06
3	6061-T651	20.20	44.87	5.41E+07	1.11E+06
4	6061-O	36.45	54.04	3.81E+07	1.24E+05
5	6061-O	38.76	60.08	3.99E+07	1.64E+05

The data shows the increase in ductility obtained by the annealing process. The elongation (%EL) of the 6061-O aluminum is significantly higher than that of the 6061-T651 aluminum. The annealed aluminum also shows a reduction in section toughness and resilience modulus as compared to the as-received aluminum alloy. Figure 5.9 shows failed samples of both aluminum types.

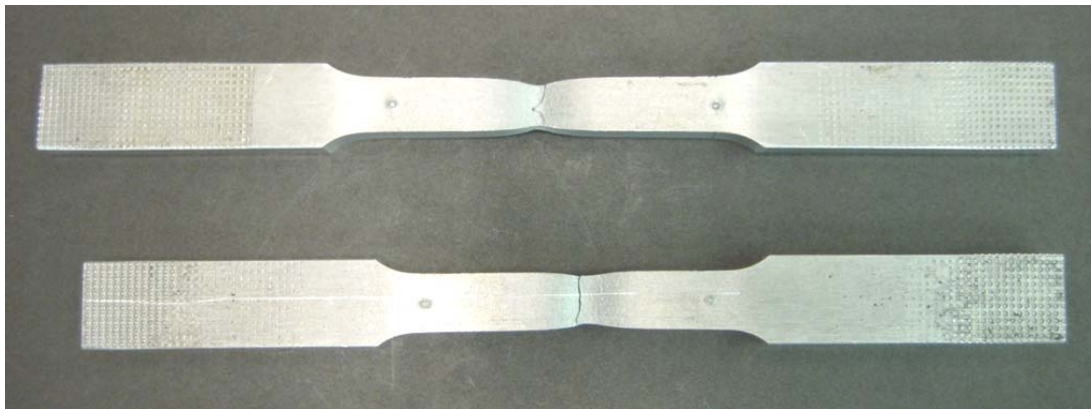


**Figure 5.9: Failure of 6061-T651 (bottom) and 6061-O (top)**

As shown in Figure 5.9, necking is apparent in both specimens; especially in the annealed specimen. The pronounced necking and increase in elongation of the 6061-O specimen is a result of an increase in ductility caused by the annealing process. The increase in ductility of the annealed specimen versus the as-received specimen is also apparent in the failure surface (Figure 5.10).

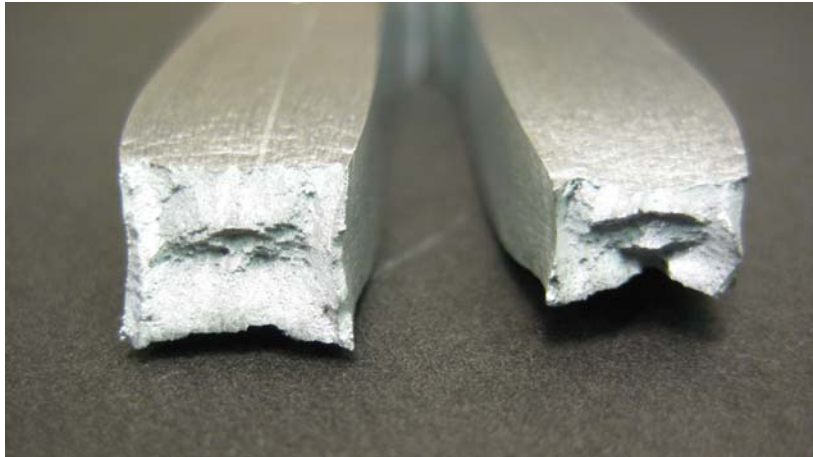


**Figure 5.10: Failure surfaces of 6061-T651 (left) and 6061-O (right)**

The failure surface of the 6061-T651 aluminum alloy shows a ductile failure but the failure surface is not as rough as the 6061-O specimen. The difference in cross-sectional area is significant. Due to the increased elongation and plastic deformation of the annealed aluminum specimen, the cross-sectional area is somewhat reduced in comparison to the as-received specimen.

### **5.3 Cyclic Testing**

The cyclic test specimens were fabricated from 6061-T651 aluminum plate with the geometry described in Section 4.3. Two specimens were tested – one “as-received” and one “annealed”. Cyclic loads were applied axially to both specimens under strain control and repeated until the hysteresis loop stabilizes or specimen failure occurred. Axial load and strain data were obtained and used to generate stress versus strain plots to fit the material behaviour to a Ramberg-Osgood material model.

Measurements of each specimen’s cross-sectional area were taken prior to testing, and both were found to have a diameter of 5.08 mm and a cross-sectional area of 20.268 mm<sup>2</sup>. For a duration of 10 cycles, multiple load and strain readings were recorded for each level of strain tested (ie. from 0.1%  $\epsilon$  to 1.0%  $\epsilon$ ). For analysis, the average maximum and minimum, load and strain readings for each level of strain were used to determine the engineering stress and strain at each strain level. The Ramberg-Osgood relationship models the plastic stress and strain in a material, thus the true and plastic stress and strains could be calculated based on the engineering stress determined from testing as shown below,

$$\sigma_{true} = \sigma_{eng} \cdot (1 + \epsilon_{eng}) \quad (5.1)$$

$$\varepsilon_{true} = \ln(1 + \varepsilon_{eng}) \quad (5.2)$$

$$\varepsilon_p = \frac{(\varepsilon_{true} - \sigma_{true})}{E} \quad (5.3)$$

### 5.3.1 Test Results and Interpretation

A comparison of the total engineering strain recorded from the test and the calculated plastic strain is provided in Figure 5.11.

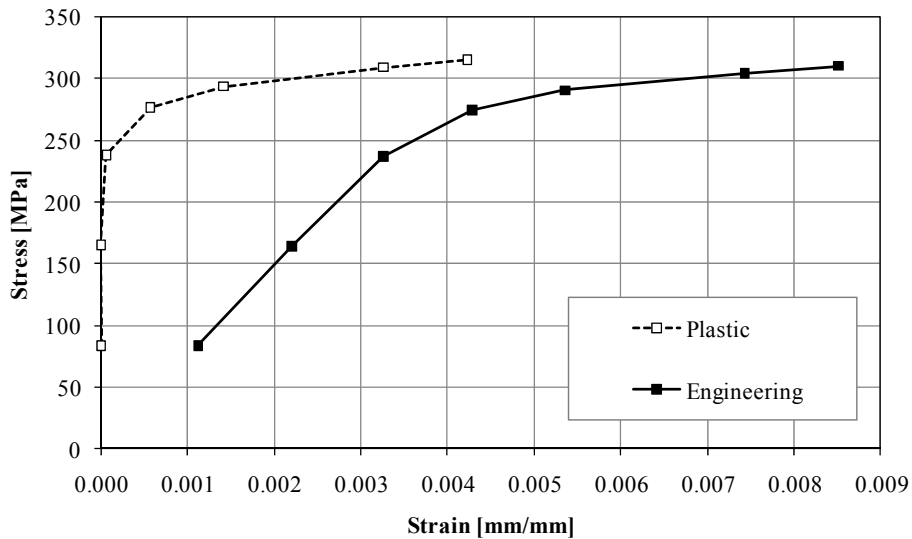
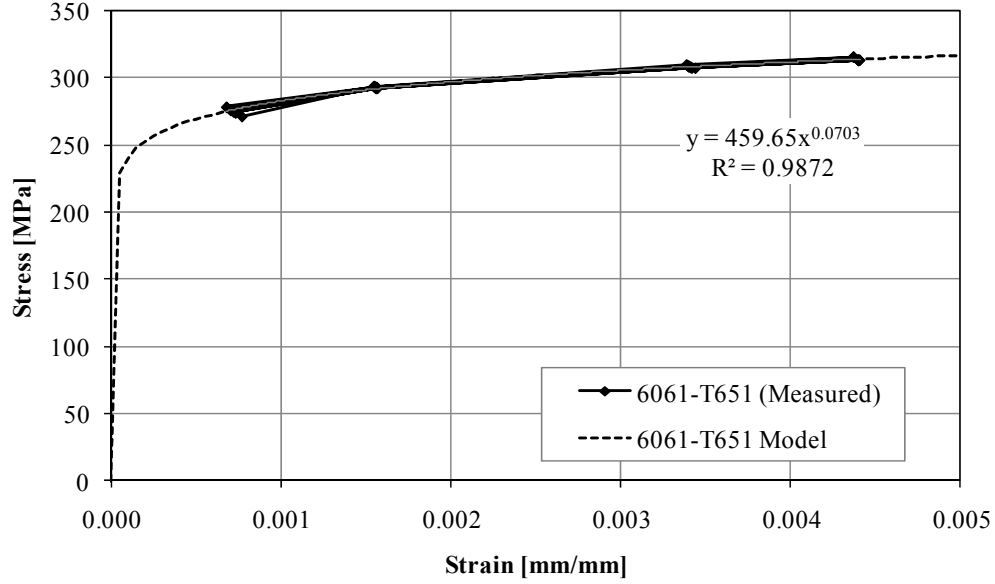


Figure 5.11: Total engineering & plastic strain for 6061-T651 aluminum

For the 6061-T651 aluminum specimen, the strain cycles were varied between  $\pm 0.1\% \varepsilon$  and  $\pm 1.0\% \varepsilon$  a total of 13 times before specimen failure. The strain measurements stabilized on the third series of readings, thus the first two series of data are excluded from the analysis. The final series of data is also excluded from the analysis as failure occurred during the 13<sup>th</sup> series of readings. A line of best fit is applied to the 6061-T651 test data using a power law to determine the cyclic material constants (Figure 5.12).



**Figure 5.12: Cyclic test data for 6061-T651 aluminum**

The power law fit to the data provided a regression coefficient,  $R^2$ , of 0.987, indicating a good fit of the cyclic test data. The data plotted in Figure 5.12 represents the plastic strain component of the data only, thus the power law of the best fit line can be correlated to the plastic strain component,  $\varepsilon_p$ , by rearranging the Ramberg-Osgood material model,

$$\varepsilon_p = \left( \frac{\sigma}{K'} \right)^{1/n'} \approx \sigma = K' \cdot \varepsilon_p^{n'} \approx y = 459.65 \cdot x^{0.0703} \quad (5.4)$$

thus,

$$K'_{6061-T651} = 459.65 \quad (5.5)$$

$$n'_{6061-T651} = 0.0703 \quad (5.6)$$

Similarly, for the 6061-O aluminum specimen, the strain was varied between  $\pm 0.1\% \varepsilon$  and  $\pm 1.0\% \varepsilon$  a total of 7 times before specimen failure. The strain measurements stabilized on the second series of readings, thus the first series of data is excluded from the analysis. The final series of data is also excluded from the analysis as failure occurred during the 7<sup>th</sup> series of readings. A line of best fit was again applied to the 6061-O test data using a power law to determine the cyclic material constants (Figure 5.13).

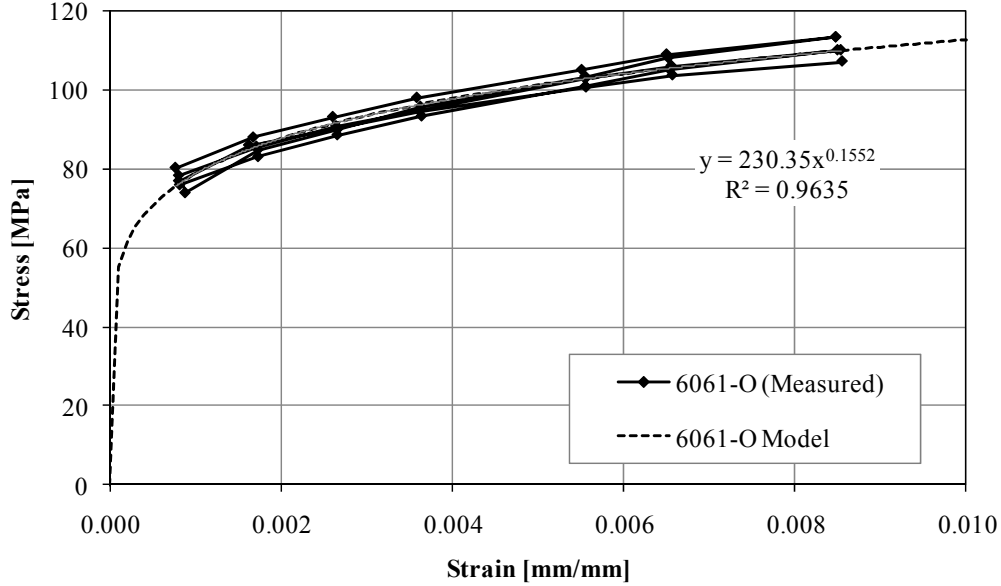


Figure 5.13: Cyclic test data for 6061-O aluminum

The power law fit to the data provided a regression coefficient,  $R^2$ , of 0.964, indicating a good fit of the cyclic test data. The data plotted in Figure 5.13 represents the plastic strain component of the data only, thus the cyclic material constants are determined again by re-arranging the Ramberg-Osgood material model as shown above, which results in,

$$K'_{6061-O} = 230.35 \quad (5.7)$$

$$n'_{6061-O} = 0.1552 \quad (5.8)$$

## 5.4 Microhardness Testing

Microhardness test specimens were fabricated using existing 6061-T651 aluminum fatigue specimens and 6061-O tensile specimens, as outlined in Section 4.4. Microhardness measurements were taken from as-received base metal, weld metal, HAZ metal, and annealed metal. The objective of the hardness tests was to facilitate estimation of the material properties in the HAZ using the material properties previously determined for 6061-T651 and 6061-O aluminum.

### 5.4.1 Test Results and Interpretation

Vickers hardness can be calculated using the following expression,



$$HVN = \frac{1854.4 \cdot F}{d^2} \quad (5.9)$$

where,  $HVN$  is the Vickers hardness,  $F$  is the load applied by the indenter in grams (g), and  $d$  is the average pyramid diagonal length in micrometres ( $\mu\text{m}$ ) [ASTM 2003]. The pyramid diagonal length was determined using the ImagePro 6.3 software, by taking measurements from photos of the indentation sites using a microscope as shown in Figure 5.14.

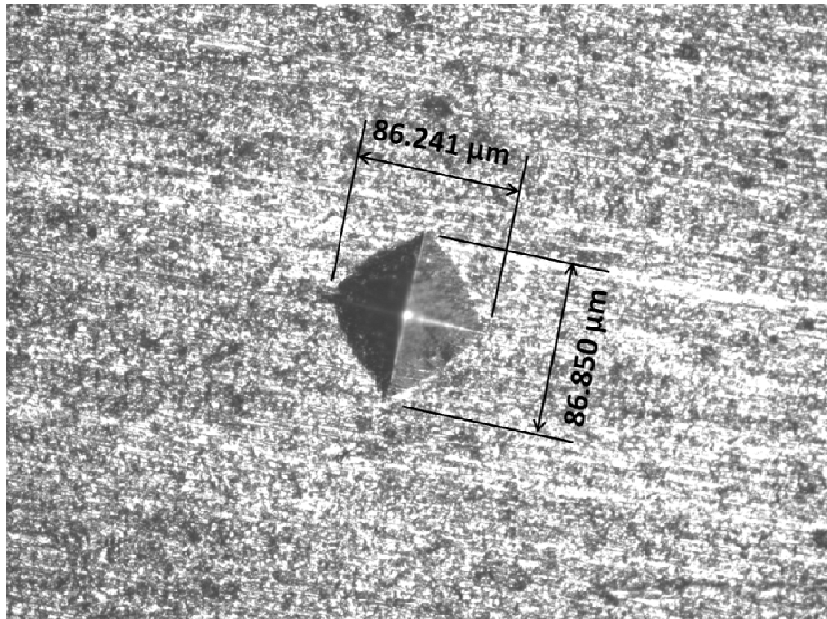


**Figure 5.14: Vickers hardness pyramid diagonal length measurements**

Vickers hardness readings were taken at 10 locations across the 9.5 mm thickness for as-received base metal (BM) and annealed (AM) specimens (Figure 5.15).

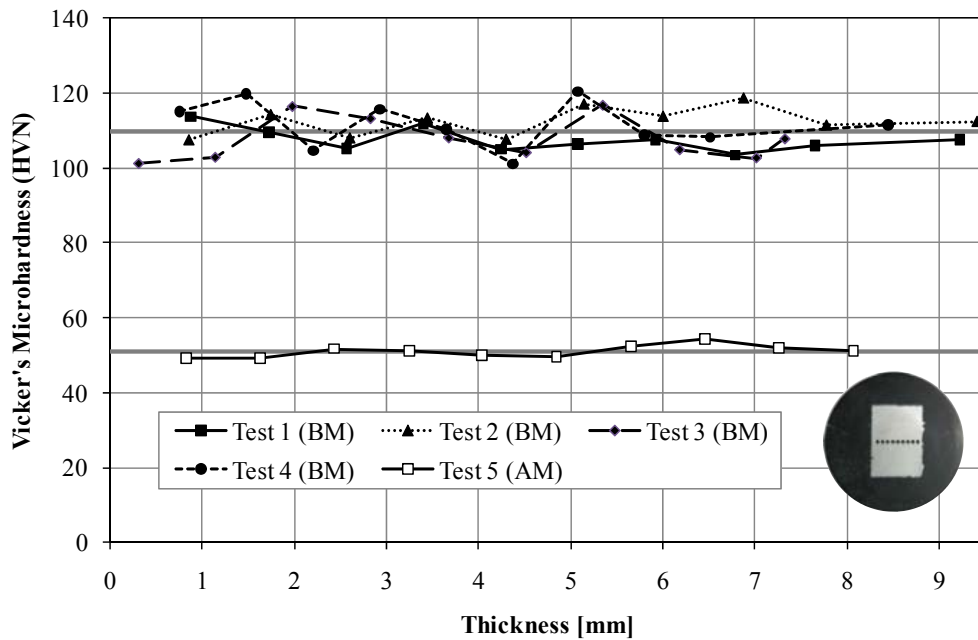


**Figure 5.15: Vickers hardness measurements for BM & AM**

In Figure 5.15, the grey lines are representative of an average Vickers hardness of 110 and 51, for the as-received and annealed aluminum, respectively. The lower hardness measurements for the annealed specimens are consistent with the expected softening effect from the annealing process. In general, for both base metal and annealed metal, the hardness readings across the thickness of the specimens, remained fairly consistent, in particular for the annealed specimens. It is expected that the variability in the hardness readings may be due in part to variations in the polishing process.

Vickers hardness readings were also taken for WM-HAZ specimens at multiple locations along a cross-section in the vicinity of the weld, including both weld metal and 6061-T651 base metal in the heat-affected zone (Figure 5.16).

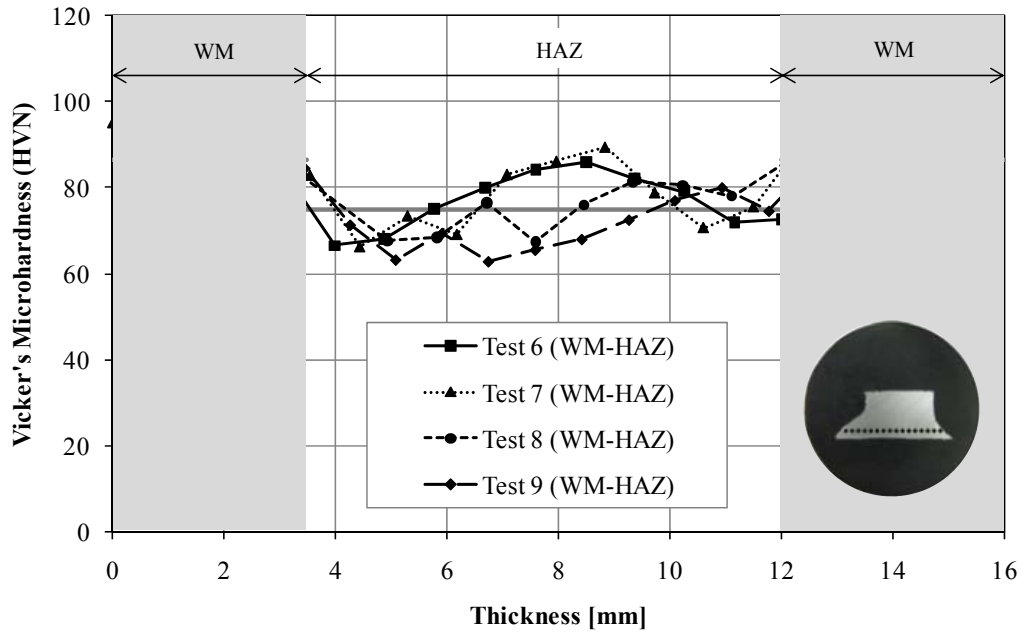


**Figure 5.16: Vickers hardness measurements for WM & HAZ**

The light grey regions of Figure 5.16 denote the hardness readings taken for the weld metal. The grey lines are representative of an average Vickers hardness of 87 and 75, for the weld metal and base metal in the heat-affected zone, respectively. A trend of decreasing hardness is apparent in the transition from the weld metal to the HAZ. Tests 6 and 7 exhibit a decrease in hardness, as the distance to the weld decreases; but, in general, this trend cannot be confirmed due to the high variability in the data. The increased variability in results is a distinct difference between the hardness readings taken in the base metal and in the vicinity of the weld.

A summary of the hardness data for all four materials is presented in Table 5.5.

**Table 5.5: Vickers hardness results summary**

Material	Vickers Hardness (HV/N)			
	AVG	MAX	MIN	Range
BM	109.8	120.4	101.0	19.4
AM	51.0	54.3	49.2	5.1
WM	86.6	99.4	69.9	29.5
HAZ	74.8	89.5	62.9	26.6

In addition to average hardness measurements, maximum and minimum hardness measurements are provided to give an indication of the variability in readings. Hardness results show that the base metal

and annealed metal provide upper and lower bounds of the hardness measurements recorded in the vicinity of the weld, respectively. In the heat-affected zone, the hardness readings fall within bounds set from the base and annealed specimens, which may facilitate an estimate of the mechanical properties in the HAZ in relation to those of the 6061-T651 and 6061-O aluminum.

## 5.5 Residual Stress Testing

Residual stress testing was conducted using an un-tested fatigue specimen by Proto Manufacturing Limited. A non-destructive x-ray diffraction technique, discussed in Section 4.5, was used to take the residual stress measurements.

### 5.5.1 Test Results and Interpretation

The fatigue test specimen was first prepared for residual stress measurements at two test locations, longitudinally along the plate at both weld toes as shown in Figure 5.17.

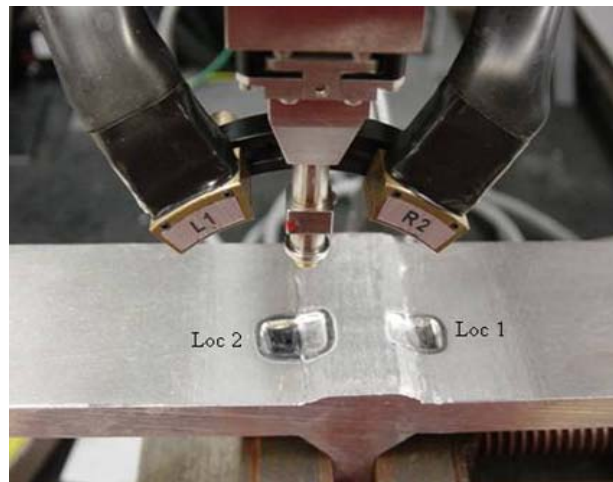


Figure 5.17: Residual stress measurement locations [Proto 2010]

Residual stress measurements were taken at both weld toes at varied depths between 0 and 1.5 mm (Figure 5.18).

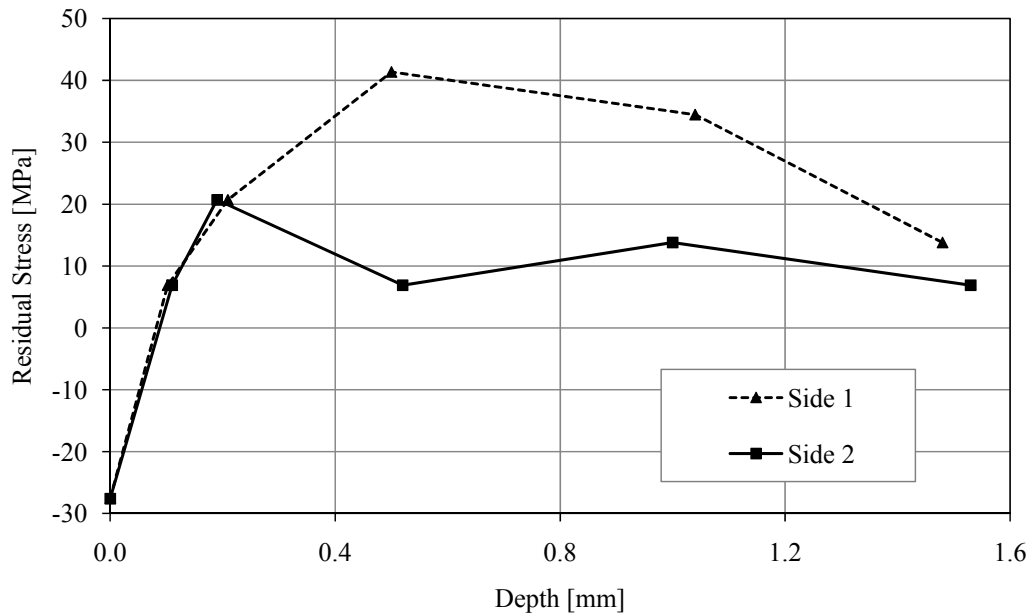


Figure 5.18: Residual stress measurements at weld toe [Proto 2010]

The residual stresses at the weld toes for the fatigue specimen were lower than expected, and even slightly compressive at the surface. The maximum residual stress at a depth of 0.5 mm is  $41 \pm 7$  MPa, which is 14.4% of 6061-T651 aluminum base metal yield strength (Table 5.6).

Table 5.6: Residual stress test results

Side 1			
Depth (mm)	Residual Stress (MPa)	Gradient Corrected (MPa)	Gradient and Depth Corrected (MPa)
0.00	-21 ± 0	-28 ± 0	-28 ± 0
0.10	+14 ± 7	+7 ± 7	+7 ± 7
0.21	+21 ± 7	+21 ± 7	+21 ± 7
0.50	+48 ± 7	+41 ± 7	+41 ± 7
1.04	+48 ± 14	+48 ± 14	+34 ± 14
1.48	+41 ± 14	+41 ± 14	+14 ± 14
Side 2			
Depth (mm)	Residual Stress (MPa)	Gradient Corrected (MPa)	Gradient and Depth Corrected (MPa)
0.00	-21 ± 7	-28 ± 7	-28 ± 7
0.11	+7 ± 7	+7 ± 7	+7 ± 7
0.19	+28 ± 7	+21 ± 7	+21 ± 7
0.52	+7 ± 14	+7 ± 14	+7 ± 14
1.00	+14 ± 14	+14 ± 14	+14 ± 14
1.53	+14 ± 14	+14 ± 14	+7 ± 14

The compressive stresses at the surface and very low residual stress measurements are of interest. The maximum residual stress measured for the fatigue specimen in this study is approximately 15% of the base metal yield strength. The residual stress measurements reported herein on small-scale specimens are considerably lower than tests by Menzemer [1992] and Kosteas [1978]. Testing by Menzemer [1992] concluded residual stresses in small- and large-scale specimens of 40-50% and 80% of the parent material yield strength, respectively. Testing of large-scale beams by Kosteas [1978] revealed the presence of residual stresses up to approximately 50% of the parent material strength, which is considerable lower than seen in the tests by Menzemer [1992]. The differences between the residual stress measurements in all cases suggest a high degree of variability in the residual stresses present in welded aluminum components.

## Chapter 6

### Fracture Mechanics Analysis

#### 6.1 Introduction

Fracture mechanics analysis has been a primary means, historically, for justifying the use of a reduced slope in the design S-N curve beyond the CAFL in some codes and recommendations. In Menzemer [1992], such a fracture mechanics analysis is presented. The results suggest that the S-N curves for VA loading conditions may have two slopes. However, the change in slope is seen to be diminished by periodic overload events. Results are presented in this chapter of a similar analysis performed with the specific purpose of examining the shape of the design S-N curve under simulated VA loading conditions due to North American highway traffic.

A linear elastic fracture mechanics (LEFM) model and the input parameters for the model are first discussed, including a sensitivity analysis to examine the assumed input parameters. Analysis results are then presented for the load histories used previously for fatigue testing, and were compared with fatigue test results from Section 5.1. The effects of overload events and use of other relevant loading histories are also investigated. A scale effect study is then conducted to predict fatigue lives of full-scale fatigue details.

In addition to the LEFM model, a strain based fracture mechanics (SBFM) model was considered for application to this problem. In Section 6.6, this model is described and sample analysis results generated with this model are presented and discussed.

#### 6.2 Linear Elastic Fracture Mechanics Model

The model assumes the presence an initial defect and simulates how the defect will grow over time, subject to various loading conditions. Modelling fatigue crack propagation based on an assumed initial defect is a valid assumption for welded components, as crack-like defects are quite certainly always present due to the effects of the welding process. Once validated with the available test data, fatigue life prediction can be conducted for other structural configurations and loading conditions.

The LEFM model discussed here has been previously used by Walbridge [2008], which notes use of the LEFM approached by others. The Paris-Erdogan crack growth law, modified to include crack closure effects and a threshold stress intensity factor (SIF) range,  $\Delta K_{th}$ , is used in this model to predict growth of an initial defect:

$$N = \int_{a_i}^{a_c} \frac{da}{C \cdot \min(\Delta K_{eff}^m - \Delta K_{th}^m, 0)} \quad (6.1)$$

where the fatigue life,  $N$ , of a component is determined by a numerical integration from the initial crack depth,  $a_i$ , to a critical crack depth,  $a_c$  and the effective stress intensity factor range,  $\Delta K_{eff}$ , is a function of crack closure effects:

$$\Delta K_{eff} = K_{max} - \max(K_{op}, K_{min}) \quad (6.2)$$

where  $K_{max}$  and  $K_{min}$  are the maximum and minimum stress intensity factors for the given load history, and  $K_{op}$  is the stress intensity factor corresponding with the load level at which the crack opens.

Figure 6.1 explains the  $\Delta K_{eff}$  and  $K_{op}$  concepts with respect to the loading cycle. In this figure, a crack closure SIF,  $K_{cl}$ , is also defined. In the current study, it is assumed that  $K_{op} = K_{cl}$ .

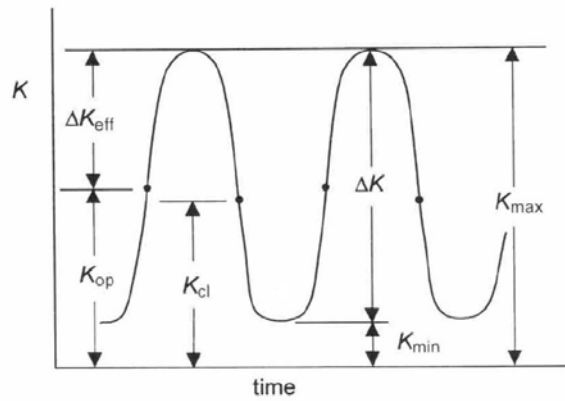


**Figure 6.1: Effective and opening stress intensity factor representation [Stephens *et al.* 2001]**

The stress intensity factor at the load level corresponding with crack closure,  $K_{op}$ , was determined using the formula proposed by Newman [1994], which requires the maximum stress,  $\sigma_{max}$ , the stress ratio,  $R$ , the flow stress,  $\sigma_o$  (which may be taken as the average of the material's yield strength,  $\sigma_y$ , and ultimate strength,  $\sigma_u$ ), and the plastic constraint factor,  $\mu$ . The plastic constraint factor is estimated based on [Wang *et al.* 2002], and has a value of 1.0 for plane stress and 3.0 for plane strain.

As suggested by McClung [1994], the model used herein replaces the  $\sigma_{max}/\sigma_o$  ratio with  $K_{max}/K_o$  where,

$$K_o = \sigma_o \cdot \sqrt{\pi \cdot a} \quad (6.3)$$



Under VA loading, the LEFM conservatively assumes that  $K_{op}$  for all cycles is equal to the minimum  $K_{op}$  under steady state (CA) loading for any of the cycles in the loading history.

The stress intensity factors are determined using elastic weight functions,  $m(b,a,c)$ , for semi-elliptical cracks in plate with a finite thickness, as proposed by Shen and Glinka [1991],

$$K = \int_0^a \sigma(b) \cdot m(b,a,c) \cdot dx \quad (6.4)$$

The weight functions account for the crack shape, finite plate thickness, non-uniform stress distribution, and the fact that the crack is a surface crack. In a linear elastic analysis, the rule of superposition applies and thus residual stresses,  $\sigma_{res}$ , and applied stress,  $\sigma_{app}$ , can be added to give  $\sigma(b)$  or the SIFs,  $K_{res}$  and  $K_{app}$  can be calculated separately and added after.

In conjunction with the LEFM model described above, knowledge of the elastic and residual stress distributions along the crack path are required for the weld detail analysed. A finite element analysis using ABAQUS was performed to determine the stresses near the notch of the weld toe. Along with the plate thickness basic assumptions were made for the weld toe angle,  $\theta_w$  ( $45^\circ$ ), and the weld toe radius,  $\rho$  (0.5 mm), for input in the finite element model. The finite element model generates an elastic stress concentration factor (SCF), which was formulated based on an axially loaded transverse stiffener detail, as shown in Figure 6.2. A first-in last-out (FILO) algorithm was used to identify cycles in the VA loading analysis.

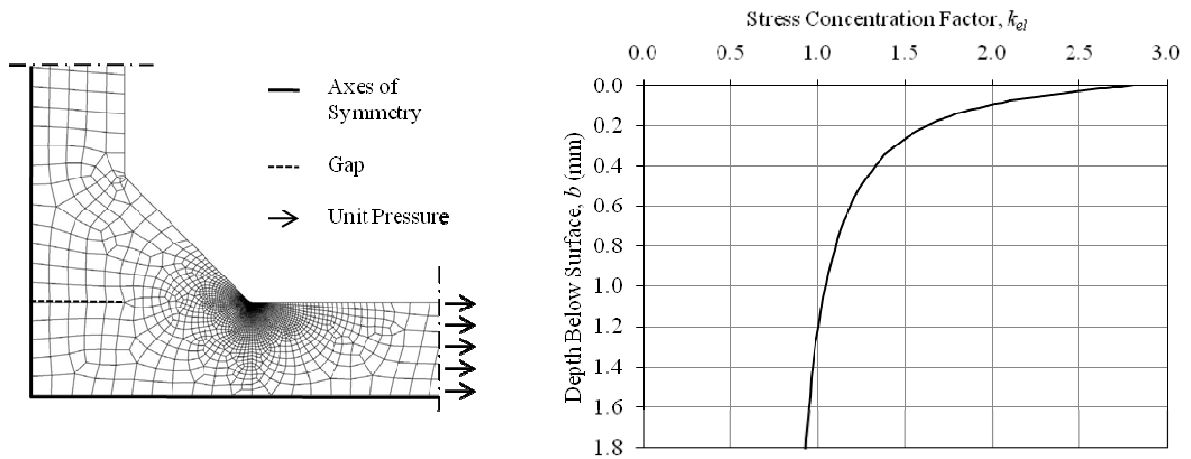


Figure 6.2: SCF determination: FE model of weld detail (left) and SCF distribution (right)

## 6.3 Fracture Mechanics Input Parameters

Based on the materials tests performed in this study and by others, assumptions for the input parameters used in the fracture mechanics analysis are outlined, including: material properties, initial crack depth, crack shape, residual stress, and crack growth data.

### 6.3.1 Material Properties

The static tensile coupon tests described in Section 5.2 provided mechanical properties for both as-received (6061-T651) and annealed (6061-O) aluminum alloys. The mechanical properties in the HAZ adjacent to the weld are most representative of the material behaviour near the fatigue crack, which are of greatest interest for the fracture mechanics analysis. Performing materials tests directly in the HAZ adjacent to the weld is rather difficult, thus the material properties for the HAZ were determined by indirect means. Specifically, the hardness results outlined in Section 5.4 were used to estimate the mechanical properties of the 6061 aluminum in the HAZ. Research by Baumel and Seeger [1990] provides an empirical relationship to predict the Ramberg-Osgood cyclic strength coefficient,  $K'$ , for steel and aluminum. Although a linear relationship between Vickers hardness and ultimate strength is provided in the same reference for steel, it is not for aluminum. Thus, with no available alternative, a similar linear relationship was generated to determine the ultimate strength in the HAZ, based on the measured Vickers hardness,  $HVN$ , and ultimate strength,  $\sigma_u$ , for 6061 aluminum in the as-received (T651) and annealed (O) states,

$$\sigma_{ult} = 3.2168 \cdot HVN + 45.006 \quad (6.5)$$

The cyclic strength coefficient,  $K'$ , was determined using the expression provided by Baumel and Seeger [1990] for aluminum,

$$K' = 1.61 \cdot \sigma_{ult} \quad (6.6)$$

The cyclic strain hardening exponent,  $n'$ , associated with equation (6.9) is 0.11. Estimation of the yield strength and modulus of elasticity based on material hardness was not available; thus, for simplicity, linear interpolation based on the hardness measurements was again used. The resulting mechanical properties used in the fracture mechanics analysis are presented in Table 6.1.

**Table 6.1: 6061-T651 aluminum material properties**

<b>Material Property</b>		<b>BM</b>	<b>HAZ</b>	<b>O</b>
Vickers Hardness	<i>HVN</i>	110	75	51
Modulus of Elasticity (MPa)	<i>E</i>	70451	64807	60937
Yield Strength (MPa)	$\sigma_y$	287.5	153.0	60.9
Ultimate Tensile Strength (MPa)	$\sigma_{ult}$	308.8	196.3	119.1
Cyclic Strain Hardening Exponent	<i>n'</i>	0.070	0.110	0.155
Cyclic Strength Coefficient (MPa)	<i>K'</i>	459.7	316.0	230.4

The properties of all three materials in Table 6.1 were used in the sensitivity analysis presented in Section 6.4. The material properties for the HAZ were taken as the expected values in this analysis.

### 6.3.2 Initial Crack Depth

Research conducted by Menzemer [1992], previously discussed in Section 2.7.3, provided over 100 measurements of initial defect sizes on welded aluminum components. These measurements suggest that the most common initial crack depth is 0.1 in (0.025 mm), which serves as the expected value in the current analytical study. It is assumed that the probability of an initial crack to be less than 0.025 mm is very low, thus an initial crack depth of 0.025 mm serves as a lower bound in the sensitivity analysis. A reasonable expected initial defect depth to assume for steel is 0.15 mm [Walbridge 2008]. Initial defect measurements observed by Menzemer [1992] were found up to 0.6 in (0.15 mm), thus an initial crack depth of 0.15 mm serves as an upper bound in the sensitivity analysis.

### 6.3.3 Crack Shape

Measurements of the crack shape in this study, previously discussed in Section 5.1, suggest the use of a constant crack shape ratio of 0.207. However, crack shape measurements were recorded for depths only as small as 3.0 mm, and thus do not consider the variations in the crack shape from the initial defect depth to the depths measured. Also discussed previously in Section 2.7.3, Menzemer [1992] formulated an empirical relationship of the crack shape based on the crack depth (see equation 2.10), which suggests a crack shape ratio of approximately 0.75 for an initial crack depth of 0.025mm, following an exponential relation to a crack shape ratio of approximately 0.2 at higher crack depths (see Figure 5.5). This relationship suggests that a constant crack shape ratio may not provide a representation of the actual crack growth. Thus, the crack shape relationship provided by Menzemer [1992] serves as the expected value in the sensitivity analysis.

### 6.3.4 Residual Stress

The residual stresses,  $\sigma_{res}$ , assumed in the analysis were chosen based on testing conducted in this study and elsewhere. Testing from this study, discussed previously in Section 5.5, suggest residual stresses of approximately 15% of the base metal yield strength are present at the weld toe, which serves here as the expected value in this analysis. Testing also shows that residual stresses can be as low as zero at the weld toe, thus zero serves as a lower bound in this study. Previous research conducted, quantifying residual stresses in welded aluminum components discussed in Section 2.7.4, suggests residual stresses in small-scale specimens to be in the order of 40 to 50% of the base metal yield strength and residual stresses in large-scale specimens to be in the order of 50 to 80% of the base metal yield strength. Therefore, a range of residual stress are analysed up to 80% of the base metal yield strength.

### 6.3.5 Crack Growth Parameters

For the fracture mechanics analysis of aluminum, many references indicate, that a multi-slope crack growth rate curve is appropriate. Eurocode 9 proposes a series of upper bound curves for wrought aluminum alloys. Since, for the model employed herein, the crack opening SIF is considered explicitly, an effective SIF versus crack growth rate curve was desired. Menzemer [1992] recommends that crack growth rate data obtained under constant  $K_{max}$  or high  $R$ -ratio conditions be used in this case. On this basis, a curve based on a combination of constant  $K_{max}$  conditions at low SIFs and  $R = 0.8$  at high SIFs was used herein. Rather than use the upper bound curve in Eurocode 9, a “best fit” curve was estimated graphically. This curve is shown in Figure 6.3.

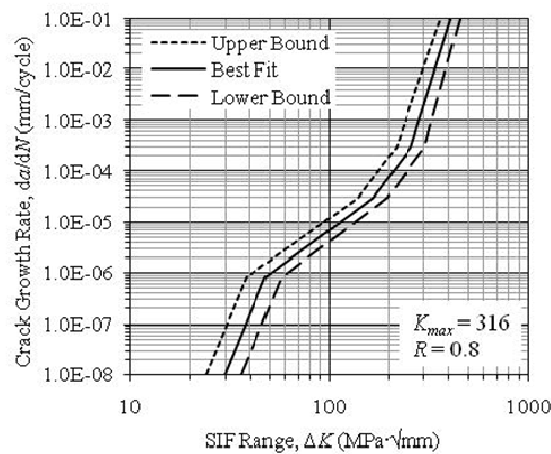


Figure 6.3: Crack growth rate curves based on Eurocode 9

In the sensitivity analysis, the best fit curves serve as the expected value and the lower and upper bound crack-growth curves serve as the upper and lower bounds, respectively.

## 6.4 Constant Amplitude and Sensitivity Analysis

LEFM analyses were first performed for the three  $R$ -ratios of 0.1, 0.4, and -1.0 tested under constant amplitude loading. The results produced using the LEFM model were compared to the fatigue tests conducted in this study to assess the accuracy of the model. A sensitivity analysis was then conducted to examine the impacts of separately varying different inputs parameters in relation to the expected values assumed. The results of the sensitivity analysis were compared to determine which inputs have a more significant effect on the results. Table 6.2 outlines the expected input values for the sensitivity analysis.

**Table 6.2: Sensitivity analysis expected values**

<b>Input</b>		<b>Expected Value</b>
Material properties	$E, \sigma_y, \sigma_{ult}, K', n'$	HAZ
Initial crack depth	$a_i$	0.025 mm
Crack shape	$a/c$	[Menzemer 1992] model
Residual stress	$\sigma_{res}$	$0.15 \cdot \sigma_y$
Crack growth curve	$da/dN \text{ v } \Delta K$	Best Fit

In all comparisons, the AASHTO Detail Category C curve is provided for reference in grey.

### *Material Properties*

The material properties from the HAZ, represent the expected values as the material properties in the vicinity of the weld define the fatigue life. The material properties of the base metal and annealed metal represent the upper and lower bounds assumed in the sensitivity analysis, respectively. Figure 6.4 provides a comparison for the assumed material properties under an  $R$ -ratio of 0.1 of the LEFM analysis results.

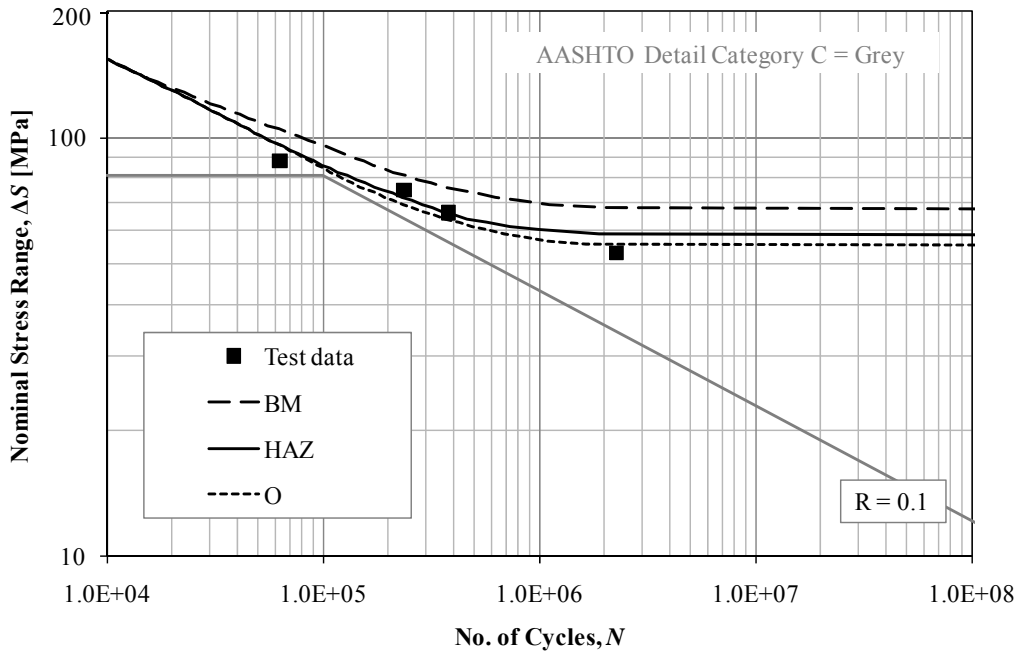


**Figure 6.4: Material properties comparison for  $R = 0.1$**

The material properties assumed for the HAZ fall within the bounds of the measured properties for the base (BM) and annealed (O) metals. The S-N results with the HAZ and O material properties assumed are very close and fit the test data well. The results were similar for the other CA loading cases using  $R$ -ratios of -1.0 and 0.4. On this basis, the HAZ material properties are assumed in the subsequent analysis.

#### *Initial Crack Depth*

Due to the limited availability of measured data, an initial crack depth of 0.025 mm was assumed to represent the expected value and lower bound in the analysis. An upper bound crack depth of 0.15 mm was assumed. A crack depth of 0.05 mm, used by Menzemer [1992], is also considered in the analysis to show the effect of varying this parameter on the analysis results. Figure 6.5 provides a comparison of the analysis results for the three initial crack depths.

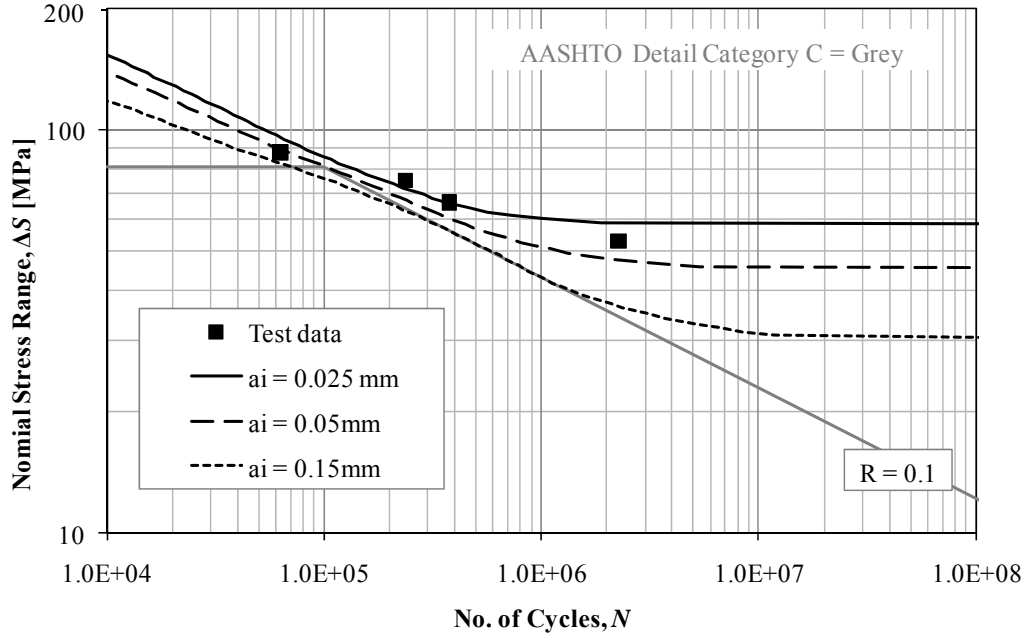
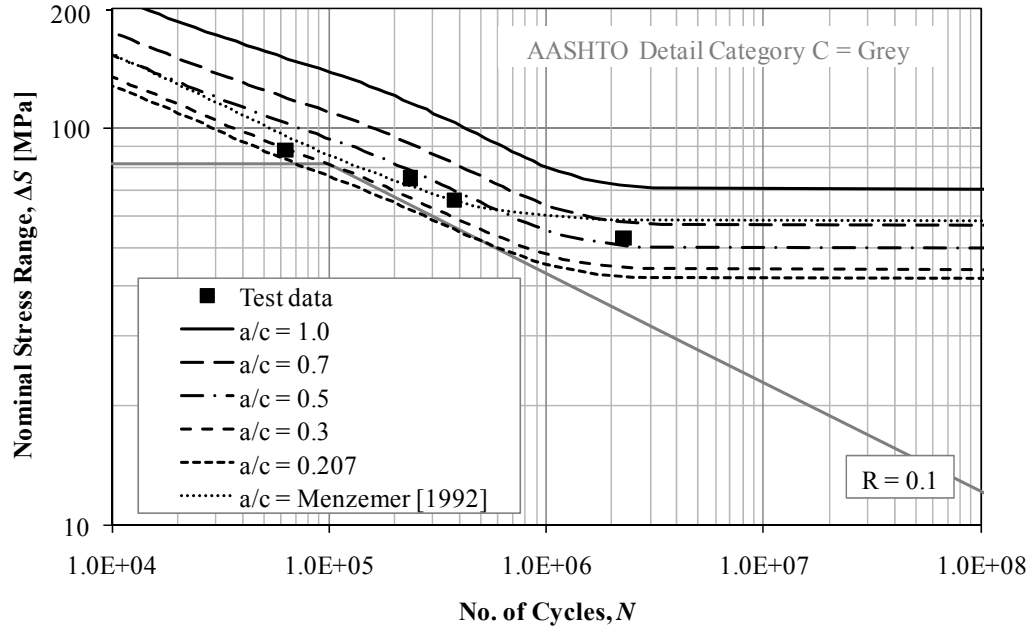


Figure 6.5: Initial crack depth comparison for  $R = 0.1$

Assumed initial crack depths of 0.025 mm and 0.05 mm both provide a good fit of the test data. A large majority of measurements taken in [Menzemer 1992] were for an initial crack depth of 0.025mm. Trends in the results remain consistent with the other  $R$ -ratios of -1.0 and 0.4 analysed. On this basis, an initial crack depth of 0.025 mm is assumed in the subsequent analysis.

#### Crack Shape

A comparison was conducted between results predicted using the empirical crack shape relationship proposed by Menzemer [1992], shown previously in equation (2.10), and results predicted using a constant crack shape ratio. Constant crack shape ratios ranging between 0.207 and 1.0 were assumed based on the measurements conducted in this study. This range also happens to bound the evolving crack shape determined by Menzemer's crack shape function. Figure 6.6 provides a comparison of the results for various assumed crack shape ratios.



**Figure 6.6: Crack shape ratio comparison for  $R = 0.1$**

The S-N curve in Figure 6.6 derived using the Menzemer relationship does not provide the best fit with the data as it appears to over-estimate the constant amplitude fatigue limit. The measured crack shape ratio of 0.207 provides a lower bound estimate of the fatigue life. These trends are consistent for other  $R$ -ratios of -1.0 and 0.4 analysed herein. A constant crack shape ratio in the range of 0.3 to 0.5 provides a good fit with the  $R = 0.1$  test data. A comparison with all  $R$ -ratios tested was conducted to establish a crack shape ratio that fits all the constant amplitude test data (see Figure 6.7).



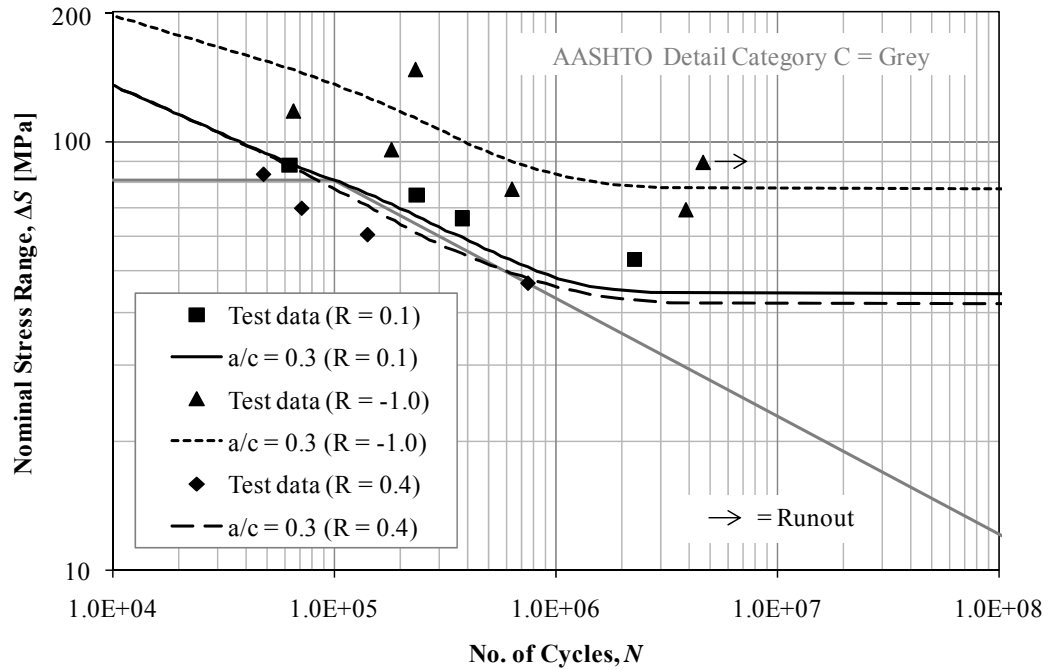
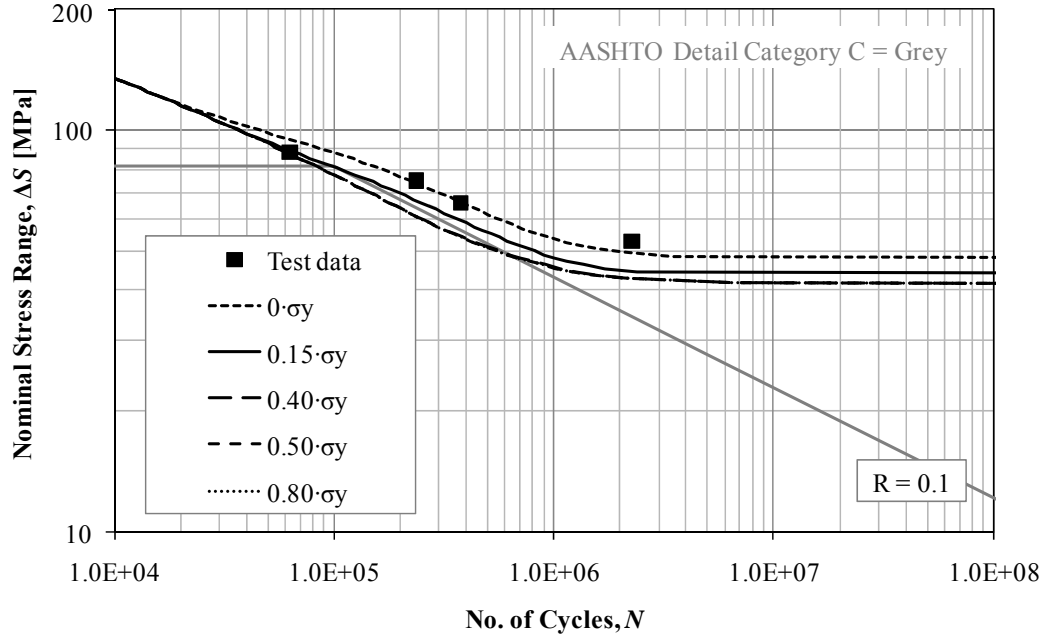


Figure 6.7: Crack shape ratio comparison for all  $R$ -ratios

Based on the comparison in Figure 6.7, it was determined that a crack shape ratio of 0.3 provides the best fit for the test data at all  $R$ -ratios. Thus, for the duration of the analysis a constant crack shape ratio of 0.3 is used.

#### *Residual Stress*

Based on the limited availability of data, residual stresses,  $\sigma_{res}$ , between zero and 80% of the base metal yield strength ( $0.8 \cdot \sigma_y$ ) were assumed. For this study, the expected residual stress is the measured value of  $0.15 \cdot \sigma_y$ . Various residual stress levels were investigated, including 40, 50, and 80% of the base metal yield strength. Figure 6.8 provides a comparison of the results predicted with the different assumed uniform stress levels for an  $R$ -ratio of 0.1.



**Figure 6.8: Residual stress comparison for  $R = 0.1$**

As expected the effects of the assumed tensile residual stress levels are minimal when considering an  $R$ -ratio of 0.1. Measured residual stresses in this study, as discussed previously in Section 5.5, lie in a range between zero and  $0.15 \cdot \sigma_y$ . The results within this range provide the best fit with the test data. In contrast, Figure 6.9 provides a comparison of the results obtained with the different residual stresses for an  $R$ -ratio of -1.0.

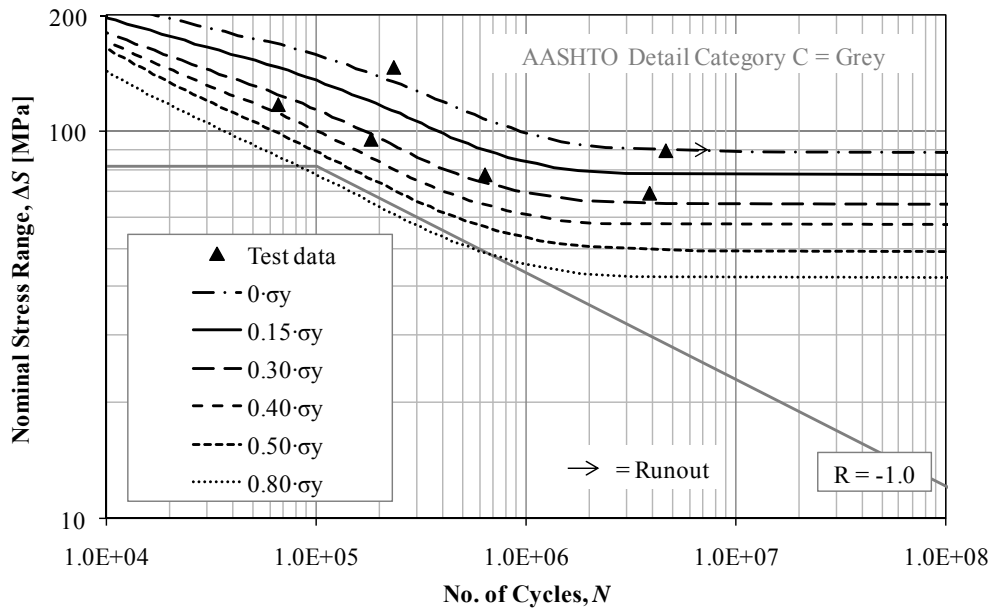


Figure 6.9: Residual stress comparison for  $R = -1.0$

Residual stresses have a significant effect on the fatigue life prediction when considering loading in compression. The expected residual stress at 15% of the base metal yield strength,  $0.15 \cdot \sigma_y$ , provides a fatigue life prediction that is a good fit to the  $R = -1.0$  test data. Based on the LEFM life prediction, a residual stress of  $0.30 \cdot \sigma_y$  provides a lower bound of the test data. Residual stresses of  $0.40 \cdot \sigma_y$  and  $0.50 \cdot \sigma_y$ , similar to conclusions made by Menzemer [1992] for small-scale specimens, show a downward shift in the fatigue life, providing a conservative estimate of the fatigue resistance. The low fatigue life prediction for a residual stress at  $0.80 \cdot \sigma_y$  suggest that for large-scale specimens, which tend to contain higher residual stresses, the fatigue life would be lower than the small-scale specimens tested. Nevertheless, a residual stress of  $0.15 \cdot \sigma_y$ , similar to the residual stress test data previously discussed, is used for the duration of the study unless noted otherwise.

#### Crack Growth Parameters

The upper bound, average (or best fit), and lower bound crack growth rate curves previously discussed in Section 6.3.5 used to examine the effect of the assumed crack growth rate curve on the predicted S-N results. The *best fit* crack growth curve serves as the expected case for this study. Figure 6.10 provides a comparison of the results predicted using the different crack growth curves for an  $R$ -ratio of 0.1.

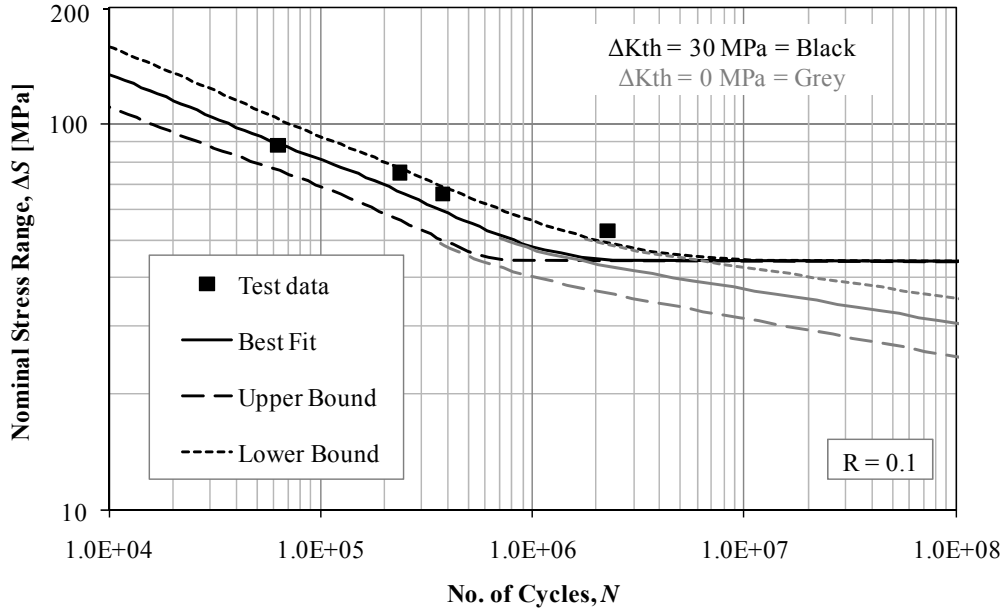


Figure 6.10: Crack growth data comparison for  $R = 0.1$

The *best fit* crack growth curve provides a good prediction of the test data. A crack growth curve somewhere between the *best fit* and lower bound curves seemingly would provide a better fit to the data in this case. The *best fit* crack growth curve was superior, however when considering all  $R$ -ratios tested. Using the best fit crack growth curve, was deemed sufficient in view of the goals of the current study. Further refinement of the model could include additional fatigue testing wherein the crack growth is recorded, and used to generate crack growth curves specific to the tested aluminum grade. All three crack growth curves converge on the same constant amplitude fatigue limit, as shown in Figure 6.10, due to the assumed threshold stress intensity factor,  $\Delta K_{th}$ , of  $30 \text{ MPa}\cdot\sqrt{\text{mm}}$  in this study. Crack growth curves using a  $\Delta K_{th}$  of zero, shown in grey, provide a lower bound solution for all three cases.

## 6.5 Variable Amplitude Analysis

The VA loading analysis presented in this section consists of using the LEFM model discussed in Section 6.2 to make fatigue life prediction, for various VA loading histories, including the histories used for fatigue testing, LH1 and LH2, previously discussed in Section 4.1. As mentioned in the previous section, for the VA loading analysis, all of the expected values remain the same as those used in the CA loading sensitivity analysis, with the exception of the crack shape ratio, which was assumed to be constant at 0.30. Analysis results are presented in this section for the two VA loading

histories considered in the fatigue test program, as well as additional histories including: overload events and histories representative of various influence lines not used previously for fatigue testing. Analyses are performed for the investigated fatigue specimen and for a thicker flange plate with input parameters adjusted to represent full-scale fatigue details.

### 6.5.1 Comparison with VA Test Data

Using the LFM model with the expected inputs, a fatigue life prediction was first generated using the load history LH1. As discussed previously in Section 4.1, the LH1 load history inputted into the test frame was generated from the *ps-m* influence line, representing the positive mid-span moment in a single span bridge with a span of 40 m. A fatigue life prediction for the full 1000 truck history, from the 1995 Ontario study [MTO 1995], representative of the *ps-m* influence line for a 40 m span bridge, was also generated and compared to the LH1 results, as shown in Figure 6.11.

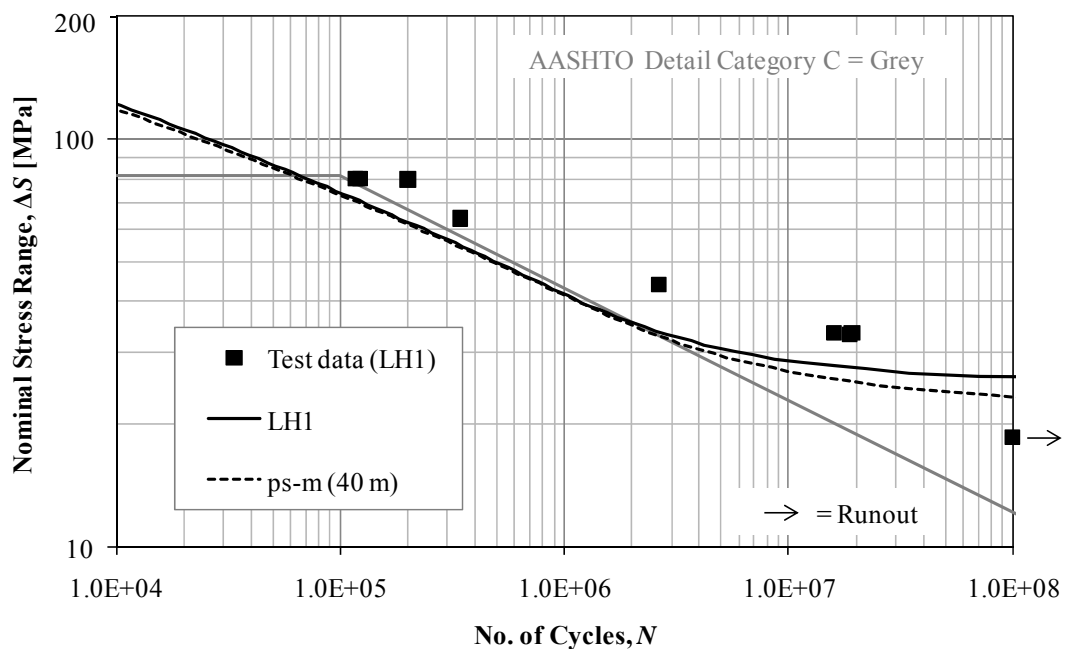
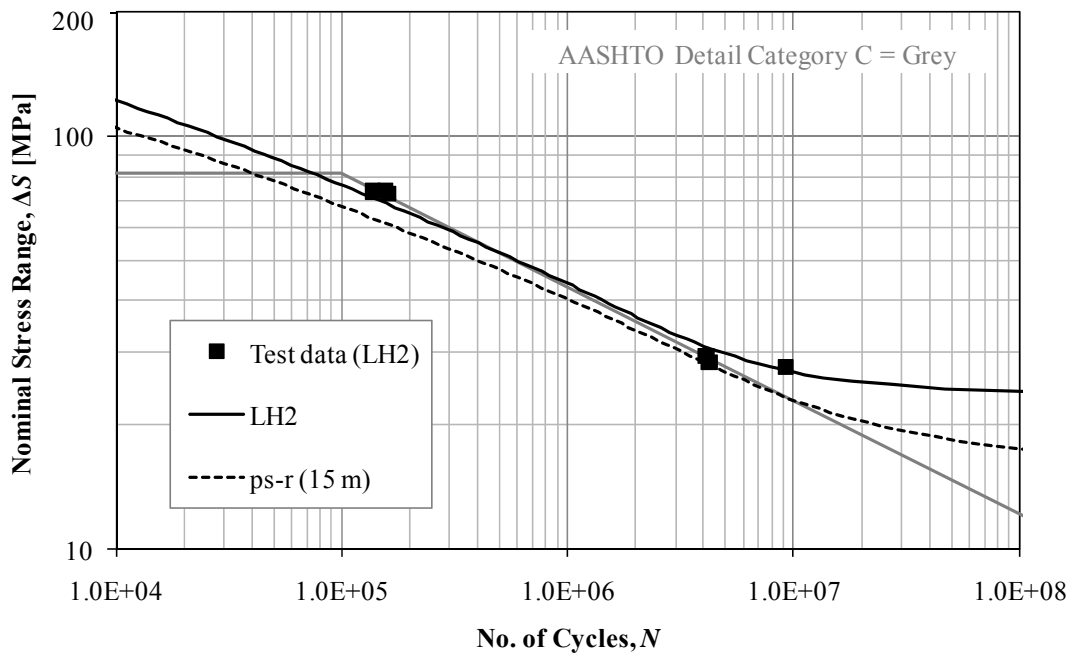


Figure 6.11: VA test data and LFM prediction for load history LH1

The results in both cases provide a conservative estimate of the VA test data for load history LH1. Both fatigue life predictions for the LH1 and *ps-m* (40 m) load histories show little difference, excluding in high life cycle range where there is a downward shift in the curve for the *ps-m* (40 m) history. This difference in the high cycle range between the two fatigue life predictions can be attributed to the fact that the LH1 load history was based on a 200 peak sample from the *ps-m* (40 m)

history. In this case, both the VA test data and the LEFM result, suggest the presence of a secondary slope may model the test data better than the single-slope AASHTO curve also shown in this figure.

A similar comparison was also completed for the LH2 load history, which was generated from the  $ps-r$  influence line, representing shear at the support for a simply supported beam, with a span of 15 m. A fatigue life prediction for the full 1000 truck history, from the 1995 Ontario study [MTO 1995], representative of the  $ps-r$  influence line for a 15 m span bridge, was also generated and compared to the results for load history LH2, as shown in Figure 6.12.



**Figure 6.12: VA test data and LEFM prediction for load history LH2**

Similar trends to those discussed previously for the LH1 load history, are apparent in the life prediction results for the LH2 and  $ps-r$  (15 m) histories. The life prediction for the LH2 load history offers a good fit with the test data. Also in this case, both the VA test data and the LEFM result suggest that a secondary slope may better represent the test data than the single-slope AASHTO curve also shown in this figure.

A comparison of the VA test data, for both the LH1 and LH2 load histories, and the corresponding LEFM predictions is shown in Figure 6.13.

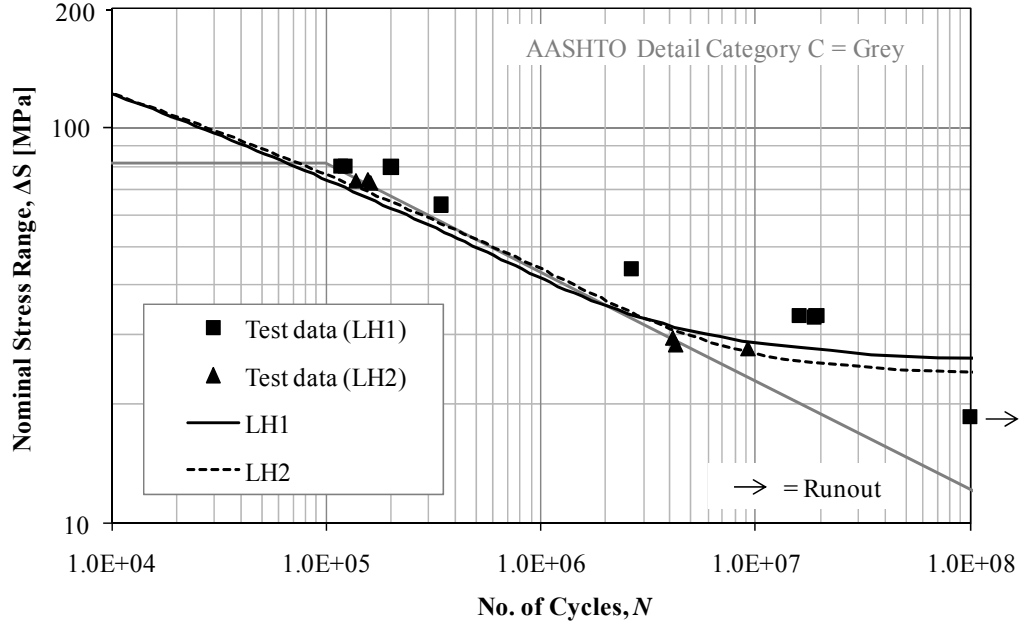


Figure 6.13: VA test data and LEFM prediction for the LH1 and LH2 load histories

As mentioned earlier, life predictions using LEFM provide a good fit of the LH2 test data and a conservative estimate of the LH1 test data. The main difference in the VA test data for both load histories is the lower fatigue life in the high cycle regime, under the LH2 history. This observation is also predicted using the LEFM model, but not to the same degree of difference shown in the test data, where the LH2 load history predicts a lower fatigue life in the high cycle range similar to the LH2 test data. Although the LEFM model used does not fit well with the LH1 test data, it does provide a conservative estimate of the test results. Again, based on the LEFM predictions, a second slope seems warranted and use of the AASHTO single-slope design curve provides a conservative prediction of the fatigue life in this case.

### 6.5.2 Overload Analysis

An overload analysis was conducted, using the overload cases investigated in Section 3.4, for the two influence lines used to generate the load histories for fatigue testing (*ps-m(40 m)* and *ps-r(15 m)*). The first overload case considered was an overload truck consisting of a CL-625 truck with the axle weights doubled occurring at a frequency of 0.1%. For the 1000 truck sample used in the analysis, this meant inserting one overload truck into the load history. The second overload case considered the Nowak [1999] live load model accounting for the simultaneous passage of trucks, discussed

previously. In this case, a modification was made to the Nowak model, which consisted of a worst case scenario, similar to the case presented in Section 3.4.2.2, where the presence of two fully correlated trucks was assumed to occur at every 15<sup>th</sup> occurrence. This assumption was made for this analysis, due to the relatively small truck sample (1000 trucks) used in the LEFM analysis. For a 1000 truck sample the Nowak live load model would only apply two occurrences of fully correlated trucks, which would not necessarily capture the high rare overload events that would be generated if a larger database were used; thus, the modified Nowak model is employed.

Figure 6.14 provides a comparison fatigue life predictions with and without overload events for the LH1 load history.

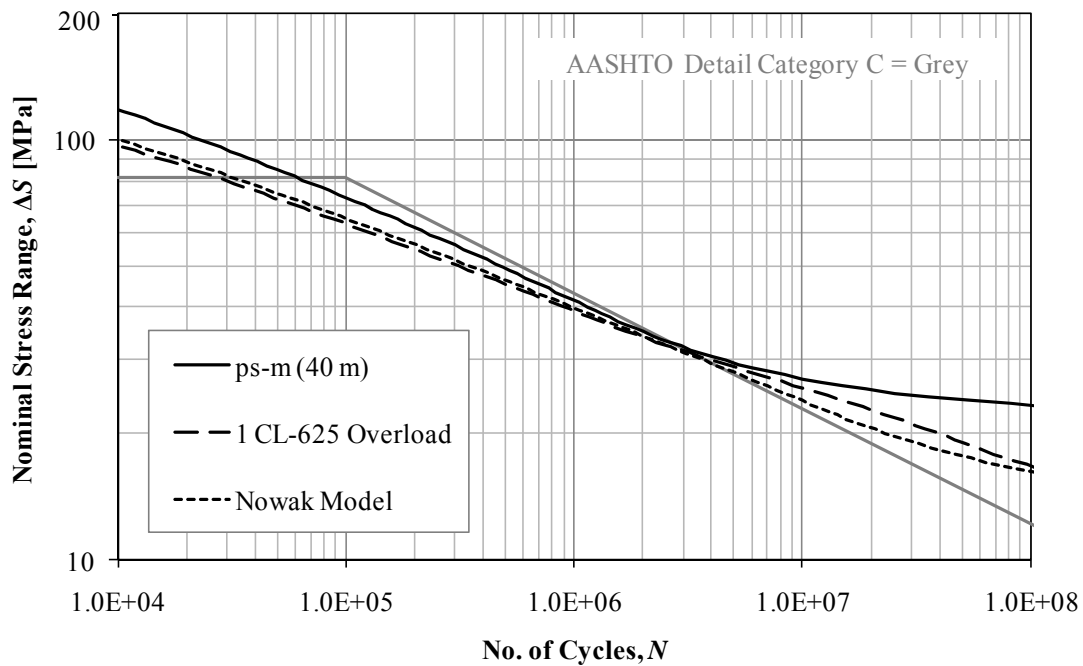


**Figure 6.14: LEFM predictions considering overload events for the LH1 load history**

Based on Figure 6.14, it can be concluded that the effect of overload events is a significant reduction of the fatigue life in the high cycle regime. Use of a two-slope S-N curve is much more apparent when considering the *ps-m (40 m)* influence line with no overloaded events. Although, the modified Nowak live load model does still exhibit a small change in slope at approximately  $1.0 \times 10^7$  cycles, the results may be better represented by a single slope S-N curve.

A similar comparison was also conducted for the LH2 load history, as shown in Figure 6.15.



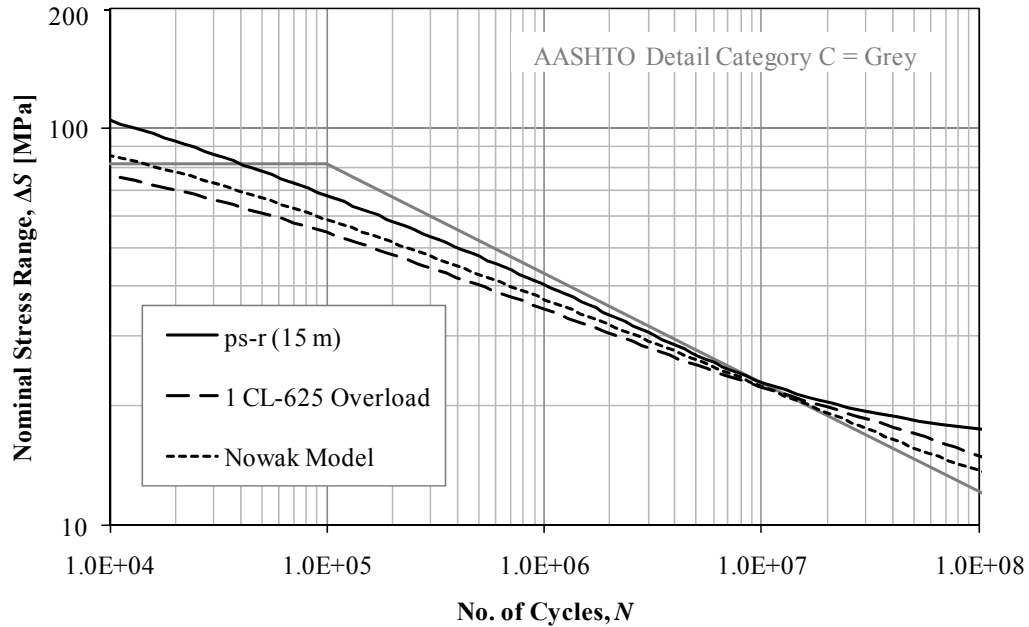
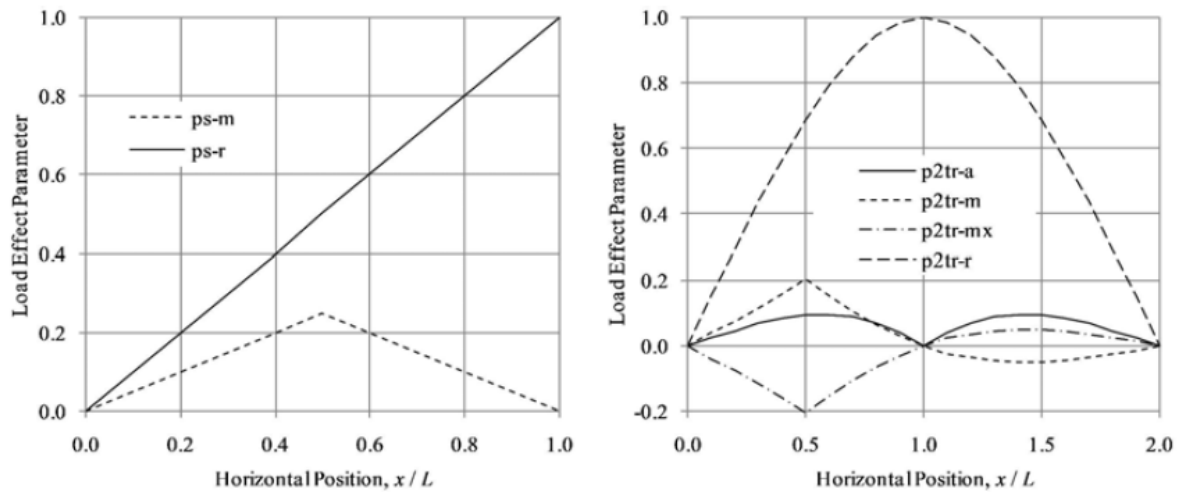


Figure 6.15: LEFM predictions considering overload events for the LH2 load history

Similar trends to the LH1 load history are also apparent when considering overloads using the LH2 load history. A ‘flattening’ of the calculated S-N curve is seen in the high cycle regime, which may suggest that the use of a single-slope S-N curve is appropriate. Another interesting observation, exemplified when considering the *ps-r* influence line, is the fatigue life reduction at high stress ranges, causing a shallower slope to the fatigue life curve. Although the results suggest a single-slope S-N curve is appropriate, the overload cases studies herein represent particularly extreme loading cases, since the live load factor for static design is only 1.7 and the assumption of fully correlated trucks every 15<sup>th</sup> truck passage is conservative.

### 6.5.3 Additional Analysis of Different Influence Lines

In addition to the two influence lines used for fatigue testing and LEFM predictions above, four other influences lines, representative of two-span continuous beams, were used to further extend the scope of the VA loading study. The influence lines used to generate the in-service load effect histories are shown in Figure 6.16.



**Figure 6.16: Influence lines used to generate in-service load effect histories: single-span simply supported girders (left) and two-span continuous girders (right)**

In total, six influence lines were used in this study: moment at the mid-span for one- and two-span girders ( $ps-m$ ,  $p2tr-m$ , and  $p2tr-mx$ ), moment at the intermediate support of two-span girders ( $p2tr-a$ ), and shear at the support ( $ps-r$  and  $p2tr-r$ ). To generate the load effect histories, the same sample of 1000 trucks taken from the 1995 Ontario survey was used.

Figure 6.17 provides an example of the effect bridge span has on the fatigue life for the  $p2tr-mx$  influence line.

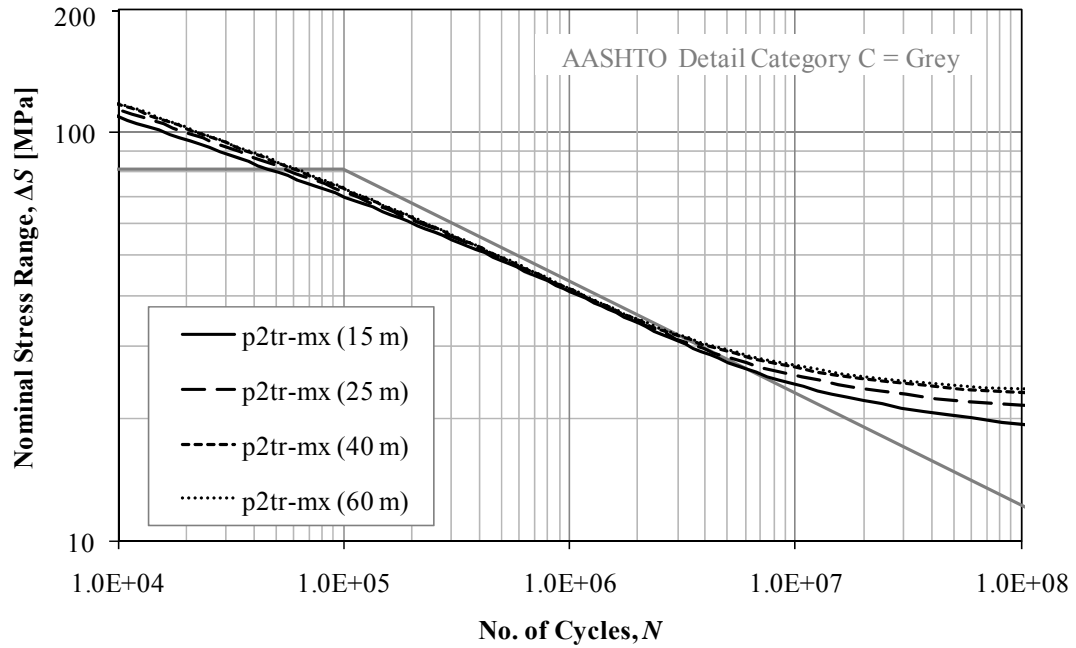
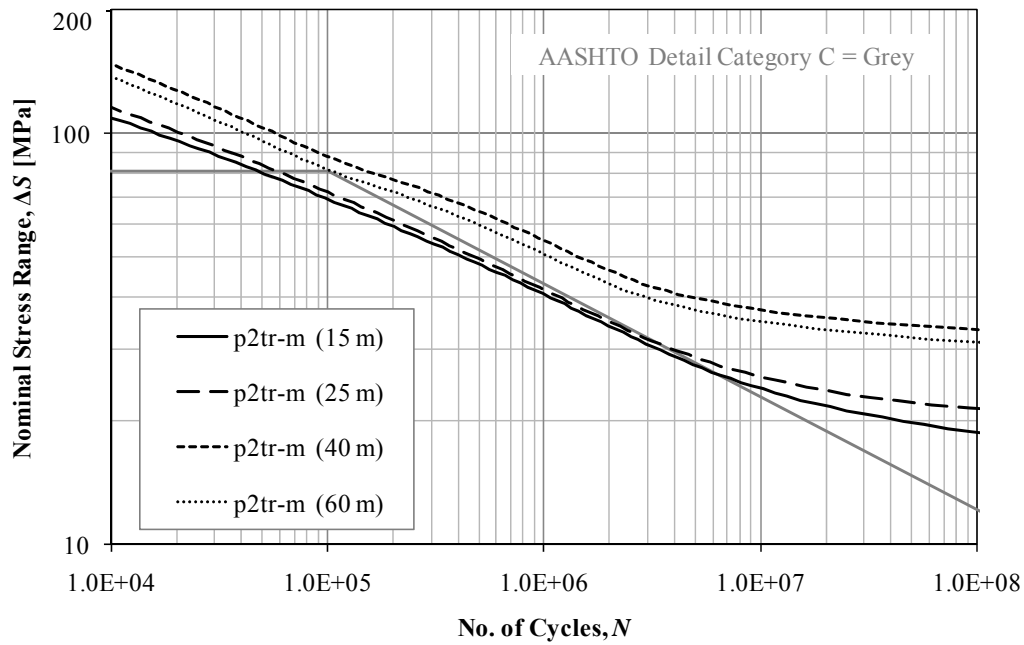


Figure 6.17: Girder span comparison for the  $p2tr-mx$  influence line

The results in Figure 6.17 show little variation in the S-N curve with a change in girder span length. In general, the results show an increase in fatigue life with an increase in span, since more load cycles occur in shorter spans as each individual axle comes on and goes off the bridge. For longer spans, there is a tendency for each truck to cause a single large cycle. Other influence lines analysed,  $p2tr-a$  and  $ps-m$ , show trends similar to that of  $p2tr-mx$ , while the influence lines for shear at the support,  $p2tr-r$  and  $ps-r$ , exhibit no change at all in fatigue life with increase in span. The span had a significant effect on the fatigue life when using the  $p2tr-m$  influence line, as shown in Figure 6.18.



**Figure 6.18: Girder span comparison for the  $p2tr-m$  influence line**

When considering mid-span moments for a two-span girder, the fatigue life increases significantly with an increase in span, up to a span of approximately 40 m.

Figure 6.19 provides a comparison of the 15 m span results for all influence lines employed in this study.

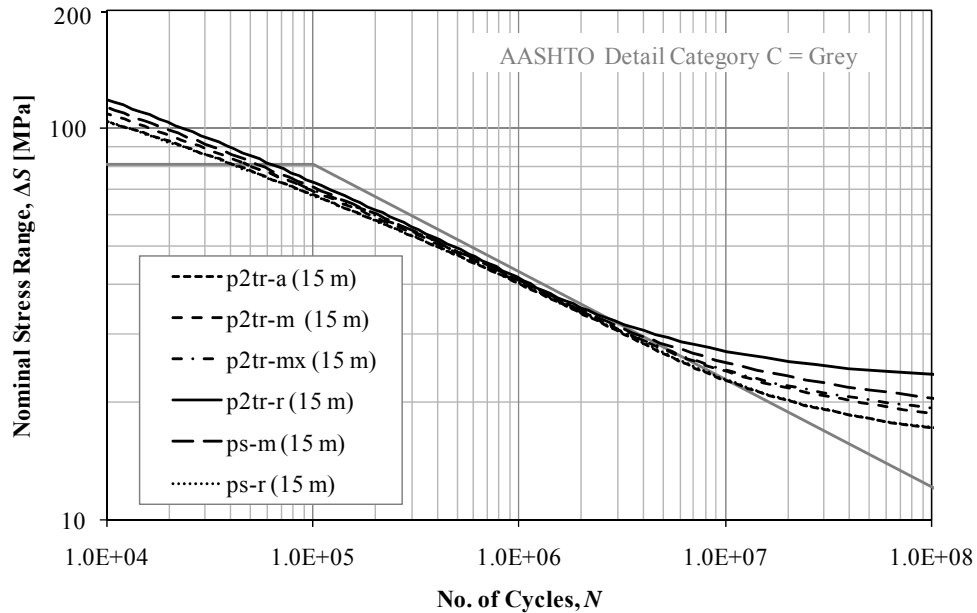


**Figure 6.19: Lower bound LEFM predictions for all influence lines**

Interestingly, the influence line that generated the lowest fatigue life, *ps-r*, was the one considered for generation of the LH2 load history. When considering recommendations on the fatigue design curve, the lower bound defined by the *ps-r* history should therefore govern. The *p2tr-m* influence line with a span of 40 m generated the highest fatigue life prediction in the study.

In general, the fatigue test data for the LH2 load history and fatigue life prediction for *ps-r* fall very closely with the AASHTO design curve for Detail Category C, excluding the high cycle regime. Based on the fatigue life prediction and test data for the LH2 load history one could recommend a second slope to represent the high cycle regime, although the overload analysis suggests that such a recommendation could be unconservative.

#### **6.5.4 Scale Effect Study**

Upon completion of the fracture mechanics analysis described in the previous sections concurrent to fatigue testing in this study, further analysis was conducted to simulate fatigue life predictions for larger scale fatigue details typical of full-scale structures. Herein, the effect of the larger plate thickness, higher residual stresses, and larger initial defect depths, all consistent according to the literature with large-scale specimens, are considered. All other parameters remain the same as defined in the previous studies.

The previous analysis considered a plate thickness of 9.5 mm, representative of the small-scale specimens tested. A plate thickness of 25.0 mm, more typical of full-scale bridge structures, is investigated here. Previously discussed in Section 2.7.4, residual stresses present in large-scale specimens are generally higher; approximately 50 to 80% of the base metal yield strength. Also, with the increased weld sizes required for large-scale components, it is assumed that the probability of more defects is higher, and thus a larger initial defect depth is assumed. Thus, higher initial defect depths, closer to the previously assumed maximum of 0.15 mm, are considered here. The finite element analysis of the weld geometry was also revised, since the plate thickness was increased (while the weld toe radius remains the same), to subsequently calculate the higher SCF present at the weld toe.

Figure 6.20 provides a comparison of both plate thicknesses used in this study, 9.5 and 25 mm, at varying levels of residual stress.

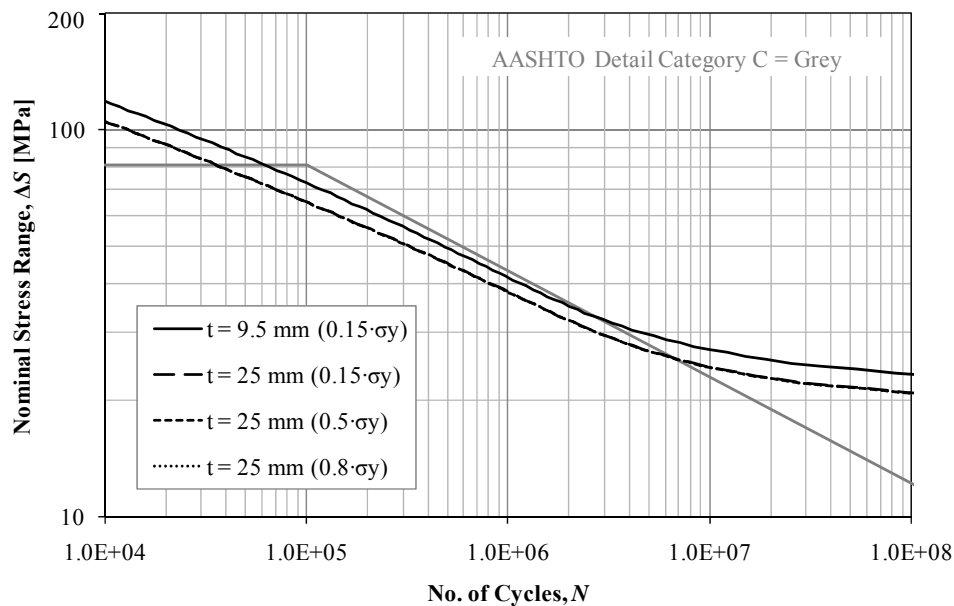
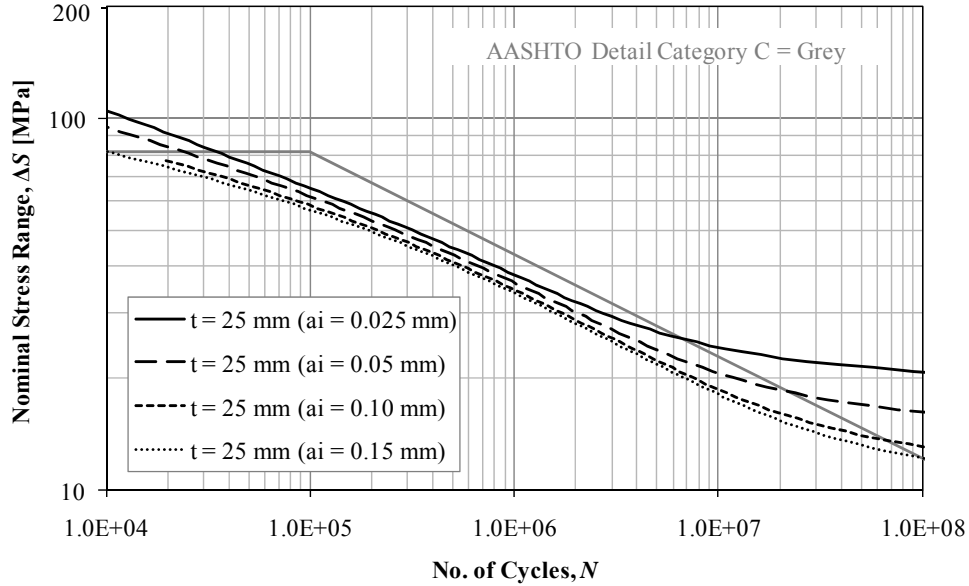


Figure 6.20: Plate thickness comparison for large-scale components

Based on the results presented in this figure, it can be concluded that the fatigue life is reduced when considering an increased plate thickness. Increasing the residual stress level above  $0.15 \cdot \sigma_y$ , on the other hand, has no effect on the fatigue life prediction for the VA loading history used in this study.

Figure 6.21 provides a comparison of varying initial crack depths ranging from 0.025 mm to 0.15 mm for a 25 mm thick plate.



**Figure 6.21: Initial crack depth comparison for large scale components**

Variation of the initial crack depth, similar to the sensitivity analysis presented above, generates a range of fatigue life predictions. In general, increased initial crack depths cause a decrease in fatigue life. When considering a fatigue detail with a plate thickness of 25 mm and initial crack depths greater than 0.025 mm, fatigue life predictions are lower than those given by the AASHTO design curve for Detail Category C. In general, as expected the predicted fatigue life of the large-scale fatigue details is less than those predicted for small-scale specimens.

## 6.6 Strain Based Analysis

In this section, a strain based fracture mechanics (SBFM) model is investigated and predictions made with this model were compared with previous results using the LEFM model.

### 6.6.1 Strain Based Fracture Mechanics Model

A limitation of the LEFM model described in Section 6.2, is that it does not account for the true non-linear material behaviour. Thus, the use of a SBFM model is explored in this section. The SBFM model has the advantage of being able to account for the true non-linear material behaviour.

Similar to the LEFM, the SBFM model assumes the presence of an initial defect, which is assumed to grow according to the Paris-Erdogan crack growth law given in equation (6.1).

According to the SBFM model, the stress intensity factors are calculated using the following expression,

$$K = Y \cdot E \cdot \varepsilon \cdot \sqrt{\pi \cdot (a + a_o)} \quad (6.7)$$

where  $Y$  is a correction factor that accounts for the crack shape, the free surface on one side of the crack, and the plates finite thickness;  $\varepsilon$  is the local strain at a depth,  $a$ , below the surface, and  $a_o$  is an empirical material constant added to the crack depth to account for small crack behaviour,

$$a_o = \left( \frac{\Delta K_{th}}{\Delta \sigma_e} \right)^2 \cdot \frac{1}{\pi} \quad (6.8)$$

where  $\Delta \sigma_e$  is the fatigue limit (assumed herein to equal  $0.5 \cdot \sigma_u$ ). Crack closure effects are again taken into account in the model through calculation of the effective stress intensity factor range. The determination of  $K_{op}$  is the same as the LEFM model, except that the  $K_{max}/K_o$  ratio is replaced by,

$$Y \cdot \frac{\sigma_{max}}{\sigma_o} \quad (6.9)$$

as recommended by McClung [1994], and a limit of 1.0 is introduced. The crack-opening stress model described above, is suited for constant amplitude loading histories. Khalil and Topper [2003] proposed an expression to model the evolution of the crack opening stress following overloads,

$$\sigma_{op} = \sigma_{cu} + \mu \cdot (\sigma_{ss} - \sigma_{cu}) \quad (6.10)$$

where  $\sigma_{cu}$  is the crack opening stress prior to the current cycle,  $\sigma_{ss}$  is the crack opening stress at steady state (or the stress at the current cycle under constant amplitude loading), and  $\mu$  is a material constant. Thus, using this expression the crack opening stress can be modelled under variable amplitude loading histories.

Another distinct difference of the SBFM model is that it accounts for the true, non-linear material behaviour by using a Ramberg-Osgood cyclic material model to calculate the stresses and strains at each load cycle,

$$\Delta \varepsilon = \frac{\Delta \sigma}{E} + 2 \cdot \left( \frac{\Delta \sigma}{2 \cdot K'} \right)^{1/n'} \quad (6.11)$$



where  $K'$  and  $n'$  are material constants representative of cyclic strength and cyclic strain hardening, respectively. Assuming non-linear elastic material behaviour, the stresses and strains are determined for each load cycle. Neuber's rule is then used to determine the strain histories at various depths at the weld toe,

$$\sigma \cdot \varepsilon = \frac{(k_{el} \cdot \sigma_{st})^2}{E} \quad (6.12)$$

where  $\sigma_{st}$  is the structural stress and  $k_{el}$  is the stress concentration factor. Thus, using a Ramberg-Osgood cyclic material model and Neuber's rule, stress-strain histories can be determined for various crack depths.

In summary, based on the procedure presented above, the model consists of cycling the material at various depths below the weld toe to determine the stress and strain parameters for each completed cycle (Figure 6.22). Thus, at any point in the load history, the local elastic stress,  $\sigma_{el}$ , is a function of the local elastic stress,  $\sigma_{el,app}$ , caused by the applied load, and the local elastic residual stresses,  $\sigma_{el,res}$ , due to welding. Residual stresses are considered in the model during the first step of the stress history.

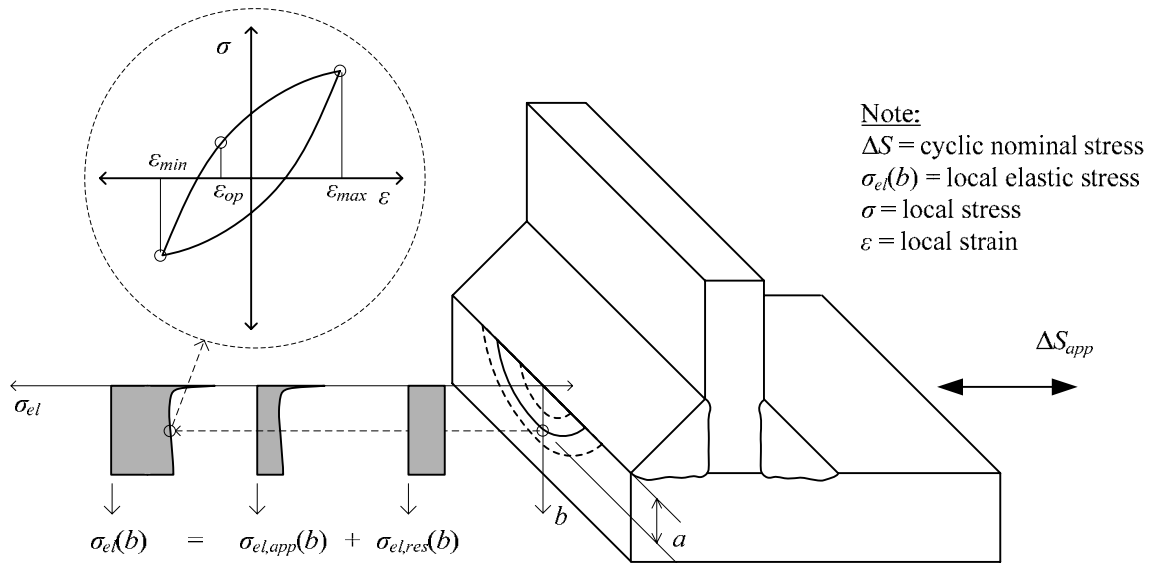


**Figure 6.22: Explanation of stress-strain analysis used in the fracture mechanics model**

Again, a finite element analysis was used to determine the stresses near the notch of the weld toe.

The described model can be improved by replacing the elastic SCF,  $k_{el}$ , with a modified SCF,  $k_p$ , which accounts for the presence of a crack at the weld toe as described in [Dabayeh *et al.* 1998]. The SCF for an uncracked weld toe,  $k_{el}$ , is modified according to,

$$k_p = \frac{K_{el}}{Y \cdot \sqrt{\pi \cdot a}} \quad (6.13)$$

where  $K_{el}$  is the elastic SIF accounting for the non-uniform stress distribution along the crack path. The weight functions,  $m(b, a, c)$ , prescribed by Shen and Glinka [1991] are used to calculate the elastic SIF as shown below,

$$K_{el} = \int_0^a k_{el}(b) \cdot m(b, a, c) \cdot dx \quad (6.14)$$

The local elastic strain is associated to a give nominal stress level,  $S$ , according to,

$$\sigma_{el} = k_p \cdot S \quad (6.15)$$

Thus, for a given structural stress history, the local nonlinear stress-strain history can then be determined. Each time a stress-strain hysteresis loop is closed, the maximum, minimum, and crack closure stresses and strains ( $\sigma_{max}$ ,  $\varepsilon_{max}$ ,  $\sigma_{min}$ ,  $\varepsilon_{min}$ ,  $\sigma_{op}$ ,  $\varepsilon_{op}$ ) are calculated. Using the parameters calculated,  $\Delta K_{eff}$  and  $da/dN$  can then be calculated. Then, a numerical integration of the modified Paris-Erodgan crack growth law is completed to determine the fatigue life.

### 6.6.2 Analysis Results Using SBFM

Using the same input parameters for the LEFM analysis, the SBFM model was employed to generate fatigue life predictions that could be compared with the results of the LEFM analysis. Figure 6.23 compares the results for the SBFM and LEFM models under CA loading.

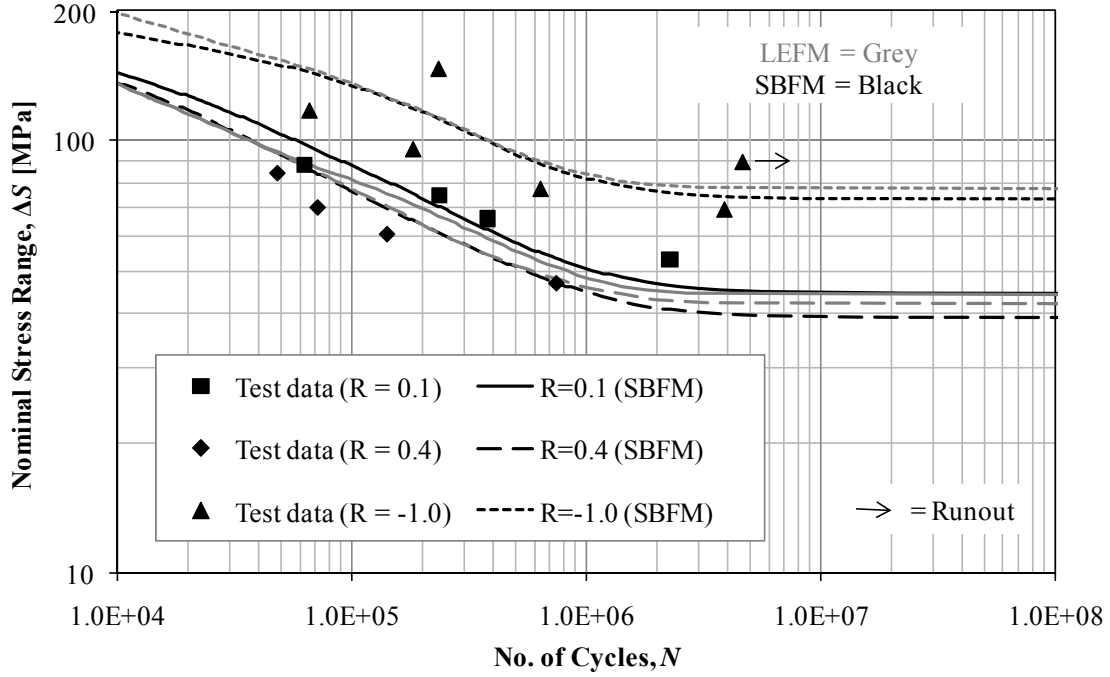


Figure 6.23: LEFM and SBFM comparison for CA loading

In general, the LEFM and SBFM results for each  $R$ -ratio remain fairly consistent. Similarly, the results using the SBFM model also fit well with the CA test data. Differences in the results between the two approaches vary depending on the  $R$ -ratio. For an  $R$ -ratio of -1.0, the SBFM model provides lower fatigue life predictions in the high and low cycle ranges. For an  $R$ -ratio of 0.1, the SBFM model provides a higher fatigue life prediction at high stress ranges, while predicting the same CAFL as the LEFM analysis. In contrast, for an  $R$ -ratio of 0.4, the SBFM model generates a lower prediction of the CAFL than the LEFM model. In comparison with the LEFM model and the CA fatigue test data, use of the SBFM model is adequate.

A similar comparison, between the SBFM and LEFM models, was also conducted under VA loading conditions, as shown in Figure 6.24.

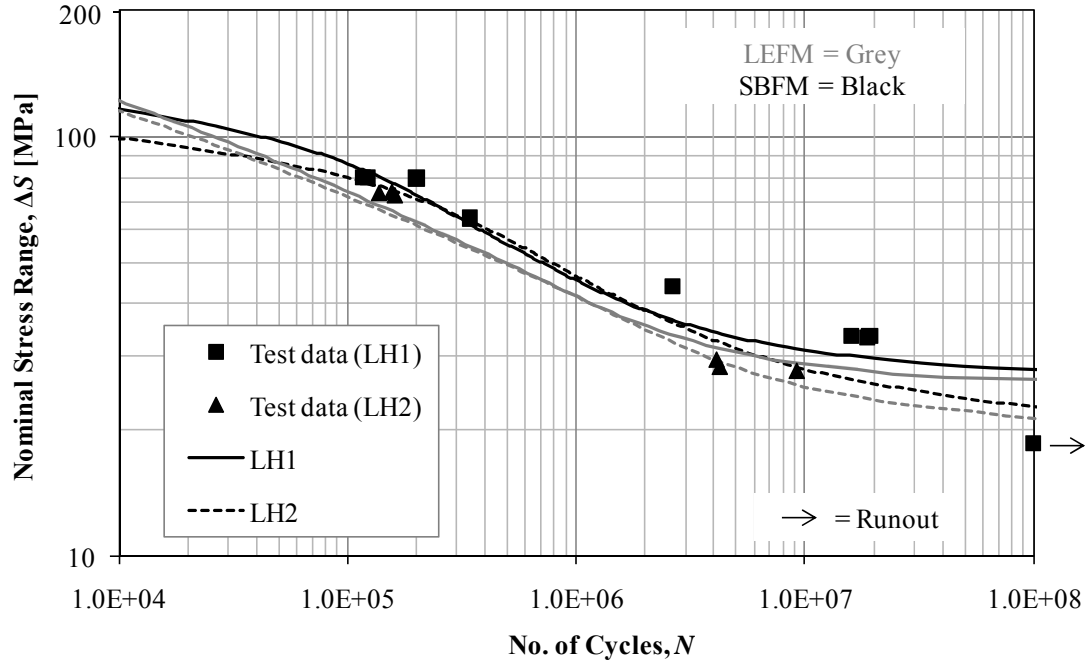


Figure 6.24: LEFM and SBFM comparison for VA loading

A slight variation in the fatigue life prediction for the LEFM and SBFM approaches is apparent, but in general the results remain fairly consistent. The difference in the results under VA loading may be due in part to the different assumptions made regarding the evolutions of the crack opening stress made in implementing the two models. The SBFM model also suggests use of a two-slope design S-N curve would best represent the results, similar to results using LEFM, but provides a less conservative fatigue life prediction. The shape of both curves remains similar, excluding at high stress ranges where the SBFM generates a reduced fatigue life prediction. Both models adequately model the fatigue test results, although, a more in-depth analysis is recommended to further validate use of SBFM. In this study only one influence line was used, thus further analysis could investigate various influence lines, span lengths, and loading conditions including overload events.

## **Chapter 7**

### **Conclusions and Recommendations**

#### **7.1 Conclusions**

Conclusions are divided into the two major areas of study: the fatigue correction factors, and the experimental testing and fracture mechanics analysis.

##### **7.1.1 Fatigue Correction Factors**

Based on the investigation of the fatigue correction factors in CSA-S6 and AASHTO presented in Chapter 3, the following conclusions are drawn:

- For single-slope design S-N curves in CSA-S6 and AASHTO, the fatigue correction factor increases as the slope increases.
- Also, for two-slope design S-N curves in CSA-S157, the fatigue correction factor increases as truck traffic volume (ADTT) increases.
- In CSA-S6, if the AASHTO design S-N curves are assumed for aluminum, the derived fatigue correction factors should be higher than the current factor (0.52) specified for steel in all cases.
- In AASHTO, the fatigue correction factors for aluminum can be significantly greater than the current factor (0.75). Higher correction factors should be employed for Detail Categories A and B to ensure a level of safety consistent with current design provisions for steel. For Detail Categories C to F, the current factor of 0.75 may still be satisfactory.
- Overloaded trucks generally have little effect on the fatigue correction factor.
- Simultaneous passage of trucks has an effect on the fatigue correction factor. For simultaneous truck crossings, an amplification factor ranging from 1.08 to 1.22 depending on the Detail Category and whether maximum or average curves are considered is proposed.

##### **7.1.2 Experimental Testing and Fracture Mechanics Analysis**

The following conclusions are drawn based on the fatigue and materials laboratory testing, and fracture mechanics analysis presented in this thesis:

### 7.1.2.1 Fatigue Testing

- Constant amplitude tests, at  $R$ -ratios of -1.0, 0.1 and 0.4, generated results with trends similar to those reported previously by others. Wide scatter in the test data for an  $R$ -ratio of -1.0 is assumed to be attributed to residual stress effects caused by tension-compression loading.
- Variable amplitude test results for the two load histories tested, LH1 and LH2, exhibit similar results at high equivalent stress ranges, but in the high cycle regime, lower fatigue lives are found using load history LH2 in comparison with load history LH1.
- A mean crack shape ratio of 0.207 for crack depths between 3.0 and 9.0 mm was found using dye penetrant techniques.

### 7.1.2.2 Materials Testing

#### *Static Tensile Coupon Testing*

- For both as-received and annealed 6061 aluminum, material properties were determined including the modulus of elasticity, yield, and ultimate strengths (see Table 6.1).

#### *Cyclic Coupon Testing*

- Cyclic material properties,  $K'$  and  $n'$ , were determined through cyclic testing of both as-received and annealed 6061 aluminum (see Table 6.1).

#### *Hardness Testing*

- Vickers hardness measurements of 110, 75, and 60 for as-received, HAZ, and annealed 6061 aluminum were determined, respectively.

#### *Residual Stress Testing*

- Residual stress testing on one fatigue test specimen found residual stresses present at the weld toe with a maximum magnitude, in tension, of 15% of the base metal yield strength.

### 7.1.2.3 Fracture Mechanics Analysis

Based on CA fatigue test data, a sensitivity analysis was conducted to review the assumed input parameters employed in the LEFM analysis, which concluded that:

- Input parameters assumed for the VA analysis (see Table 6.2), from testing in this study and previous research, including, material properties, initial crack depth, crack shape, and crack

growth data, were considered adequate based on a sensitivity analysis of the LEFM model employed.

- Use of a constant crack shape ( $a/c$ ) of 0.3 provided a good fit with the fatigue test data.

A working LEFM model was then used to compare fatigue life predictions with VA testing data, resulting in the following conclusions:

- The life prediction for the LH1 load history provides a conservative estimate of the fatigue life in the high cycle range and the LH2 load history provides a good fit with the test data. The LEFM model for the LH2 load history does predict a fatigue life less than predicted for the LH1 load history, which is consistent with the test data. The difference between the test results for the two VA loading histories is, however, underestimated by the LEFM model. In both cases, the fatigue life curves exhibit increased fatigue life in the high cycle range, warranting the use of a two-slope S-N curve pending additional large-scale testing.
- Fatigue life predictions considering overloaded trucks and simultaneous truck crossings are reduced in the high cycle range. For simultaneous truck crossings, the fatigue life prediction suggests that the use of a single-slope design S-N curve may be adequate, although the assumed overloads were conservative.
- Fatigue life predictions generated for a wide range of influence lines found that the two influence lines,  $ps-m$  and  $ps-r$ , used to generate the LH1 and LH2 loading histories essentially provide a good representation of all the influence lines reviewed. The  $ps-r$  (15 m) loading history represents a lower bound fatigue life prediction.
- In a scale effect study, whereby input parameters for plate thickness, residual stress, and initial defect depth were increased to represent full-scale fatigue details, a general downward shift in the fatigue life curve is found.
- The explored SBFM model considered non-linear material effects on the fatigue life prediction and provided similar results to the LEFM analysis.

In general, the results show potential for use of a two-slope curve but more large-scale experimental testing in the high-cycle region is required using up-to-date traffic data and live load models.

## **7.2 Recommendations for Future Work**

The following recommendations are presented for the two major areas of study: the fatigue correction factors, and the experimental testing and fracture mechanics analysis.

### **7.2.1 Fatigue Correction Factors**

Based on the findings in this investigation, the following recommendations on future research toward the development of fatigue correction factors are proposed:

- The current study for CSA-S6 uses an Ontario traffic survey from 1995. Estimation of the fatigue correction factor could be refined by use of a more up-to-date traffic database that considers WIM data, which provides a more realistic representation of actual traffic as it would account for overloaded trucks that may avoid weigh stations otherwise. Since the current study only considers truck traffic from Ontario, traffic data included from other provinces may further refine the study.
- The fatigue corrections factor calculations for the AASHTO code could be improved by using more recent WIM data from the United States.
- Further analytical studies employing more advanced simultaneous vehicle crossing models using probabilistic or reliability-based methods would be beneficial.

### **7.2.2 Experimental Testing and Fracture Mechanics Analysis**

- Additional experimental work with an emphasis on VA fatigue testing in the high cycle range is needed. In the current study, limited small-scale VA test data does not provide enough information to confidently recommend a second slope in the high cycle range.
- Additional experimental testing using large-scale specimens would be of benefit. Past research confirms that higher residual stresses in full-scale specimens due to an increase in welding causes a reduction in fatigue strength not captured by small-scale specimens.
- From this study, it was found that it is difficult to find a small sample of a VA load history that is representative of the entire history. Therefore, for future fatigue testing larger VA load histories should be used to better represent realistic loading conditions. Testing using more up-to-date WIM data will better quantify the effects of overload events if larger load histories are utilized.



- More testing to define the input parameters for the fracture mechanics analysis is required. Specifically, further material testing to better define the elastic modulus, yield and ultimate strengths, and most importantly the cyclic material constants,  $K'$  and  $n'$ , in the HAZ is required for use in the fracture mechanics analysis. Also, further testing to determine the crack growth data specifically for the specimen and material tested would further refine the fracture mechanics analysis.
- Further analysis is required using the SBFM model, especially to examine the effects of overloads on the fatigue life predictions.

## References

- Agarwal, Akhilesh C. and Edward C. Lane. "Permissibility of Mobile Cranes by the Proposed Overweight Permit Guidelines." 1980.
- American Association of State Highways and Transportation Officials. AASHTO LRFD Bridge Design Specification. Fourth Edition. 2007.
- American Society for Testing of Materials. ASTM B 918M - 09: Standard Practice for Heat Treatment of Wrought Aluminum Alloys. 2009.
- American Society for Testing of Materials. "ASTM E3-01: Standard Guide for Preparation of Metallographic Specimens." 2007.
- American Society for Testing of Materials. ASTM E8M-04 Standard Test Methods for Tension Testing of Metallic Materials. 2004.
- American Society for Testing of Materials. ASTM E92-82(2003)e2: Standard Test Method for Vickers Hardness of Metallic Materials. 2003.
- Arrien, Paul, Josee Bastien and Denis Beaulieu. "Rehabilitation of Bridges Using Aluminum Decks." Canadian Journal of Civil Engineering 28 (2001): 992-1002.
- Baumel Jr., A. and T. Seeger. Materials Data for Cyclic Loading - Supplement 1. New York: Elsevier Science Publishing Company, 1990.
- British Standards Institution. BS 8118: Structural use of aluminum. 1992.
- Burk, J. D. and F. V. Lawrence Jr. The Effect of Residual Stresses on Weld Fatigue Life. Fracture Control Program Report No. 29. Urbana: University of Illinois, 1978.
- Canadian Society for Civil Engineering. Arvida Bridge QC. 2005. 20 January 2009  
<<http://history.csce.ca/ArvidaBridge.aspx>>.
- Canadian Standards Association. Calibration Report for CAN/CSA-S6-06: Canadian Highway Bridge Design Code. 2007.
- Canadian Standards Association. CAN/CSA-S157-05: Strength Design in Aluminum. Fourth Edition. 2005.

- Canadian Standards Association. CAN/CSA-S6.1-06: Commentary on the Canadian Highway Bridge Design Code. 2006.
- Canadian Standards Association. CAN/CSA-S6-06: Canadian Highway Bridge Design Manual. 2006.
- Dabayeh, A. A., A. J. Berube and T. H. Topper. "An experimental study of the effect of a flaw at a notch root on the fatigue life of a cast Al 319." International Journal of Fatigue 20.7 (1998): 517-530.
- Das, Subodh K. and J. Gilbert Kaufman. "Aluminum Alloys for Bridges and Bridge Decks." The Minerals, Metals, and Materials Society (2007): 61-72.
- Downing, S.D. and D. F. Socie. "Simple Rainflow Counting Algorithms." International Journal of Fatigue (1982): 31-40.
- European Committee for Standardization. prEN 1999-1-3: Eurocode 9 - Design of aluminum structures - Structures susceptible to fatigue. 2006.
- Gitter, Reinhold. "Aluminum Material for Structural Engineering - Essential Properties and Selection of Materials." Structural Engineering International (2006): 294-300.
- Harwood, Douglas W., et al. Review of Truck Characteristics as Factors in Roadway Design. NCHRP Report 505. Washington: Transportation Research Board, National Research Council, 2003.
- Hecker. Smithfield Street Bridge Pittsburgh. 2003. 20 January 2009  
<<http://www.iceandcoal.org/bridges/smithfield/smithfield.html>>.
- Hobbacher, A. "Recommendation for Fatigue Design of Welded Joints and Components." IIW Document XIII-1965-03 / XV-1127-03. 2005.
- Jaccard, Robert, Dimitris Kostea and Roland Ondra. "Background Documents to Fatigue Design Curves for Welded Aluminum Components." IIW Doc. No. XIII-1588-95. 1995.
- Khalil, M. and Tim H. Topper. "Prediction of crack-opening stress levels for 1045 as-received steel under service loading spectra." International Journal of Fatigue 25 (2003): 149-157.
- Kosteas, Dimitris and Serge Bompard. "Correlating Design and Quality Classifications of Welded Structural Details in Fatigue." Sixth International Conference on Aluminum Weldments. Cleveland: INALCO, 1995. 487-502.

Kosteas, Dimitris. "Estimating Residual Stresses and Their Effect in Welded Aluminum Components in Fatigue." American Society for Testing and Materials (1988): 122-130.

Kulicki, John. M., et al. Updating the Calibration Report for AASHTO LRFD Code. NCHRP Report 186. Washington: Transportation Research Board, National Research Council, 2007.

Maddox, S.J. "Review of fatigue assessment procedure for welded aluminum structures." International Journal of Fatigue 25 (2003): 1359-1378.

Mazzolani, Frederico M. "Structural Applications of Aluminum in Civil Engineering." Structural Engineering International (2006): 1-4.

Menzemer, Craig C. and John W. Fisher. "Fatigue Design of Welded Aluminum Structures." Journal of the Transportation Research Record (1993): 79-88.

Menzemer, Craig C. "Fatigue Behaviour and Design of Aluminum Structures." Progress in Structural Engineering and Materials 2 (2000): 120-127.

Menzemer, Craig C. Fatigue Behaviour of Welded Aluminum Structures. PhD Thesis. Bethlehem: Lehigh University, 1992.

Ministry of Forestry. "Forest Service Bridge Design and Construction Manual." 2002.

Ministry of Transportation of Ontario. "Ontario Commercial Vehicle Survey." 1995.

Moses, F., C. G. Shilling and K. S. Raju. Fatigue Evaluation Procedures for Steel Bridges. NCHRP Report 299. Washington: National Cooperative Highway Research Program, 1987.

Moses, Fred. Calibration of Load Factors for LRFR Bridge Evaluation. NCHRP Report 454. Washington: Transportation Research Board, National Research Council, 2001.

Newman, J. C. "A Crack Opening Stress Equation for Fatigue Crack Growth." International Journal of Fatigue 24 (1994): R131-R135.

Nowak, A.S. Calibration of the LRFD Bridge Design Code. NCHRP 368. Washington: Transportation Research Board, National Research Council, 1999.

O'Connor, Colin and Peter A. Shaw. Bridge Loads. New York: Spon Press, 200.

Okura, I. "Application of Aluminum Alloys to Bridges and Joining Technologies." Welding International 17 (2003): 781-785.

- Pineault, J.A., M.E. Brauss and J.S. Eckersley. "Residual Stress Characterization of Welds Using X-ray Diffraction Techniques." Proceedings from AWS Convention, Welding Mechanics and Design. Chicago, 1996.
- Sharp, Maurice L., Glenn E. Nordmark and Craig C. Menzemer. Fatigue Design of Aluminum Components & Structures. Toronto: McGraw-Hill, 1996.
- Shen, G. and G. Glinka. "Weight functions for a surface semi-elliptical crack in a finite thickness plate." Theoretical and Applied Fracture Mechanics 15 (1991): 247-255.
- Sivakumar, Bala, et al. Legal Truck Loads and AASHTO Legal Loads for Posting. NCHRP Report 575. Washington: Transportation Research Board, National Research Council, 2007.
- Siwowski, Tomasz. "Aluminum Bridges - Past, Present, and Future." Structural Engineering International (2006): 286-293.
- Snyder, F. E., G. E. Likins and F. Moses. Loading Spectrum Experience by Bridge Structures in the United States. Report FHWA/RD-85/012. Cleveland: Case Western Reserve University, 1985.
- Soetens, F., IJ. J. Van Straalen and O. D. Dijkstra. "European Research on Fatigue of Aluminum Structures." Sixth International Conference on Aluminum Weldments. Cleveland: INALCO, 1995. 53-64.
- Stephens, Ralph I., et al. Metal Fatigue in Engineering. Second Edition. Toronto: John Wiley & Sons Inc., 2001.
- The Aluminum Association. Aluminum Design Manual. 2005.
- Thompson, Kurt P., et al. "Corrosion and Fatigue Resistance Study of Aluminum Bridge Deck." Journal of the Transportation Research Record (1996): 18-21.
- Walbridge, Scott and Reid Coughlin. "Aluminum Bridge Structures - Recommendations Regarding S-N Design Curves and Fatigue Correction Factor." Second International Conference on Fatigue and Fracture in the Infrastructure. Philadelphia: Lehigh University, 2009.
- Walbridge, Scott. "Fatigue analysis of post-weld fatigue improvement treatments using a strain-based fracture mechanics model." Engineering Fracture Mechanics 75 (2008): 5057-5071.

Wang, C. H., L. R. F Rose and J. C. Newman. "Closure of plane-strain cracks under large-scale yielding conditions." Fatigue & Fracture of Engineering Materials & Structures 25 (2002): 127-139.